แบบจำลองพลศาสตร์ของไหลเชิงคำนวณของผลกระทบของท่อกั้นในไมโครฟิลเตรชั่นเมมเบรน
ที่มีช่องทางการไหลลักษณะรูปดาวสำหรับการบำบัดน้ำ

นายโสภณ ลีชาแสน

วิทยานิพนธ์นี้เป็นส่วนหนึ่งของการศึกษาตามหลักสูตรปริญญาวิศวกรรมศาสตรมหาบัณฑิต
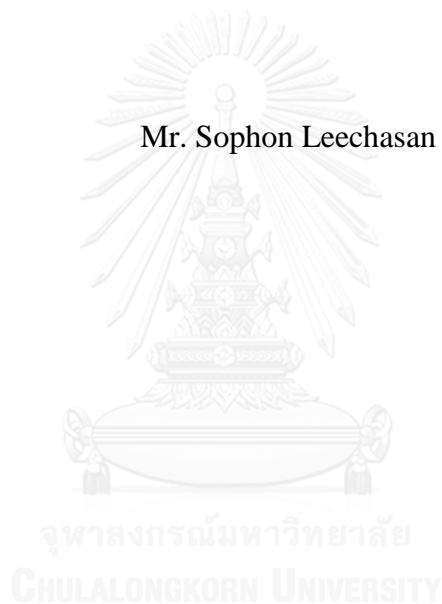สาขาวิชาวิศวกรรมเคมี ภาควิชาวิศวกรรมเคมี
คณะวิศวกรรมศาสตร์ จุฬาลงกรณ์มหาวิทยาลัย
ปีการศึกษา 2558
ลิขสิทธิ์ของจุฬาลงกรณ์มหาวิทยาลัย

COMPUTATIONAL FLUID DYNAMICS MODELING OF EFFECT OF BAFFLES I
N STAR SHAPED MICROFILTRATION MEMBRANES FOR WATER
TREATMENT

Mr. Sophon Leechasan

A Thesis Submitted in Partial Fulfillment of the Requirements
for the Degree of Master of Engineering Program in Chemical Engineering
Department of Chemical Engineering
Faculty of Engineering
Chulalongkorn University
Academic Year 2015
Copyright of Chulalongkorn University

| | |
|---|---|
| Thesis Title | COMPUTATIONAL FLUID DYNAMICS MODELING OF EFFECT OF BAFFLES IN STAR SHAPED MICROFILTRATION MEMBRANES FOR WATER TREATMENT |
| By | Mr. Sophon Leechasan |
| Field of Study | Chemical Engineering |
| Thesis Advisor | Pimporn Ponpesh, Ph.D. |

Accepted by the Faculty of Engineering, Chulalongkorn University in Partial Fulfillment of the Requirements for the Master's Degree

....................................................... Dean of the Faculty of Engineering
(Professor Bundhit Eua-arporn, Ph.D.)


THESIS COMMITTEE
....................................................... Chairman
(Associate Professor Seeroong Prichanont, Ph.D.)
....................................................... Thesis Advisor
(Pimporn Ponpesh, Ph.D.)
....................................................... Examiner
(Associate Professor Prasert Pavasant, Ph.D.)
....................................................... Examiner
(Assistant Professor Benjapon Chalermsinsuwan, Ph.D.)
....................................................... External Examiner
(Associate Professor Vejapong Juttijudata, Ph.D.)

โสภณ ลีชาแสน : แบบจำลองพลศาสตร์ของไหลเชิงคำนวณของผลกระทบของท่อกั้นใน
ไมโครฟิลเตรชั่นเมมเบรนที่มีช่องทางการไหลลักษณะรูปดาวสำหรับการบำบัดน้ำ
(COMPUTATIONAL FLUID DYNAMICS MODELING OF EFFECT OF
BAFFLES IN STAR SHAPED MICROFILTRATION MEMBRANES FOR
WATER TREATMENT) อ.ที่ปรึกษาวิทยานิพนธ์หลัก: ดร. พิมพ์พร พลเพชร, 109
หน้า.

การบำบัดน้ำเสียจากโรงงานผลิตยาโดยใช้การกรองแบบเยื่อเลือกผ่านในระดับไมครอนที่
มีช่องทางการไหลลักษณะรูปดาวที่มีท่อกั้นวางขวางอยู่ภายในได้รับการศึกษาด้วยแบบจำลอง
พลศาสตร์ของไหลเชิงคำนวณสามมิติโดยใช้น้ำเสียที่มีส่วนประกอบความเข้มข้นของเพปโทน 16
กรัมต่อลิตร, เนื้อสกัด 11กรัมต่อลิตร, ยูเรีย 3 กรัมต่อลิตร, แอนไฮดรัสไดโพแทสเซียมไฮโครเจน
ฟอสเฟต 2.8 กรัมต่อลิตร, โซเดียมคลอไรด์ 0.7 กรัมต่อลิตร, แคลเซียมคลอไรด์ไดไฮเดรต 0.4
กรัมต่อลิตร และแมกนีเซียมซัลเฟตเฮปตะไฮเดรต 0.2 กรัมต่อลิตร ในเยื่อเลือกผ่านระดับไมครอน
ที่มีช่องทางการไหลลักษณะรูปดาว เส้นผ่านศูนย์กลาง $4.6 \times 10^{-3}$ เมตร ยาว 0.3 เมตรโดยมีท่อกั้น
ขนาดเส้นผ่านศูนย์กลาง $9 \times 10^{-4}$ เมตร ยาว 0.3 เมตร วางขนานอยู่ภายในเมมเบรนโมดูล ค่าฟลักซ์
วิกฤตต่อค่าความดันรวมของระบบจากบทความงานวิจัยถูกนำมาเปรียบเทียบกับผลจากแบบจำลอง
โดยใช้สมการการเคลื่อนที่แบบปั่นป่วน (RNG k-ε turbulence model) และ สมการดีสครีตเฟส
(Discrete phase model) สำหรับนำมาอธิบายพฤติกรรมการไหลภายในเมมเบรนโมดูล พบว่ามี
ค่าความคลาดเคลื่อนระหว่าง 8-14 เปอร์เซ็นต์ จากนั้นศึกษาตัวแปรที่สามารถปรับได้ง่ายในทาง
ปฏิบัติและส่งผลต่อประสิทธิภาพการแยก ได้แก่ ความเร็วขาเข้าของน้ำเสีย โดยศึกษาความเร็วขา
เข้าในช่วง 2.5-4.0 เมตรต่อวินาที พบว่าความเร็วของน้ำเสียขาเข้าที่ให้ค่าฟลักซ์วิกฤตที่สูงสุดใน
การดำเนินการ คือ 4.0 เมตรต่อวินาที หลังจากนั้นศึกษาผลของขนาดของสารแขวนลอยต่อ
ประสิทธิภาพในการบำบัดน้ำเสีย พบว่าเมื่อเพิ่มขนาดของสารแขวนลอยของเนื้อสกัดพบว่าค่าฟ
ลักซ์วิกฤตที่ได้มีค่าสูงขึ้น จากนั้นศึกษาค่าสัมประสิทธิ์ของการชนซึ่งสัมพันธ์กับการคำนวณ
ความสามารถในการเกาะติดพื้นผิวโดยศึกษาในช่วง0.1-1 พบว่าไม่มีผลต่อค่าฟลักซ์วิกฤต หลังจาก
นั้นศึกษาผลกระทบของลักษณะของท่อกั้น พบว่าเมื่อติดตั้งท่อกั้นรูปแบบพิเศษ (Rod baffle)
พบว่าค่าฟลักซ์วิกฤตสูงขึ้น

| ภาควิชา | วิศวกรรมเคมี | ลายมือชื่อนิสิต | ................................... |
|---|---|---|---|
| สาขาวิชา | วิศวกรรมเคมี | ลายมือชื่อ อ.ที่ปรึกษาหลัก | ................................... |
| ปีการศึกษา | 2558 | | |

# # 5570433421 : MAJOR CHEMICAL ENGINEERING

KEYWORDS: MICROFILTRATION MEMBRANE / COMPUTATIONAL FLUID DYNAMIC

SOPHON LEECHASAN: COMPUTATIONAL FLUID DYNAMICS MODELING OF EFFECT OF BAFFLES IN STAR SHAPED MICROFILTRATION MEMBRANES FOR WATER TREATMENT. ADVISOR: PIMPORN PONPESH, Ph.D., 109 pp.

Star shaped microfilter with inserted rod baffle for waste water treatment was studied by the Computational Fluid Dynamics in three dimensions. The composition of substances in waste water consisted of seven substances including peptone 160 mg/L, meat extraction 110 mg/L, urea 30 mg/L, anhydrous di-potassium hydrogen phosphate ($K_2HPO_4$) 28 mg/L, sodium chloride (NaCl) 7 mg/L, calcium chloride dehydrate ($CaCl_2.2H_2O$) 4 mg/L, and magnesium sulphate heptahydrate ($Mg_2SO_4.7H_20$) 2 mg/L. The geometry of the star-shaped microfilter in this study was built based on the system applied by Chiu et al. (2006). It consisted of seven star-shaped channels, that were $4.6 \times 10^{-3}$ m in diameter and 0.3m long, and rod baffles with $9 \times 10^{-4}$ m in diameter and 0.3 m long. The critical flux and trans-membrane pressure from the published experimental-study were compared with the simulation results by using the RNG k-ε turbulence model and discrete phase model to describe flow behavior inside the star shaped microfilter. Which yielded 8-14% deviation from the experimental data. After that, the parametric study was conducted by varying the parameters which could be easily changed in practice and could affect column performance. First, the inlet velocity of waste water was varied from 2.5-4.0 m/s. The result showed that the optimal inlet velocity, which gave the highest critical flux, was 4.0 m/s. Then, the effect of particles size of meat extraction was varied from $3.75 \times 10^{-7}$m to $5 \times 10^{-6}$m. The result showed that the large particle range size gave the highest critical flux. Then, coefficient of restitution was varied from 0.1-1. The result showed that the coefficient of restitution did not affect the critical flux. Moreover, it was found that by inserting the special rod baffle the critical flux was improved.

Department:     Chemical Engineering     Student's Signature _____

Field of Study:     Chemical Engineering     Advisor's Signature _____

Academic Year: 2015

# ACKNOWLEDGEMENTS

## CONTENTS

# LIST OF TABLES

# LIST OF FIGURES

# NOMENCLATURE

| | | |
|---|---|---|
| a | = | Particle radius (m) |
| $C_D$ | = | Drag coefficient |
| $C_{ij}$ | = | Inertial resistance factor |
| $C_x$ | = | Correction factor of shear flow |
| $C_{1\varepsilon}$ | = | Constant |
| $C_{2\varepsilon}$ | = | Constant |
| $C_{3\varepsilon}$ | = | Constant |
| $C_2$ | = | Inertial resistance (1/m) |
| $D_{ij}$ | = | Viscous resistance factor |
| $d_{ij}$ | = | The deformation tensor |
| $d_{lk}$ | = | The deformation tensor |
| $d_{kl}$ | = | The deformation tensor |
| $d_p$ | = | Particle size (m) |
| $E_P$ | = | The energy consumption (Watt) |
| e | = | Coefficient of restitution |
| $F_D$ | = | Drag force of cross-flow (m/s$^2$) |
| $F_L$ | = | Lift force |
| $F_y$ | = | Drag force of filtrate flow (m/s$^2$) |
| $F_i$ | = | Other force |
| $F_{dx}$ | = | Drag force in the x-direction |
| $F_{dy}$ | = | Drag in the y-direction |
| $G_b$ | = | Generation of turbulent kinetic energy due to buoyancy |
| $G_k$ | = | Generation of turbulent kinetic energy due to the mean velocity gradient |
| $g_i$ | = | Gravitational force (m/s$^2$) |
| H | = | Channel width (m) |
| H | = | Channel height (m) |
| I | = | The MOI of cricket bat |
| J | = | Flux (m$^3$/m$^2$.s) |
| $J_c$ | = | Critical flux (m$^3$/m$^2$.s) |

| | | |
|---|---|---|
| $k$ | = | Turbulent kinetic energy |
| $K$ | = | Constant coefficient saffman's lift force equal to 2.594 |
| $M$ | = | Mass of the cricket bat (m/s$^2$) |
| $M_d$ | = | The deposited mass (kg/m$^2$) |
| $m_b$ | = | Mass of the ball (kg) |
| $P_L$ | = | Trans-membrane pressure (Pa) |
| $Q$ | = | Inlet volumetric flow rate (m$^3$/s) |
| $q$ | = | Filtration rate |
| $Re$ | = | Reynolds number |
| $R_f$ | = | Fouling resistance (1/m) |
| $R_m$ | = | Membrane resistance (1/m$^2$) |
| $R_\varepsilon$ | = | Additional term of $\varepsilon$ equation |
| $R'_t$ | = | Total filtration resistance per unit thickness of cake |
| $S$ | = | Membrane area (m$^2$) |
| $S_i$ | = | Source term for the momentum equation |
| $S_\varepsilon$ | = | User defined source term |
| $S_k$ | = | User defined source term |
| $u$ | = | Fluid velocity (m/s) |
| $u_p$ | = | Particle velocity (m/s) |
| $u_s$ | = | Average cross flow velocity (m/s) |
| $u_y$ | = | Fluid velocity in y direction |
| $v$ | = | Velocity of fluid (m/s) |
| $V_b$ | = | Inbound velocity (m/s) |
| $V'_b$ | = | Rebound velocity (m/s) |
| $v_f$ | = | Filtration rate, flux (m$^3$/m$^2$.s) |
| $v_j$ | = | Velocity components in x, y, and z direction (m/s) |
| $v_j$ | = | Liquid velocity in j direction (m/s) |
| $W$ | = | Cross-flow velocity (m/s) |
| $W$ | = | Channel width (m) |
| $x$ | = | Particle size (m) |
| $y$ | = | Channel height (m) |
| $Y_m$ | = | Contribution of the fluctuating dilation in compressible turbulence to the overall dissipation rate |

## GREEK LETTER

| | | |
|---|---|---|
| $\alpha$ | = | Permeability of membrane (1/m) |
| $\alpha$ | = | Specific resistance (m/kg) |
| $\eta$ | = | Dynamic fluid viscosity |
| $n_{\varphi}$ | = | Viscosity as function of particle volume |
| $\rho$ | = | Fluid density ($kg/m^3$) |
| $\rho_p$ | = | Particle density ($kg/m^3$) |
| $\mu$ | = | Viscosity of fluid (Pa.s) |
| $|v|$ | = | Velocity magnitude (m/s) |
| $\Delta n$ | = | Thickness of medium (m) |
| $\tau_w$ | = | Shear stress acting on the membrane surface |
| $v$ | = | Kinematic viscosity of liquid |
| $\sigma_k$ | = | Turbulent Prandtl number of k |
| $\sigma_\varepsilon$ | = | Turbulent Prandtl number of $\varepsilon$ |
| $\varepsilon$ | = | Dissipation rate of turbulent kinetic energy |
| $\alpha_k$ | = | Inverse effective Prandtl number for k |
| $\alpha_\varepsilon$ | = | Inverse effective Prandtl number for $\varepsilon$ |
| $\mu_{eff}$ | = | Effective viscosity coefficient |
| $\gamma_0$ | = | Sheer rate at the membrane surface |
| $\emptyset$ | = | Shape factor |

## ACRONYM

| | | |
|---|---|---|
| CFD | = | Computational fluid dynamics |
| TMP | = | Trans-membrane pressure |

# CHAPTER1

# INTRODUCTION

## 1.1 Motivation

Microfiltration is a pressure-driven membrane separation, the pressure gradient offers driving force to force fluid flows across the membrane and the substances, which are restricted by the membrane's pore size, are retained on the membrane. Thereby, it has been widely used in pharmaceutical, water purification, beer and wine filtration and other food processing industries. The application of microfiltration in pharmaceutical wastewater treatment will be attended in this study. The waste water based on OECD 302A (Inherent Biodegradability) and 303A (Biodegradation of Chemicals) was contaminated by the sludge such as peptone, $CaCl_2.2H_2O$, meat extraction, Urea, $Mg_2SO_4$, $K_2HPO_4$, and NaCl [1, 2]. Operating at long time, the substances can be accumulated on the membrane surface and, cause fouling resistance which obstructs the fluid to permeate to membrane. This will decline the flux and increase energy consumption for the operation.

The impact of hydrodynamics induced by turbulent flows has been widely applied to reduce membrane fouling [3]. There are several techniques to enhance turbulence, for example, inserting turbulence promoter, gas sparging, and applying special membrane geometries [3]. Generally, the industries require membrane filtration with less maintenance, easily-cleaned fouling, and low energy consumption [4]. Microfiltration with special geometries such as star-shaped microfilters can offer maximum surface area with minimized cross-sectional area and, thus, enhanced flow rate. Therefore, they not only induce turbulence which prevents the accumulation of fouling, but also require less pump input power. Studies have shown that star-shaped microfilters provide higher filtration performance, i.e., double the flux while reducing energy input by 50% [4]. However, Chiu et al (2005) [5] claimed that stagnant zones, where turbulent flows were unable to prevent accumulation of the substances near the membrane surface, presented near the tips of the star channels and high flow velocity would reduce these zones. Their claim was based on the occurring of the critical flux. They found that the critical flux was increased when operating at high cross flow velocity, which in turn required high pump input power. Consequently, Chiu et al. (2006) [3] applied baffles in star-shaped microfiltration membrane and found that the system with inserted baffles yielded higher flux while consuming lower energy compared to the system without the baffles.

There are several empirical studies about the effects of turbulent flows induced by special membrane geometry on membrane fouling [6-8]. However, there is still a lack in literature for detailed quantitative and qualitative knowledge about

this effect. Numerical simulation has been applied to provide insight into microfiltration. It not only correctly predicts the results, but also requires a short turnaround time for solving problems in transport phenomena. Liu et al. (2009) [9] used computational fluid dynamics modeling to compare the effects of position of baffles on velocity profile in flow channel. They found that the application of baffle position resulted in high velocity and shear stress near membrane surface which was the factor to improve flux by decreasing particle deposition on membrane surface. Meanwhile, the position of the baffles had a significant effect on pressure drop which effected to the energy cost. CFD modeling has been applied in this study to investigate the velocity and pressure profiles, which affect particle distribution and fouling in a star-shaped microfiltration membrane. The results will help elucidate the transport phenomena occurred in the system and guide the design of the star-shaped microfiltration membrane for an optimum performance.

**1.2 Objectives of the research**

      1.2.1 To study influence of velocity profile on the distribution of particles occurred in system.

      1.2.2 To conduct a parametric study of the star-shaped membrane microfiltration by varying inlet velocity, particle size, and coefficient of restitution using the CFD model, and propose the operation guideline.

      1.2.3 To guide the design of baffle in the star-shaped microfiltration for an optimum performance

      1.2.4 To guide the energy consumption value

**1.3 Scope of the research**

1.3.1 Develop an appropriate CFD model to study the behaviors of fluid and particles in the star shaped microfiltration by using a commercial CFD code, Fluent (Fluent 14.5, ANSYS Inc. Lebanon, NH).

1.3.2 Validate the CFD model by comparing the simulated result of the critical flux with the experimental data of tubular microfiltration membrane from the literatures [10][10].

1.3.3 Validate the CFD model by comparing the simulated result of the critical flux with the experimental data of star-shaped microfiltration from the literatures [3][3].

1.3.4 Employ the validated CFD model to predict the critical flux of star-shaped membrane under different operating conditions (i.e., parametric analysis) such as velocity inlet, particle size, and coefficient of restitution.

1.3.5 Apply the validated model to predict the critical flux at different types of baffles (i.e., geometry).

**1.4 Benefits of the research**

1.4.1 To elucidate the transport phenomena in a star shaped microfiltration membrane by using the CFD model.

1.4.2 To obtain operational and design guideline for the optimum performance (i.e., separation and energy consumption efficiencies) of the star shaped microfiltration membrane.

# CHAPTER2

# THEORY AND LITERATURE REVIEWS

## 2.1 Synthetic waste water

The pharmaceutical's waste water in the activated sludge process from IBACON [11] was the synthetic waste water by using porous pot method as shown in figure 2.1, which was controlled by the organisation for economic coordination and development standard (OECD) i.e., 302A, and 303A. The information of OECD 302A was the inherent biodegradability of substance in waste water which was degraded by the microorganism to verify that the waste water after treatment became to be treated water which was contaminated by the sediment of substance (sludge) [2]. The information of OECD 303A was the production of synthetic waste water in the continuous bio-reactor for 250 day by using porous method that waste water was operated and kept the condition for more realistic with real waste water plant. The composition of substance had seven substance; for example, peptone 160 mg, meat extract 110 mg, urea 30 mg, anhydrous di-potassium hydrogen phosphate ($K_2HPO_4$) 28 mg, sodium chloride (NaCl) 7 mg, calcium chloride dehydrate ($CaCl_2.2H_2O$) 4 mg, and magnesium sulphate heptahydrate ($Mg_2SO_4.7H_2O$) 2 mg [1]. The pH in the process was kept at $7.5 \pm 0.5$ by adding appropriate amounts of hydrochloric acid (HCl) or sodium hydroxide (NaOH) for adjusting PH. The temperature in the process was kept at 20–25 $\circ$C by using a water bath thermostat. The DOC, as show in figure 2.2 indicated the quantity oxygen consumption of aerobic bacteria which used to decompose the inorganic substance. It was found that if low oxygen requirement, the water is waste water. In contrast, at high oxygen requirement the water is the clean water. After 250 day of the synthetic waste water was measure that value of DOC higher than 80 percent which resembled to DOC of real waste water in activated sludge water treatment.
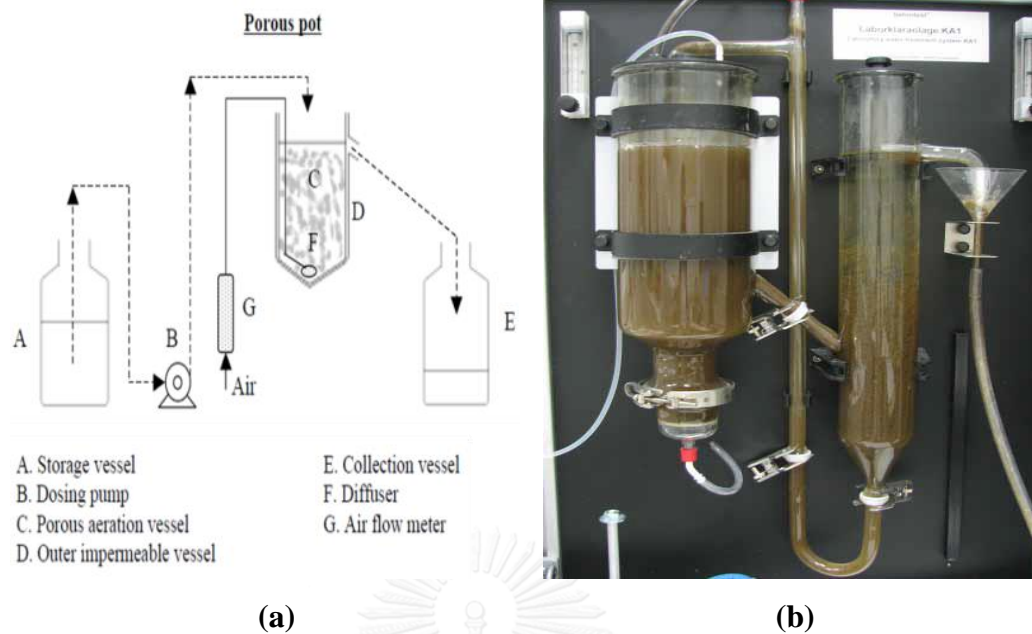
Figure 2.1 Porous pot method a) Process of porous pot method b) porous pot method of IBACON [11]
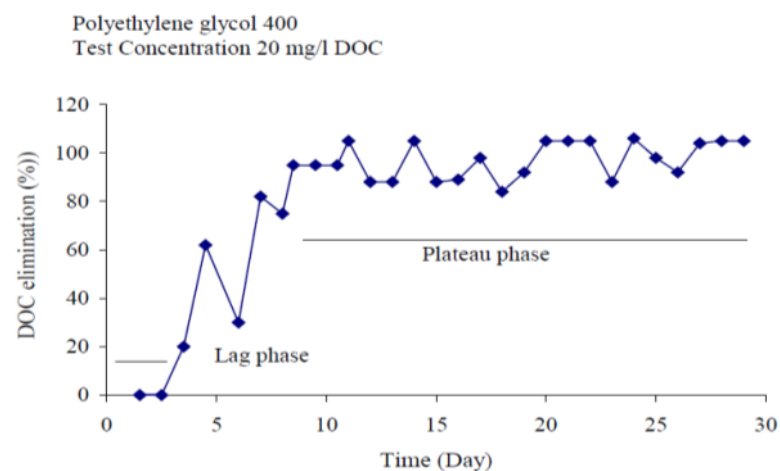


Figure 2.2 DOC elimination of synthetic waste water.[1]

## 2.2 Membrane filtration

Microfiltration is a pressure-driven membrane separation in which the fluid flows across the membrane and the substances, restricted by the membrane's pore size, are retained on the membrane. Microfiltration filtration membrane was classified by membrane pore size that show in table 2.1 and the type of operation in microfiltration membrane was divided by two case (figure 2.3), dead–end

microfiltration and cross-flow microfiltration [12]. The principal of dead-end microfiltration, the flow of fluid is vertically directed to the membrane surface. This operation is effective as long as the quantity of particles to be removed is low. This application has been widely used in sterile filtration of water, beer, and wine industry. In contrast, there are many industrial processes that have a high quantity of particle effected on the membrane surface when operates in a dead-end microfiltration membrane at long time. Cross-flow microfiltration membrane, the flow of fluid is parallelly directed with the membrane surface and fluid can wash the fouling on membrane surface that effect to decrease the accumulation of fouling on membrane surface.

**Table 2.1** Characteristics of membrane processes (Cheryan M. 1998) [13].

| Process | Pore size | Retentate | Permeate |
|---------|-----------|-----------|----------|
| Conventional filtration | >10 μm | Large particles | Small particles, water |
| Microfiltration | 0.1-10 μm | Suspended particles | Dissolvedsolutes,water |
| Ultrafiltration | 0.005-0.1 μm | | Small molecules, water |
| Nanofiltration | 0.0005-0.005μm | Large molecules | Monovalent ions,water |
| Reverse osmosis | <0.5 nm | Small molecules | water |
| | | All solutes | |
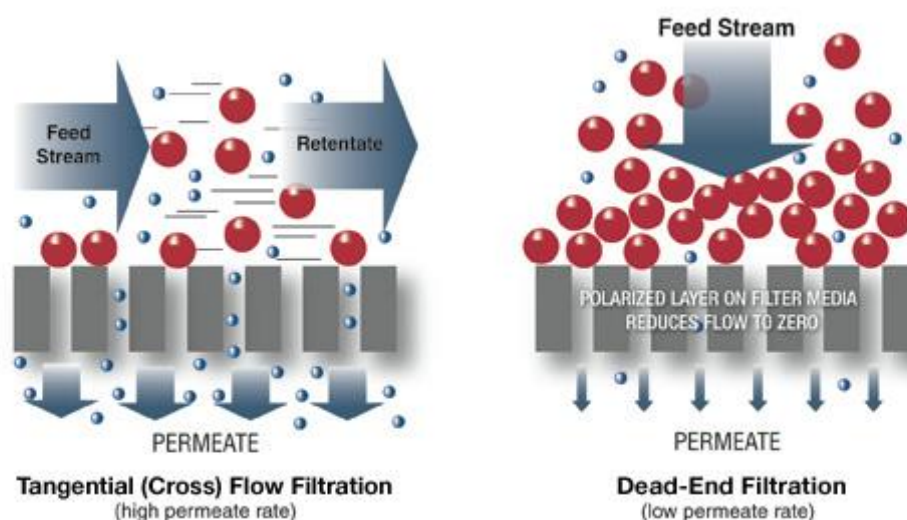


**Figure 2.3** Schematic diagrams of the cross-flow mode (left) and the dead-end mode (right)

http://www.spectrumlabs.com/filtration/Edge.html. SPECTRUM® LABORATORIES,(1995-2008) [14].

## 2.3 Star-shaped microfiltration membrane

Mantec technical ceramics Ltd has been produce the star-shaped microfiltration membrane for high performance cross flow membrane filtration. The characteristic of star-shaped microfiltration membrane (figure 2.4) has maximum surface area with minimize cross-sectional area cause induce turbulence at lower cross flow velocity. At the present time, there are many companies installing the star-shaped microfiltration membrane in their process; for example GlaxoSmithKline Ltd, the pharmaceutical manufactory has been produce the anti-biotic which put the cells in to a liquid and then the cells will produce an anti-biotic drug (figure 2.5). After this process, they used a star shaped microfiltration membrane to purify the anti-biotic drug which is contaminated by cell. The result showed that star-shaped microfiltration membrane is easily clean because the special of geometry membrane can induce turbulence which prevents the accumulation of fouling. Moreover, star-shaped microfiltration membrane used a less energy of pump that saving the operation cost [4].



**Figure 2.4** Geometry of star shaped microfiltration membrane [4]



**Figure 2.5** Installing the star-shaped microfiltration in GSK plant. [4]

## 2.4 Membrane fouling

The substances can be collected on the membrane surface and, over a period of time, cause fouling which obstructs the flux. This will decline the separation efficiency. The models of fouling are divided by 4 models; complete blocking, standard blocking, intermediate blocking, and cake formation (figure 2.6). Complete blocking means the substance size is larger than membrane pore size causing the entrance of membrane pores is blocked up by the substances that obstacle of fluid flows across the membrane. Standard blocking means the substance size is smaller than membrane pore size that substances are accumulated inside the membrane pores. Intermediate blocking is similar to complete blocking but the other substances can collect on the top of the other substances. The cake formation means the substances accumulate on the top of the membrane surface. In addition, the factor of membrane fouling is depended on the physico-chemical nature, i.e., PH, and membrane type (figure 2.7). T.Y. Chiu et al (2008) [15] separated titanium dioxide in star-shaped microfiltration membrane by varying PH and the result showed that operating at PH below 5, flux was decreased because PH relative with interaction between substances and membrane described in term zeta-potential (figure 2.8). Membrane type, Cheryan et al. [16] studied separation the oily waste water by using hydrophobic membrane that free oil could coat membrane caused decreasing of flux. Moreover, operating conditions is the significant factor of membrane fouling, i.e., temperature, volumetric flow rate, and pressure. Temperature, In contrast, Brandsma and Rizvi [17] separated milk by membrane filtration at high temperature and the result showed that protein was degraded when operating at high temperature caused low solubility and high accumulation of fouling in membrane surface. Volumetric flow rate, Jirarathanon and Chanachai [18] separated passion fruit juice in ultrafiltration by varying volumetric flow rate and the result showed that turbulent flow had a higher shear for decreasing of fouling at membrane surface caused higher permeation flux. Pressure, separated by varying trans-membrane pressure and the result showed that flux was increase when operated at high pressure however increase however, when increased trans-membrane too much, substances were compacted by pressure caused dense fouling on membrane surface that flux was decreased.



(A) Complete pore blocking        (B) Standard blocking

(C) Intermediate blocking        (D) Cake formation
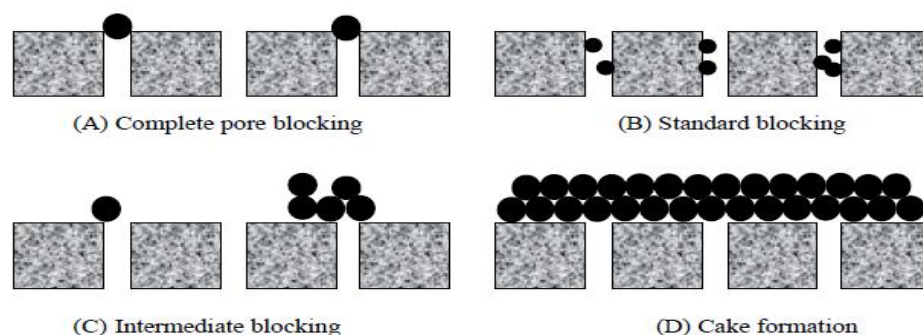
**Figure 2.6** Mechanism type of fouling [19].
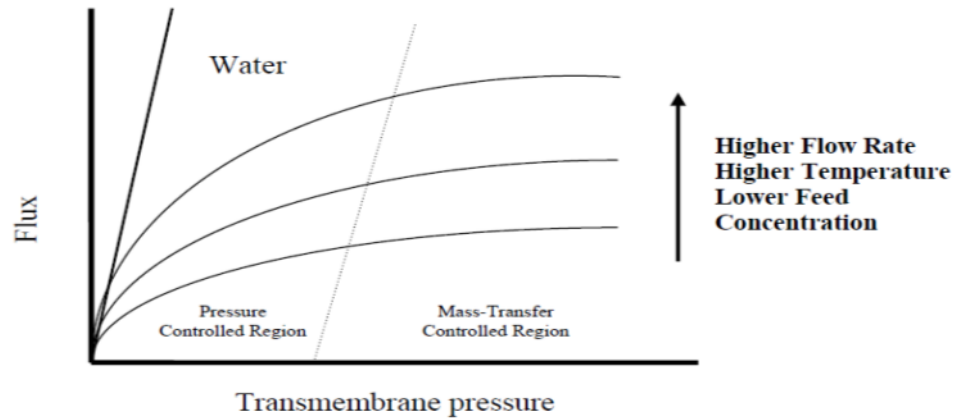
**Figure 2.7** The effect of operating condition to flux [18].
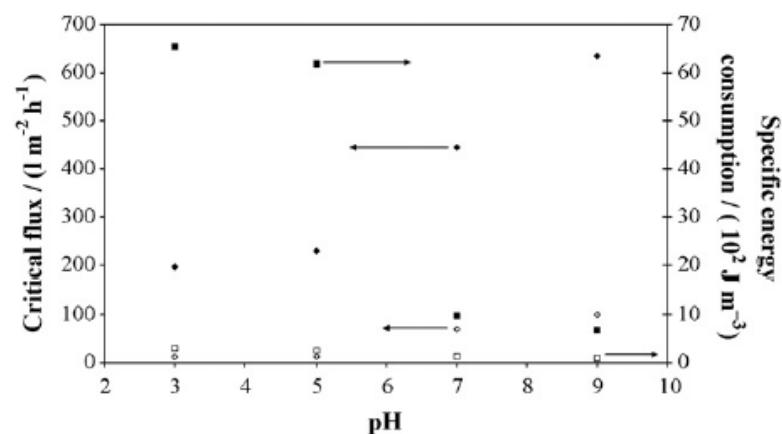


**Figure 2.8** The effect of PH to flux [15].

## 2.5 Flow in porous media

Yuan Wang et al 2012. [20] studied the factor which effected in the synthetic of waste water in membrane bioreactor system. They developed the hydrodynamics factor by inserting the hallow fiber membrane bundle which was the porous media into the system for increasing the residence time (reducing velocity). When fluid had a sufficient time for reacting with membrane bioreactor that the production of synthetic waste water was more increased than high velocity. They used computational fluid dynamics to predict the phenomena that occurred in system by adding flow in porous media equation in equation 2.1, which had a viscous loss term and inertial loss term. From the figure 2.9 showed that result of membrane bioreactor system that inserting the hollow fiber membrane bundle had a lower velocity than un-insert system.

$$S_i = (\sum_{j=1}^{3} D_{ij}\mu V_j + \sum_{j=1}^{3} C_{ij}\frac{1}{2}\rho V_j V_{mag})$$

Viscous loss term   Inertia loss term                    (2.1)

Where;

$$\nabla P = -\frac{\mu}{\alpha}\vec{v}$$

In laminar flow through porous media, the pressure drop is proportional to velocity by ignoring inertial loss term and reducing to Darcy's law
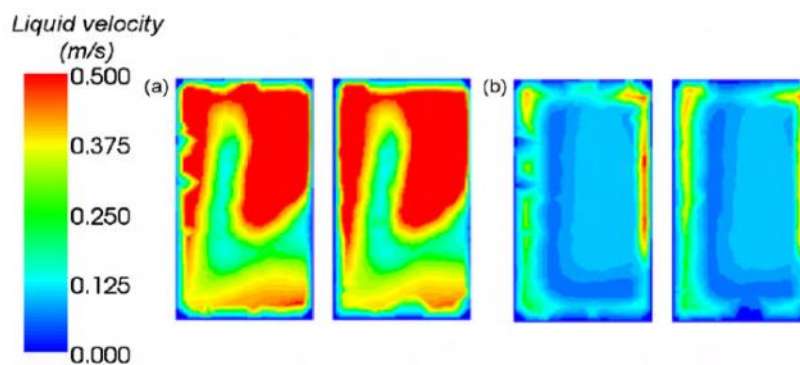


**Figure 2.9** The velocity of membrane reactor without membrane (a) and inserted the hallow fiber membrane bundle (Wang et al 2010)

## 2.6 Flow in porous media model.

Porous media modeled in Fluent user guide (2013) [21] are modeled by the addition of a momentum source term to the momentum equation in equation (2.2-2.3). The source term compose of a viscous loss term and an inertial loss term. For this thesis, loss term which cause the resistance of membrane that effect to flow of fluid in membrane's pore [21]

$$S_i = (\sum_{j=1}^{3} D_{ij}\mu v_j + \sum_{j=1}^{3} C_{ij}\frac{1}{2}\rho v_j|v|)$$

Where; $S_i$   is source term for the momentum equation

$D_{ij}$   is viscous resistance factor        $C_{ij}$   is inertial resistance factor

$\mu$    is dynamics viscosity (Pa.s)        $v_j$   is liquid velocity in j direction (m/s)

$|v|$   is velocity magnitude (m/s)        $\rho$   is density of fluid (kg/m$^3$)

For homogeneous porous

$$S_m = -(\frac{\mu}{\alpha} v_i + C_2 \frac{1}{2} \rho |v| v_i) \qquad (2.2)$$

Where; μ   is viscosity of fluid (Pa.s)       α    is permeability of membrane (1/m)

$v$   is velocity of fluid (m/s)       C2   is inertial resistance (1/m)

ρ   is density of fluid (kg/m3)       $|v|$   is magnitude of velocity (m/s)

In laminar flow through porous media, the pressure drop is proportional to velocity by ignoring inertial loss term and reducing to Darcy's law

$$\nabla P = -\frac{\mu}{\alpha} \vec{v} \qquad (2.3)$$

The pressure drop that fluent computes in x, y, and Z coordinate

$$\Delta P_x = \sum_{j=1}^{3} \frac{\mu}{\alpha_{xj}} v_j \Delta n_x \ , \qquad \Delta P_y = \sum_{j=1}^{3} \frac{\mu}{\alpha_{yj}} v_j \Delta n_y \quad , \qquad \Delta P_z = \sum_{j=1}^{3} \frac{\mu}{\alpha_{zj}} v_j \Delta n_z$$

Where;  μ   is viscosity of fluid (Pa.s)        α is permeability of membrane (1/m)

$\Delta n$   is the thickness of medium (m)

$v_j$   is velocity components in x, y, and z direction (m/s)

## 2.7 CFD simulation of effect of baffle in turbulence flow, tubular microfiltration membrane

Lui et al 2012 [9]used CFD simulation to study the effects of the position of baffle on flow channel (i.e., central baffles, wall baffles, and no-baffles) at condition; clean water (no particle), turbulence flow, velocity inlet was 0.5m/s, and pressure outlet was 50KPa. The result showed that although in this system is turbulence flow but near membrane surface, the flow regime was laminar where velocity was low. Thus, particles could be accumulated on membrane surface. Baffle could induce turbulence flow near membrane surface that effected to increase sheer rate to prevent the accumulation of particle. Figure 2.10 it elucidated that central baffle achieved higher flux than the others. Although on the central of channel, central baffle had a lower velocity than the others but where did not influence to filtration flux. On the other hands near the membrane surface which velocity of central baffle had higher than the others that velocity could prevent the accumulation of particle on membrane surface which influence to increase filtration flux.
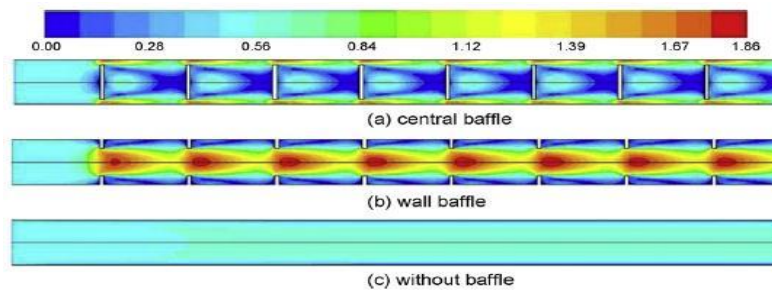
**Figure 2.10** Velocity contour of microfiltration inserted baffle a) central baffle b) wall baffle c) no baffle (Lui et al 2012)

## 2.8 Turbulence flow model.

The flow field is assumed to be single phase, incompressible and Newtonian. The effect of particles on the flow field is negligible and is not taken into account. The RANS equations will be used as the governing equations to transport the flow field quantities. LES is computationally intensive and needs several computers using the same jobs to process different datasets on different CPU''s simultaneously. DNS is expensive for the current problem and not available in FLUENT [21].

The turbulent models widely used in microfiltration membrane process are the standard k-ε, and renormalization group (RNG) k-ε [22]. The standard k-ε model is the most often used in practical engineering flow calculation [22]. It is based on high Reynolds number assumption. However, in case of swirling flow, the RNG k-ε model is more suitable as it comprises improved turbulent model parameters for swirling flow [22]. Since baffles, which induced swirling flow in microfiltration system, were applied in this study, the RNG k-ε turbulence model was used. Moreover, S. Ahmed et al (2011) [23] used RNG k-ε turbulence model to predict the velocity profile that effected by swirling from the baffle in microfiltration system and the results shown that simulation results were agree with experiment results. The RNG k-ε turbulence model in Fluent user guide (2013) was shown in equation 2.4-2.5.

$$\frac{\partial}{\partial t}(\rho k) + \frac{\partial}{\partial x_i}(\rho k u_i) = \frac{\partial}{\partial x_j}\left(\alpha_k \mu_{eff}\frac{\partial k}{\partial x_j}\right) + G_k + G_b - \rho\varepsilon - Y_M \tag{2.4}$$

and

$$\frac{\partial}{\partial t}(\rho \varepsilon) + \frac{\partial}{\partial x_i}(\rho \varepsilon u_i) = \frac{\partial}{\partial x_j}\left[\alpha_\varepsilon \mu_{eff}\frac{\partial \varepsilon}{\partial x_j}\right] + C_{1\varepsilon}\frac{\varepsilon}{k}(G_k + C_{3\varepsilon}G_b) - C_{2\varepsilon}\rho\frac{\varepsilon^2}{k} - R_\varepsilon + S_\varepsilon$$

$$\tag{2.5}$$

Rearrange so that equation can be expressed as

$$\frac{\partial}{\partial t}(\rho\varepsilon) + \frac{\partial}{\partial x_i}(\rho\varepsilon u_i) = \frac{\partial}{\partial x_j}\left[\alpha_\varepsilon \mu_{eff}\frac{\partial\varepsilon}{\partial x_j}\right] + C_{1\varepsilon}\frac{\varepsilon}{k}(G_k + C_{3\varepsilon}G_b) - C^*_{2\varepsilon}\rho\frac{\varepsilon^2}{k}$$

, where $C^*_{2\varepsilon}$ is given by

$$C^*_{2\varepsilon} = C_{2\varepsilon} + \frac{C_\mu \eta^3 (1 - \eta/\eta_0)}{1 + \beta\eta^3}.$$

Where;

| | | |
|---|---|---|
| k | = | Turbulent kinetic energy |
| $\varepsilon$ | = | Dissipation rate of turbulent kinetic energy |
| $G_k$ | = | Generation of turbulent kinetic energy due to the mean velocity gradient |
| $G_b$ | = | Generation of turbulent kinetic energy due to buoyancy |
| $Y_m$ | = | Contribution of the fluctuating dilation in compressible turbulence to the overall dissipation rate |
| $C_{1\varepsilon}, C_{2\varepsilon}, C_{3\varepsilon}$ | = | Constant |
| $\sigma_k, \sigma_\varepsilon$ | = | Turbulent Prandtl number of k and $\varepsilon$ respectively |
| $S_k, S_\varepsilon$ | = | User defined source term |
| $\alpha_k, \alpha_\varepsilon$ | = | Inverse effective Prandtl number for k, $\varepsilon$ respectively |
| $\mu_{eff}$ | = | Effective viscosity coefficient |
| $R_\varepsilon$ | = | Additional term of $\varepsilon$ equation |

## 2.9 The effect of velocity to particle dispersion

In figure 2.11 shows the particle force balance which the drag force exerted on the particle was determined by direction of fluid flow. Which was divided into two components i.e.,(parallel or perpendicular to the cross-flow). The lift force exerted on the particle in perpendicular with cross flow direction.
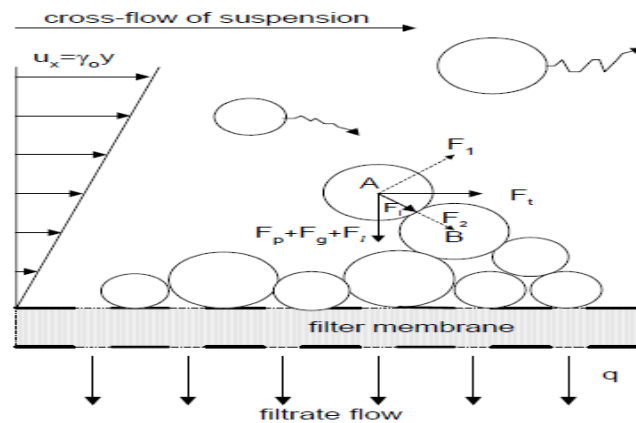
**Figure 2.11** Particle force balance [24].

$F_{dx}$ was drag force in the x-direction. When particles flowed adjacent to the membrane surface, which is the small velocity. The modified Stokes law can be employed to this equation [24]

$$F_{dx} = \frac{3}{4}\pi\mu d_p^2\gamma_0 C_x \tag{2.6}$$

Where; $\gamma_0$ is sheer rate at the membrane surface. Given by

$$\gamma_0 = \frac{6u_s}{H}$$

Where; $d_p$ is particle size (m)     $C_x$ is correction factor of shear flow

H is channel width (m)     $u_s$ is average cross flow velocity (m/s)

$F_{dy}$ was the frictional drag in the y-direction can also be calculated by using the modified Stokes law since the Reynolds number in the filtration direction is very small in most filtration. This force was exerting the particle to settle down on membrane surface [24].

$$F_{dy} = 3\pi\mu d_p u_y C_y \tag{2.7}$$

Where; $C_y$ is correction factor due to cake and membrane. Given by

$$C_y = 0.36(\frac{R_t' d_p^2}{4})^{-2/5}$$

$$u_y = q[1.5(1 - \frac{y}{H}) - 0.5\left(1 - \frac{y}{H}\right)^3]$$

Where; q is filtration rate     $\gamma_0$ is sheer rate at the membrane surface

y is channel height (m/s)     $u_y$ is fluid velocity in y direction

$R_t'$ is the total filtration resistance per unit thickness of cake

In equation 2.8 was the lift force.The lift force was the force in the y-direction opposite of frictional drag. This force lifted the particle not allow to settle down on membrane surface [24].

$$F_{lift} = 3\pi\mu d_p u_t C_y \qquad (2.8)$$

Where; $u_t$ was difined as

$$u_t = (\frac{61}{576v})(\frac{\tau_w}{\mu})^2(\frac{d_p}{2})^3$$

Where; $\tau_w$ is shear stress acting on the membrane surface

$v$ is the kinematic viscosity of liquid

In addition, Hwang et al (2001) [24] studied the influence of cross flow velocity that effect on the particle deposition on membrane surface at condition; water with polymethyl methacrylate (PMMA), inlet velocity was 0.2-0.4m/s, and particle size was 0.25-0.8μm. From the figure 2.12, the simulation result showed that layer of fouling cake on membrane surface was the most compact when operated cross flow velocity at 0.2 m/s. They elucidated by using particle force balance that operation at low cross flow velocity was increased cake fouling because at high inlet velocity had a higher  drag force in x-direction which forced the particle direction to move in x-direction. This force did not allow particles to settle down on membrane surface. Thus, operated at high inlet velocity had a low cake fouling on membrane surface.
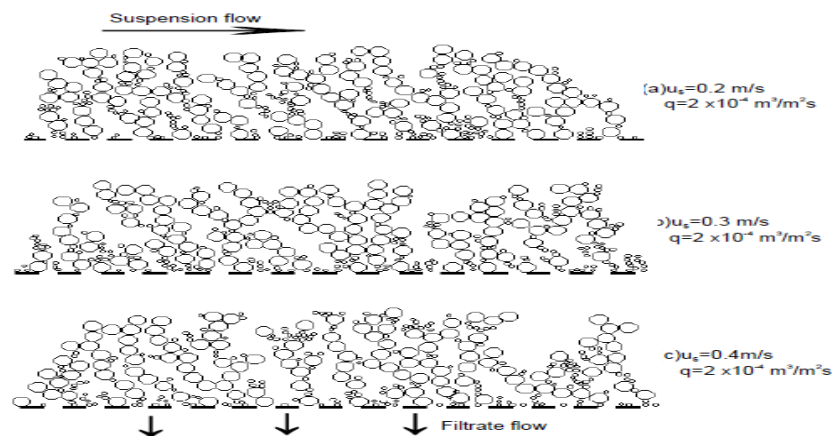


**Figure 2.12** The effect of velocity to formation of particle cake layer (Hwang et al 2001).

## 2.10 The effect of particle size to particle deposition

Altmann et al (1996) [25] studied the distribution of particle (silica) on the non-continuous cross-flow system. The information of particle distribution was elucidated by the balancing of drag force and lift force from equation (2.9-2.11). The

result showed in figure 2.14 that operation at higher filtration that drag force was higher than lift force the particle deposited on membrane surface The large particles had a higher lift , which overcame the drag force caused, the large particles did not settle down to the membrane surface. In contrast, small particle had a small lift force a drag force overcame lift force effected to the small particle was settled down to the membrane surface.

$$F_L = 0.761.\frac{\tau_w^{1.5}.x^3\rho^{0.5}}{\eta} \tag{2.9}$$

$$F_Y = F_{stoke} = 3.\pi.\eta.x.v_f \tag{2.10}$$

$$F_D = 6.33.\pi.\eta.x.w\left(\frac{x}{2}\right) = 3.16.\pi.\tau_w.x^2 \tag{2.11}$$

Where;  $F_L$ is lift force                    $F_y$ is drag force of filtrate flow (m/s$^2$)

   $F_D$ is drag force of cross-flow  (m/s$^2$)   $\tau_w$ is sheer stress

   x   is particle size (m)              $\rho$ is fluid density  (kg/m$^3$)

   $\eta$   is dynamic fluid viscosity        $v_f$ is filtration rate, flux (m$^3$/m$^2$.s)

   W is cross-flow velocity (m/s)
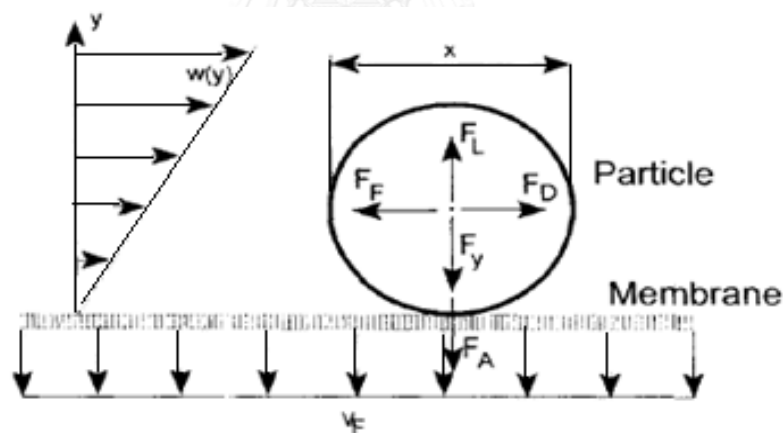


**Figure 2.13** Particle force balance (Altman et al 1996).
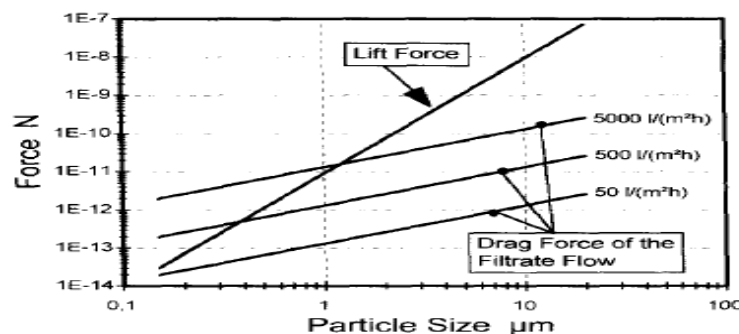


Fig. 7. Estimation of the forces on a streaming particle.

**Figure 2.14** The effect of particle size to lift force (Altman et al 1996).

## 2.11 Flow induced particle migration in micro-channels for improved microfiltration process

V. Dinther et al (2010) [26] studied the distribution of particle (Polymethyl methacrylate) at different size (i.e., small size = 1.53 um, and large size = 2.65 um) in fluid (Cyclohexylbromide). They elucidated by using inertial lift force, which causing the particle to migrate away from membrane surface. Inertial lift force dependent on particle Reynolds number (2.12). Generally, inertial lift force was effected when particle Reynolds number > 1.

$$Re_p = Re(2a(W + 2H)/4WH)^2 = \gamma a^2 \rho_P = \pi r^2 (W + 2H)/3n_\varphi W \qquad (2.12)$$

Where;   Re is Reynolds number       a is particle radius (m)

          W is channel width (m)        H is channel height (m)

          $\rho_P$ is density of particle (kg/m$^3$)   $n_\varphi$ is viscosity as function of particle

                                              volume

From figure 2.15, they found that particles with different sizes and sheer rate had different migration velocities. Larger particles interacted more easily with streamlines of fluid than smaller particles due to their size and thereby easily moved to other streamlines, leading to faster migration. As a result, larger particles would concentrate towards the middle of the channel while smaller particles were in the region close to the membrane surface. Moreover at higher sheer rate, the particles were migrated toward the middle of channel.
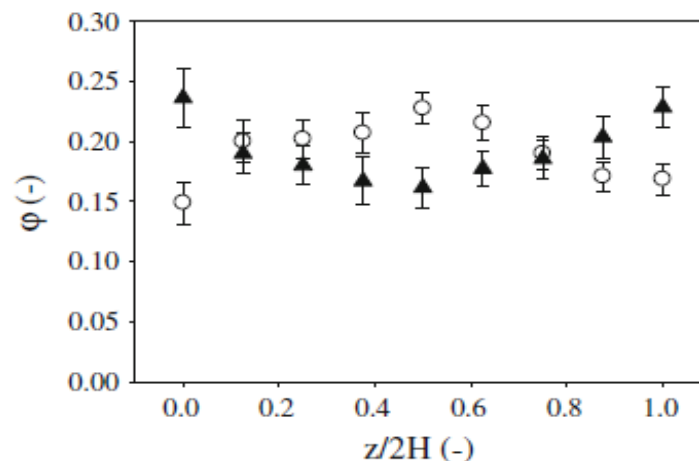


**Figure 2.15** The distribution of particles at different size in micro-channel (Dinther et al 2012).

## 2.12 CFD and experimental studies of fouling deposit on a microfiltration membrane

Rahimi et al (2010). [27] studied the influence of parameter (i.e., velocity inlet, and pressure outlet) that effect on the particle deposition on membrane surface at condition; water with Blue indigo suspension, laminar flow, velocity inlet was 0.5-1.3m/s, pressure outlet was 80KPa, and particle size was 0.4μm. From the figure 2.16a and b, the simulation results and experimental results showed that particle fouling on membrane surface occurred at lower velocity therefore at velocity inlet was 1.3m/s, the particle had not enough time (the lowest residence time) for settling down on the membrane surface.
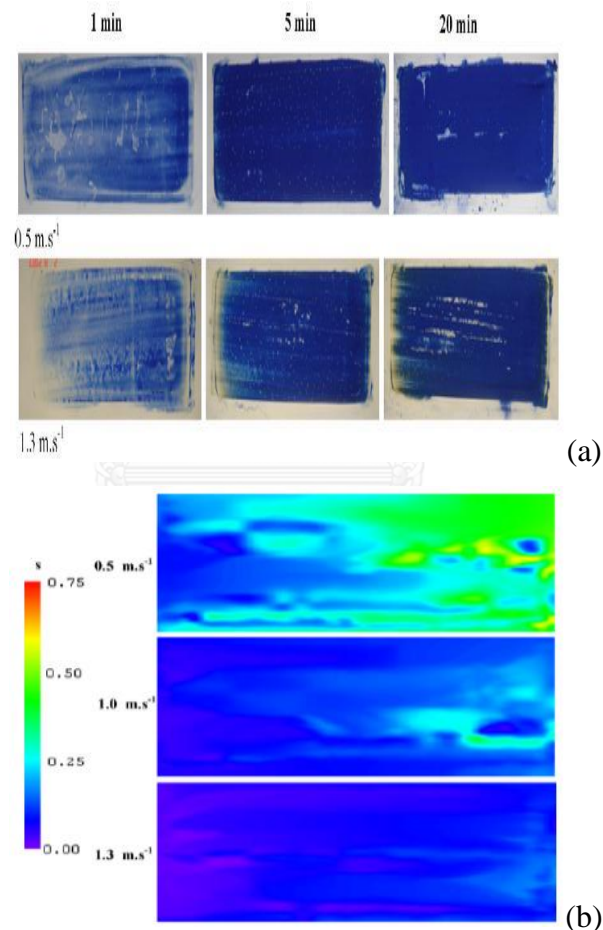


**Figure 2.16** a) The experimental results of the distribution of particle at different velocity inlet
b) The simulation result of the residence time of particle at different inlet velocity (Rahimi et al 2010)

**2.13 Discrete phase model.**

In equation (2.13-2.14) is the discrete phase model in Fluent user guide (2013). This force balance equates the particle inertia with the forces acting on the particle (i.e., drag force, gravity force, and other force). In addition to solving transport equations for the continuous phase, Fluent allows to simulate a discrete second phase in a lagrangian frame of reference. This second phase consists of spherical particles dispersed in the continuous phase (fluid phase). Fluent computes the trajectories of these discrete phase entities, as well as the coupling between the phases and its impact on both the discrete phase trajectories and the continuous phase can be include [16].

$$\frac{du_p}{dt} = F_D(u - u_p) + \frac{g_i(\rho_p - \rho)}{\rho_p} + F_i \qquad (2.13)$$

Where;  $F_D$ is drag force (m/s$^2$)     u is fluid velocity (m/s)

$u_p$ is particle velocity (m/s)     $g_i$ is gravitational force (m/s$^2$)

$\rho$ is fluid density (kg/m$^3$)     $\rho_p$ is particle density (kg/m$^3$)

$F_i$ is other force (Thermophoretic force, Brownian force, and Saftman's lift force )

Where; $F_D(u - u_p)$ is drag force per unit particle (m/s$^2$) and $F_D$ is define as

$$F_D = \frac{18\mu}{\rho_p d_p^2} \frac{C_D R_e}{24}$$

Relative Reynolds number, Re is define as

$$R_e = \frac{\rho d_p |u_p - u|}{\mu}$$

Drag coefficient, $C_D$ is define as

$$C_D = a_1 + \frac{a_2}{Re} + \frac{a_3}{Re^2}$$

Where $a_1$, $a_2$, and $a_3$ are constants that apply to smooth spherical particles over several ranges of Re given by Morsi and Alexander

$$C_D = \frac{24}{Re_{sph}}\left(1 + b_1 Re_{sph}^{b2}\right) + \frac{b_3 Re_{sph}}{b_4 + Re_{sph}}$$

Where $b_1$, $b_2$, $b_3$, and $b_4$ are taken from Haider and Levenspiel .

$$b_1 = \exp(2.3288 - 6.4581\emptyset + 2.4486\emptyset^2$$
$$b_2 = 0.0964 + 0.5565\emptyset$$
$$b_3 = \exp(4.905 - 13.8944\emptyset + 18.4222\emptyset^2 - 10.2599\emptyset^3)$$
$$b_4 = \exp(1.4681 + 12.2584\emptyset - 20.7322\emptyset^2 + 15.8855\emptyset^3)$$

Shape factor, $\emptyset$ is define as

$$\emptyset = \frac{s}{S}$$

Where; s is the surface area of a sphere having the same volume as the particle, and S is the actual surface area of the particle. The Reynolds number $Re_{sph}$ is computed with the diameter of a sphere having the same volume.

Saffman's lift force or lift force due to shear, is the additional force as an option in fluent  discrete

$$\vec{F} = \frac{2Kv^{\frac{1}{2}}\rho d_{ij}}{\rho_p d_p (d_{lk}d_{kl})^{\frac{1}{4}}}(\vec{u} - \vec{u_p}) \tag{2.14}$$

Where; K is constant coefficient saffman's lift force equal to 2.594, $v$ is kinematic

viscosity, and $d_{ij}$, $d_{lk}$, $d_{kl}$ are the deformation tensor.

## 2.14 Particle collision

Allen et al.[28]studied the finite element model of a cricket ball impacting a cricket bat. The influence of parameter (i.e., the geometry of cricket bat) that effect on the cricket ball (particle) collision at condition; velocity inlet was 30 m/s. Cricket ball elasticity was measured the ball was thrown by bowling machine without spin (figure 2.17) then it was measured the apparent coefficient of restitution (ACOR) that ACOR was defined as the ratio of rebound to inbound of ball velocity (figure 2.18). The result was shown that ACOR was based on the impact position of the bat cricket and the simulation results were agree with experiment result.

$$V_b' = \frac{V_{b(\frac{m_b}{M}+\frac{m_b Z^2}{I}-e)}}{(1+\frac{m_b}{M}+\frac{m_b Z^2}{I})} \tag{2.15}$$

Where; $V_b'$ is rebound velocity (m/s)      $V_b$ is inbound velocity (m/s)

  $m_b$ is mass of the ball (kg)      M is mass of the cricket bat (m/s$^2$)

  I   is the MOI of cricket bat      e   is coefficient of restitution

$Z$   is impact distance from center of mass (m)
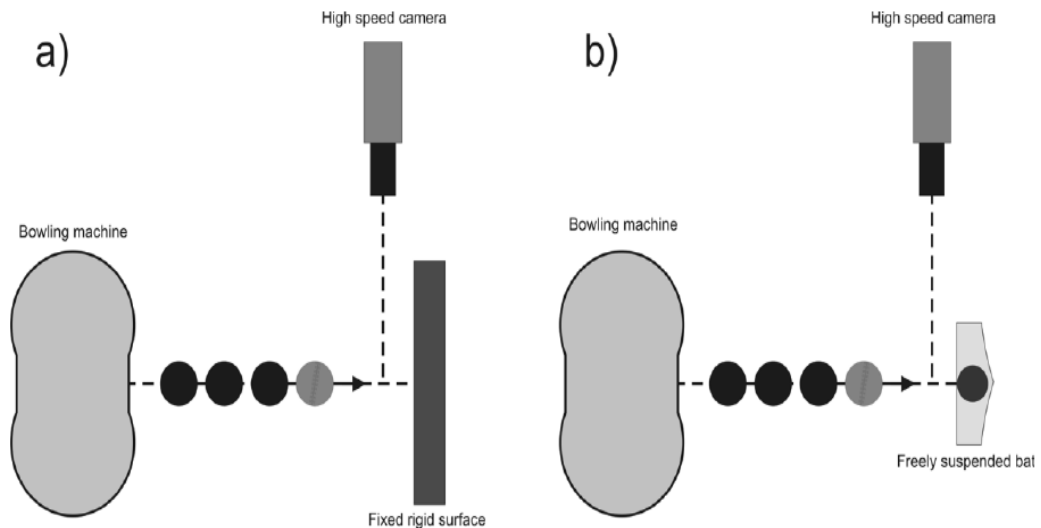


**Figure 2.17** The measurement of ACOR value (Allen et al 2014).
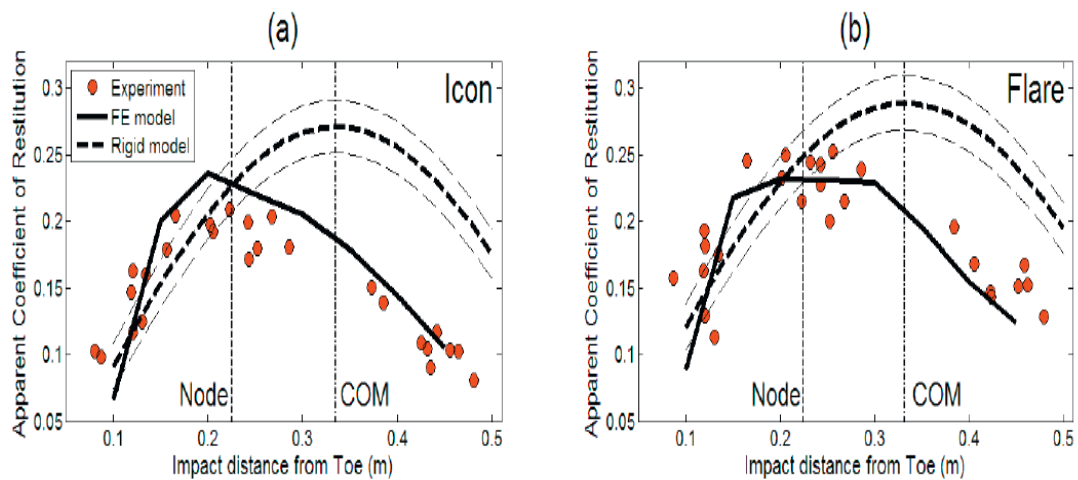


**Figure 2.18** The effect of cricket bat type to ACOR value a) icon bat b) flare bat (Allen et al 2014).

## 2.15 Particle collision boundary

In CFD FLUENT set the particle rebounds boundary was the coefficient of restitution (Figure 2.19). The normal coefficient of restitution defines the amount of momentum in the direction normal to the wall that is retained by the particle after the collision with the boundary where $v_n$ is the particle velocity normal to the wall and the subscripts 1 and 2 refer to before and after collision, respectively. Similarly, the tangential coefficient of restitution, defines the amount of momentum in the direction

tangential to the wall that is retained by the particle. A normal or tangential coefficient of restitution equal to 1.0 implies that the particle retains all of its normal or tangential momentum after the rebound (an elastic collision). A normal or tangential coefficient of restitution equal to 0.0 implies that the particle retains none of its normal or tangential momentum after the rebound. Non constant coefficients of restitution can be specialized for wall zones with the reflect type boundary condition.
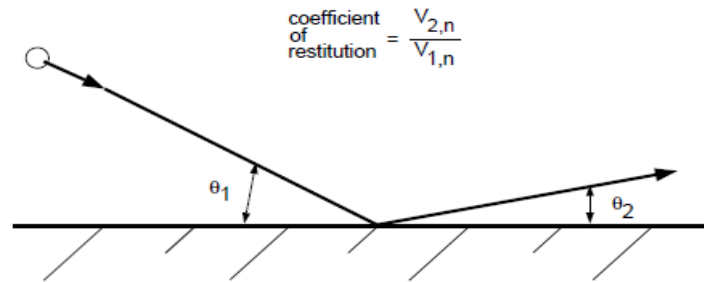


**Figure 2.19** "Reflect" boundary condition for the discrete phase [21].

## 2.16 Model and validation results of microfiltration membrane (no fouling)

Lixin et al (2011) [29] used CFD simulation to compare the effects of geometry of baffle (i.e., square bar baffle, cylindrical baffle, and no-baffle) for enhancing flux in microfiltration system. They used flow in porous media equation couple with momentum equation for solving the problem at condition; clean water (no fouling), laminar flow, velocity inlet was 0.46 m/s, pressure outlet was 2MPa, and temperature was 293 K.

Simulation results were compared with the experimental results by using flux to validate from equation (2.16)

$$J = \frac{TMP}{\mu.R_m}$$

(2.16)

Where;　J　is flux (m/s)　　　　　　　$\mu$　is viscosity of fluid (Pa.s)

　　　　$R_m$ is membrane resistance (1/m)　　TMP is trans-membrane pressure (Pa)

In figure 2.20, the result showed that cylindrical baffle had a higher flux than the others because from the stream line, rod baffle can be obstacle the direction of fluid in flow-channel to perpendicular with membrane surface. However the higher pressure-drop occurred when inserted the baffle in the system.
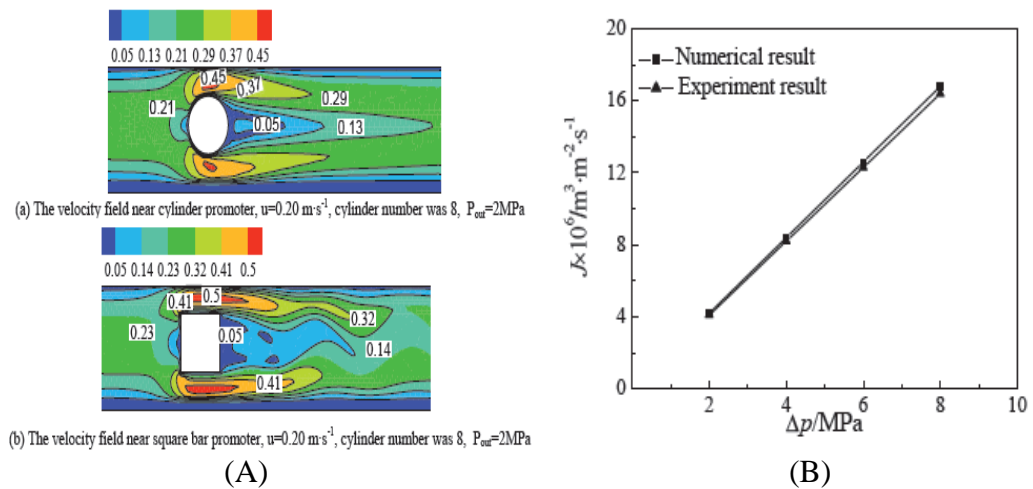
**Figure 2.20** The simulation result of A) Velocity contour, B) Validation of flux with clean water (Lixin et al 2011)

## 2.17 Model and validation results of microfiltration membrane with fouling

Gésan-Guiziou et al (2001) [10] studied the deposition of latex in cross flow tubular microfiltration system. They used equation 2.17 to find the water flux that effected from fouling in the system at condition; water, latex substance size was $4 \times 10^{-7}$m, pH was 7.0, velocity inlet was 0.5m/s, and temperature was 323K.

$$ J = \frac{TMP}{\mu.(R_m + R_f)} \tag{2.17} $$

Where;  J    is flux (m/s)                    $\mu$ is viscosity of fluid (Pa.s)

  $R_f$    is fouling resistance (1/m)          $R_m$ is membrane resistance (1/m)

  TMP is trans-membrane pressure (Pa)

In figure 2.21 a, the substances collected on the membrane surface and, over a period of operation time, cause fouling which obstructs the flux. This effected to decrease the flux in the system (figure 2.20 b).

(a)                                    (b)
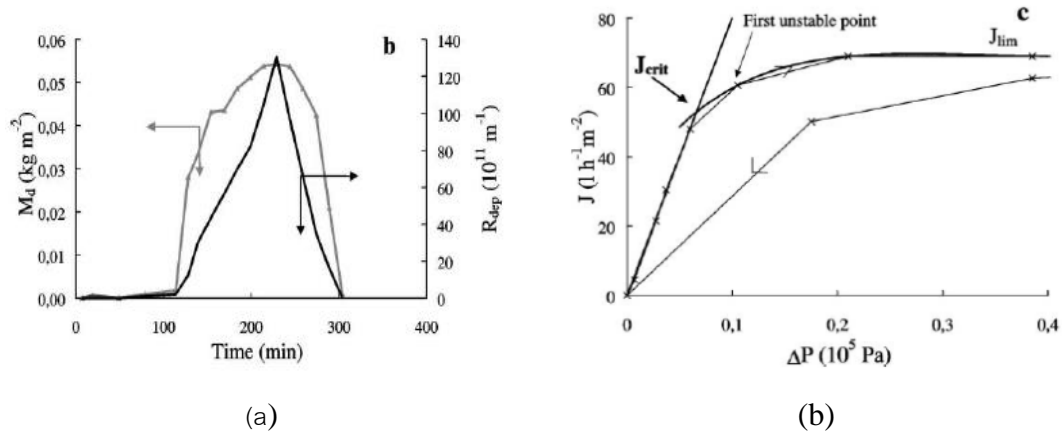
**Figure 2.21** Effect of fouling resistance to flux
a) Fouling resistance versus time b) Plot of flux versus trans-membrane pressure
(Gésan-Guiziou et al 2001)

## 2.18 Critical flux determination

The critical flux ($J_c$), the first point of flux was effected by fouling. From figure 2.22b the critical flux was the first none linear point in the graph. Operation under critical flux can prevent the effect of fouling on membrane surface. Gésan-Guiziou et al (2001) [10] demonstrated to measure critical flux by step-by-step technique.

Procedure of step for critical flux determination

- Increase trans membrane pressure (figure 2.22a)

- Wait for 30 minutes (figure 2.22a)

- Measure flux (figure 2.22a)

- Repeat step 1, 2, and 3 by increasing trans-membrane pressure.

- Plot permeation flux with trans-membrane pressure (from figure 2.22a to 2.22b) , provided that the first unstable point of curve  that start to nonlinear is the critical flux
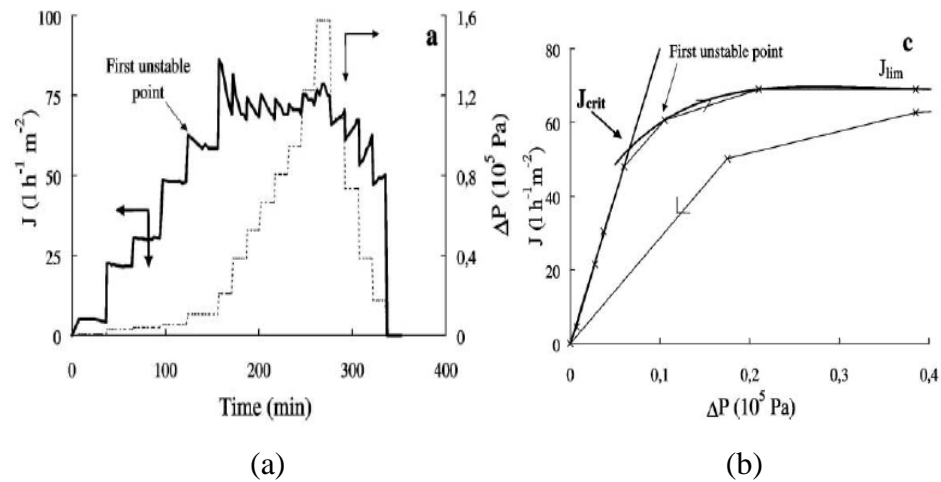
**Figure 2.22** Determination of the critical flux a) Plot of flux and trans-membrane, versus time   b) Plot of flux versus trans-membrane pressure
(Gésan-Guiziou et al 2001)

## 2.19 Energy consumption determination

The energy consumption ($E_p$), or the energy required for the pump in order to achieve a specific flux value, can be expressed as follows [30].

$$E_P = \frac{P_L Q}{J_c S} = \frac{\text{Dissipated power}}{J_c S} \qquad (2.17)$$

Where;  $P_L$ is trans-membrane pressure (Pa)      Q is inlet volumetric flow rate (m$^3$/s)
        $J_c$ is critical flux (m$^3$/m$^2$.s)      S  is membrane area (m$^2$)

# CHAPTER3

# MATERIAL AND METHOD

## 3.1 Approach

The velocity profile of fluid phase explained the particle distribution in microfiltration system by using CFD model. The CFD model was used to study the parametric study and type of baffle for an optimum condition. Finally, the energy consumption value was considered for a suitable operating point. Figure 3.1 shows the diagram of objectives in this research and the approach to achieve.
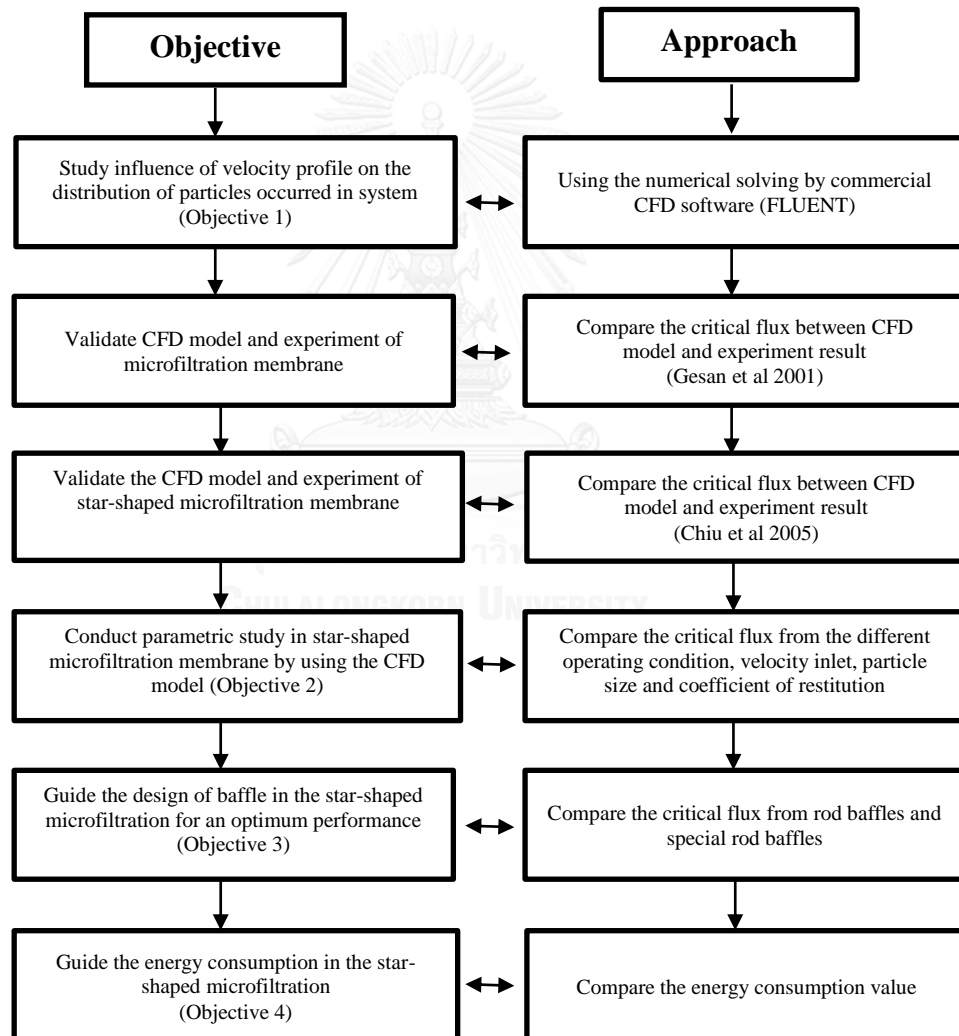


**Figure 3.1** The diagram of objectives in this research and the approaches to achieve the objectives.

## 3.2 Computational fluid dynamics of tubular and star shaped microfiltration membrane

Computational fluid dynamics (CFD) is a field of study solving fluid dynamics problems by means of numerical solution of conservation equations for mass, momentum and energy in flow regions of interest, coupled with additional equations relating to the problems [6]. CFD is a complement approach between theory and experimental approaches. It is a powerful approach as the research and design tools. There are three main steps for CFD simulation: (i) a pre-processor (ii) a solver (iii) a post-processor [16]

### 3.2.1 Pre-processor

In this step, the information such as computational domain, grid (mesh) generation, physical and chemical phenomena (i.e., governing equation), material properties, boundary and initial conditions, etc. is set up in CFD simulation software, Fluent ( Fluent 14.5, ANSYS Inc., Lebanon, NH., USA).

### 3.2.1.1 Geometry of tubular membrane

The geometry of the tubular microfiltration membrane in this study was built based on the system applied by Gesan et al. (2001). It consisted of seven channels that were 0.6 m long, $4.5 \times 10^{-3}$ m inner diameter, and with 0.03 $m^2$ membrane area. The geometry is shown in Figure 3.1. The boundaries of the tubular microfiltration are illustrated in figure 3.2 and table 3.1.
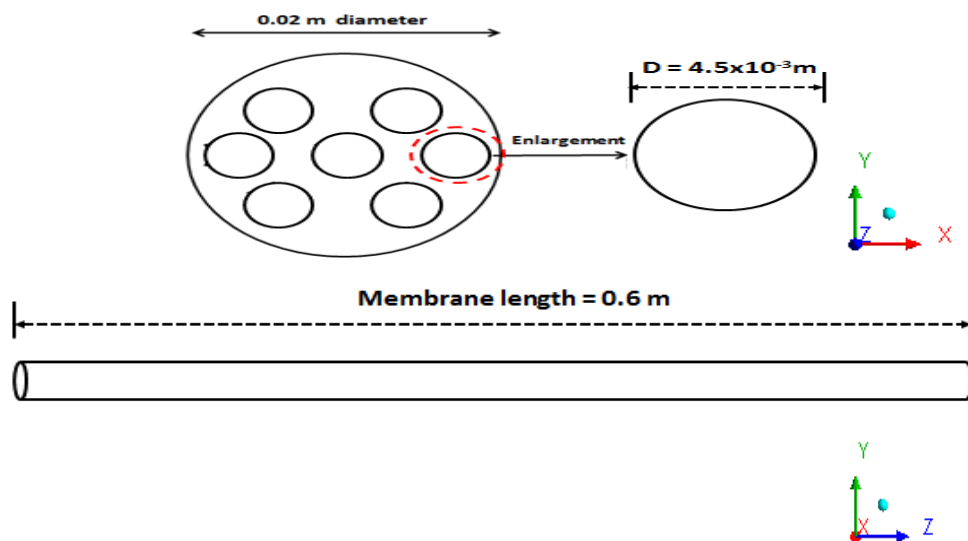


**Figure 3.2** Geometry and dimension of tubular microfiltration.
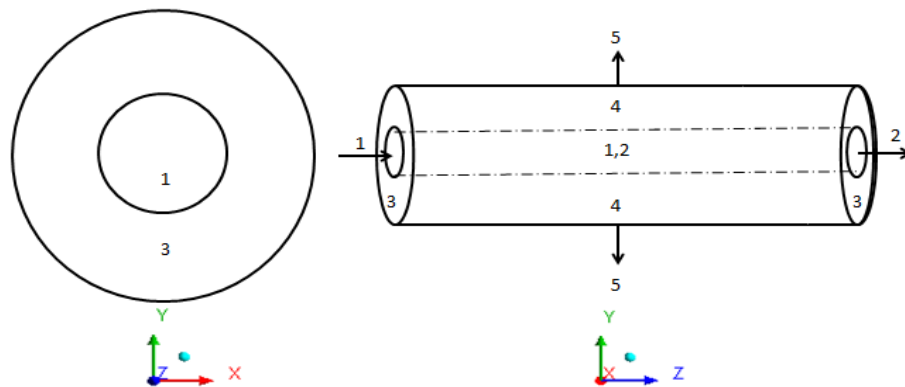
**Figure 3.3** Geometry and dimension of tubular microfiltration.

**Table 3.1** Boundary condition of tubular microfiltration.

| Number | Domain | Boundary type | Cell zone |
|--------|--------|---------------|-----------|
| 1 | Inlet (Feed stream) | velocity inlet | fluid |
| 2 | Outlet (retentate) | pressure outlet | fluid |
| 3 | wall of membrane | Wall | fluid |
| 4 | membrane | porous zone, interior | fluid |
| 5 | Outlet (permeate) | Pressure outlet | fluid |

### 3.2.1.2 Geometry of star-shaped membrane

The geometry of the star-shaped microfiltration membrane in this study was built based on the system applied by Chiu et al. (2006). It consisted of seven star-shaped channels that were 0.3m long, $4.6 \times 10^{-3}$ m in outer diameter, $2.8 \times 10^{-3}$ m in inner diameter, and with 0.03 $m^2$ membrane area. The geometry is shown in Figure (3.4-3.5). The boundaries of the star-shaped microfiltration are illustrated in figure 3.6 and table 3.2.
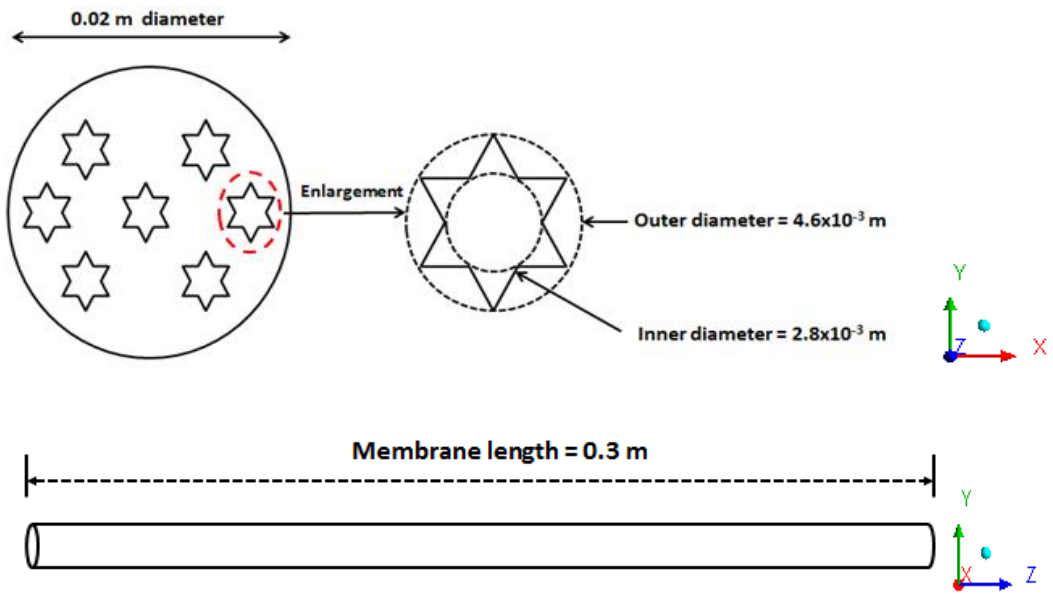
**Figure 3.4** The geometry and dimension of star-shaped microfiltration.
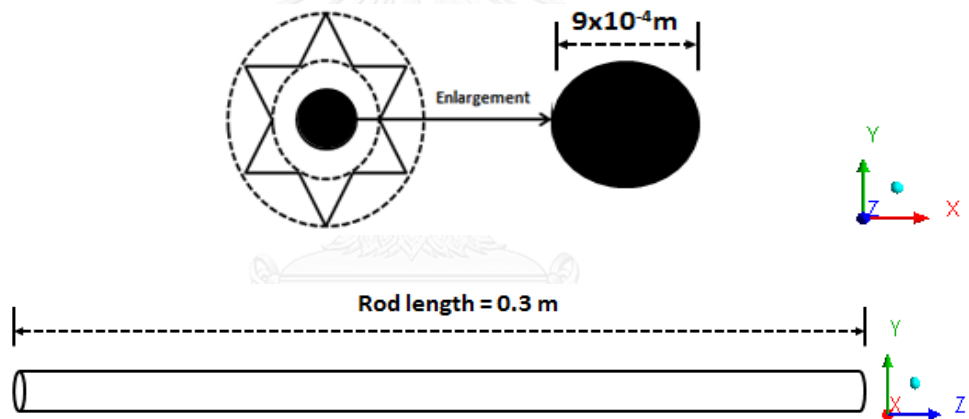


**Figure 3.5** The geometry and dimension of rod baffle
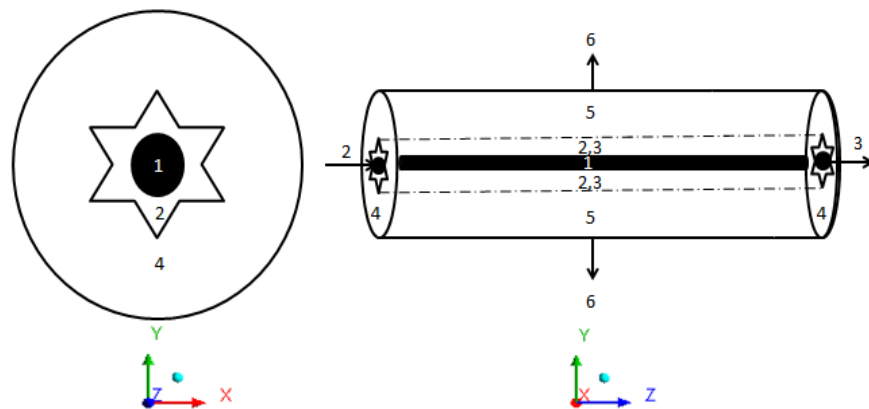


**Figure 3.6** The boundary condition of star-shaped microfiltration membrane and rod baffle.

**Table 3.2** Boundary condition of star-shaped microfiltration.

| Number | Domain | Boundary type | Cell zone |
|--------|--------|---------------|-----------|
| 1 | rod | Wall | solid |
| 2 | Inlet (Feed stream) | velocity inlet | fluid |
| 3 | Outlet (retentate) | pressure outlet | fluid |
| 4 | wall of membrane | Wall | fluid |
| 5 | membrane | porous zone, interior | fluid |
| 6 | Outlet (permeate) | Pressure outlet | fluid |

### 3.2.1.3 Computational meshing of tubular membrane

A three-dimensional computational geometry of the tubular microfiltration was created. Fine meshes were uniformly applied in the tubular channels in order to capture important flow details. The meshed geometry of the tubular microfiltration is shown in Figure 3.7 and table 3.3.
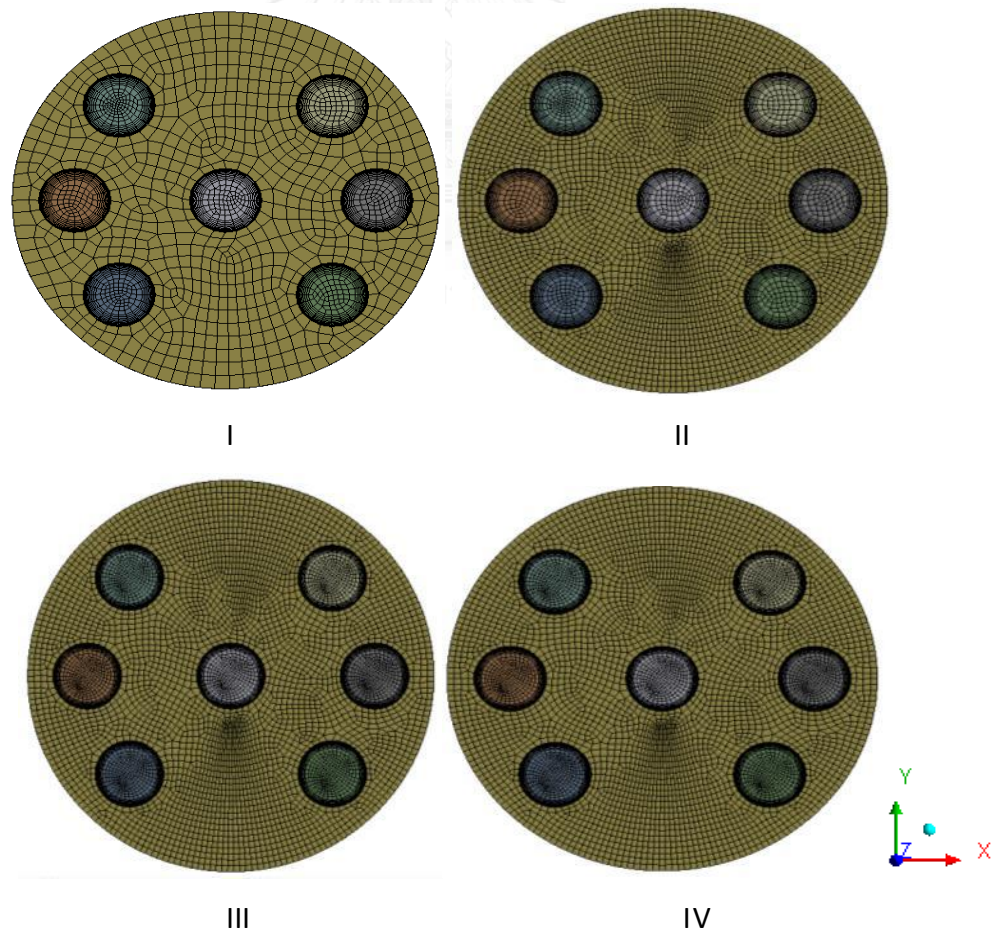


**Figure 3.7** The meshed geometry of the tubular microfiltration membrane.

**Table 3.3** Grid sensitivity analysis of tubular microfiltration.

| Grid number | Case | Number of grid |
|---|---|---|
| I | Coarse | 640000 |
| II | Medium | 1350000 |
| III | Fine | 2300000 |
| IV | Very Fine | 3170000 |

### 3.2.1.4 Computational meshing of star-shaped membrane

A three-dimensional computational geometry of the star-shaped microfiltration was created. Fine meshes were uniformly applied in the star-shaped channels in order to capture important flow details. The meshed geometry of the star-shaped microfiltration is shown in Figure 3.8 and table 3.4.



**Figure 3.8** The meshed geometry of the star-shaped microfiltration membrane.

**Table 3.4** Grid sensitivity analysis of star-shaped microfiltration

| Grid number | Case | Number of grid |
|---|---|---|
| I | Coarse | 820000 |
| II | Medium | 1870000 |
| III | Fine | 2890000 |
| IV | Very Fine | 4000000 |

### 3.2.2 Solver

#### 3.2.2.1 Simulation in fluent

The second step, after the meshes have been read into the solver, the partial differential equations (based on Navier-Stokes) are discretised over the meshes [21]. Then, a large set of nonlinear simultaneous equations is produced. To solve these, there are three distinct streams of numerical solution discretisation, including finite difference, and finite volume methods. The Finite Volume Method is a tool for solving the Navier-Stokes equations in Computational Fluid because it ensures that the discretization of governing equations is conservative. Moreover, it can be adjusted the unstructured meshes that mesh structure is necessary in the finite volume method.

The Navier-Stokes equations in FLUENT is a three-dimensional finite volume, mathematical model for solving incompressible, compressible, isothermal, and non-isothermal flow problems.

Unsteady term + Convective term = Diffusive term + Source term

$$\frac{\partial \rho \emptyset}{\partial t} + \nabla. (\rho \emptyset u) = \nabla. (\nabla \emptyset) + S_\emptyset \qquad (3.1)$$

Where; $\Gamma$ denotes the diffusivity and $S_\emptyset$ the source term. One can average Equation:

3.1 by integrating it over a three dimensional control volume, $\Omega_i$, of cell i,

$$\int_{\Omega_i} \frac{\partial \rho \emptyset}{\partial t} dV + \int_{\Omega_i} \nabla. (\rho \emptyset u) \, dV = \int_{\Omega_i} \nabla. (\nabla \emptyset) dV + \int_{\Omega_i} S_\emptyset dV \quad (3.2)$$

Applying the divergence theorem, Equation: 3.2 may be written as follows:

$$\int_{\Omega_i} \frac{\partial \rho \emptyset}{\partial t} dV + \int_{\partial \Omega_i} (\rho \emptyset u). n \, dS = \int_{\partial \Omega_i} (\nabla \emptyset). n dS + \int_{\Omega_i} S_\emptyset dV \quad (3.3)$$

Equation 3.3 is the basis of the formulation of finite volume method (FVM). Choosing appropriate properties for f, G and Sf , the generic transport equation can be transformed into the continuity and momentum equations. The other information of algorithms was shown in appendix C.

Numerical simulation of particle dispersion has two method for example; Eulerian and Lagragia. The fluid phase is always a continuum and can be solved by RANS simulation (Reynolds Average Navier Stoke). The Eulerian-Eulerian method controls particle trajectories by focusing on a control volume and consider particle as a continuum which develops particle trajectories based on conservation equation applied on control volume. The Eulerian-Largaranian method controls particle as a dispersed phase and tracks individual particles and the interparticle interaction is usually assumed to neglect. Guha et al. (2001) [31] noted that when particle motion is significantly affected by turbulence and the fluctuating flow field velocities become important, Lagrangian calculations are needed. Lagrangian approach provides a more detailed and realistic model of particle deposition because the instantaneous equation of motion is solved for each particle moving through the field of random fluid eddies.

### 3.2.2.2 Assumptions

The assumptions of this simulation for all models of star-shaped microfiltration system presented in this thesis are:

- The system is isothermal

- Incompressible and Newtonian fluid

- Neglect inertial loss in porous media

- The porosity of particle is 0.5

- Neglect interparticle interaction

- The particles are spherical shaped

- The particles are trapped on membrane surface

- No chemical reaction between fluid and particles

- Neglect thermophoretic force and brownian force in discrete phase model

- No porous in baffle

### 3.2.2.3 Initial and boundary condition

- **Initial condition of fluid**

At time was zero, it did not have a fluid in the microfiltration system. Thus, the inlet velocity = 0 m/s

$$u_t (0,x,y,z) = 0$$

- **Initial condition of particles**

At the start of the process, fouling resistance on membrane surface was zero and membrane resistance was constant which obtained from Chui et al (2005) and Gesan et al (2001).

$u_p (0,x,y,z) = 0$

$R_f (0,x,y,z) = 0$

$R_m (0,x,y,z) = constant$

Where; $2x10^{11}$ m$^{-1}$ (Chui's work), $4x10^{11}$ m$^{-1}$ (Gesan's work)

- **Bounary condition of fluid**

At any time from inlet channel of microfiltration membrane, inlet velocity was a constant velocity which obtained from Chui et al (2005) and Gesan et al (2001).

$u_t (t,0,0,0) = u_0$

$u_t (t,wall) = 0$ ,No-slip condition because fluid can not move.

- **Bounary condition of particles**

$u_p (t,0,0,0) = u_0$

$R_f (t,0,0,0) = variable ( 0 < t ≤ t_f)$

$R_m (t,0,0,0) = constant ( 0 < t ≤ t_f)$

Where; $2x10^{11}$ m$^{-1}$ (Chui's work), $4x10^{11}$ m$^{-1}$ (Gesan's work)

### 3.2.2.4 Physical and chemical property

**Table 3.5** Properties of variables used in the tubular membrane validation.

| Part | Parameter | value |
|---|---|---|
| Water (fluid phase) | Density ($\rho$) | 998.2 kg/m$^3$ |
| | Viscosity ($\mu$) | 1.003x10$^{-3}$ kg/m.s |
| | Molecular weight (MW) | 18 g/mol |
| Latex (solid phase) | Density($\rho$) | 1320 kg/m$^3$ |
| | Particle size ($d_p$) | 4x10$^{-7}$ μm |
| | Particle flow rate | 6.66x10$^{-8}$ kg/s |
| Tubular ceramic Kerasep (Membrane) | Membrane pore size | 1x10$^{-7}$ m |
| | Membrane resistance | 4x10$^{-11}$ m$^{-1}$ |

| Operation | Velocity inlet (u) | 0.5 m/s |
|-----------|--------------------|---------|
|           | Temperature (T)    | $25^0$c |

* These parameters were obtained from the journal [10].

**Table 3.6** Properties of variables used in the star-shaped membrane validation.

| Part | Parameter | value |
|------|-----------|-------|
| Water (fluid phase) | Density ($\rho$) | 998.2 kg/m$^3$ |
|  | Viscosity ($\mu$) | 1.003x10$^{-3}$ kg/m.s |
|  | Molecular weight (MW) | 18 g/mol |
| Peptone (solid phase) | Density($\rho$) | 1070 kg/m$^3$ |
|  | Particle size ($d_p$) | 4x10$^{-6}$ m |
|  | Particle flow rate | 2.23x10$^{-5}$ kg/s |
| CaCl$_2$.2H$_2$O (solid phase) | Density($\rho$) | 1850 kg/m$^3$ |
|  | Particle size ($d_p$) | 3x10$^{-5}$ m |
|  | Particle flow rate | 5.573x10$^{-7}$ kg/s |
| Meat extraction (solid phase) | Density($\rho$) | 990 kg/m$^3$ |
|  | Particle size ($d_p$) | 1.5x10$^{-6}$ m |
|  | Particle flow rate | 1.536x10$^{-5}$ kg/s |
| Urea (solid phase) | Density($\rho$) | 1335 kg/m$^3$ |
|  | Particle size ($d_p$) | 5x10$^{-6}$ m |
|  | Particle flow rate | 4.189x10$^{-6}$ kg/s |
| Mg$_2$SO$_4$.7H$_2$O (solid phase) | Density($\rho$) | 2570 kg/m$^3$ |
|  | Particle size ($d_p$) | 1.05x10$^{-5}$ m |
|  | Particle flow rate | 2.793x10$^{-7}$ kg/s |
| K$_2$HPO$_4$ (solid phase) | Density($\rho$) | 2440 kg/m$^3$ |
|  | Particle size ($d_p$) | 1.28x10$^{-6}$ m |
|  | Particle flow rate | 3.91x10$^{-6}$ kg/s |

| NaCl (solid phase) | Density($\rho$) | 2170 kg/m$^3$ |
| | Particle size ($d_p$) | 1.38x10$^{-5}$ m |
| | Particle flow rate | 9.77x10$^{-7}$ kg/s |
| Membrane (unplasticized polyvinyl chloride) | Membrane pore size | 2x10$^{-7}$ m |
| | Membrane resistance | 2x10$^{-11}$ m$^{-1}$ |
| Operation | Velocity inlet (u) | 3.27 m/s |
| | Temperature (T) | 25$^0$c |

* These parameters were obtained from the journal [3].

## 3.3 Post-processor

The final step, post-processor provides full-field data such as visualization result, geometry and grid display, vector plot, line and shaded contour plots, etc. at each and every point in the domain.

## 3.4 Model validation

The predictability of the CFD model in this study was validated by comparing the simulated values of the trans-membrane pressure (TMP) and the critical flux ($J_c$) through the membrane, as well as the energy consumption, with the experimental data of tubular microfiltration membrane from the literature [10] and experimental data of star-shaped microfiltration membrane from the literature [3]. The critical flux can be calculated as shown in equation (3.4).

$$J_c = \frac{TMP}{\mu(R_m + R_f)} \qquad (3.4)$$

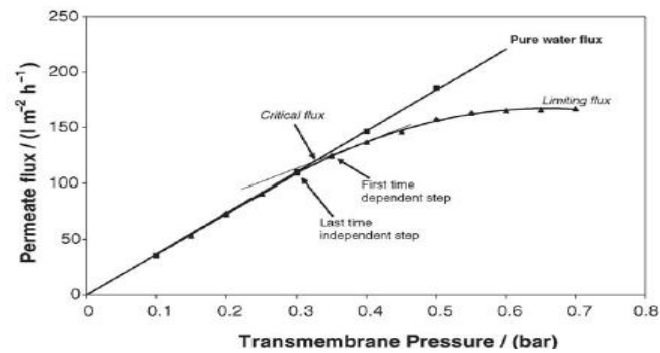Where; TMP is trans-membrane pressure (Pa)     $\mu$ is viscosity of fluid (Pa.s)

$R_f$ is fouling resistance (1/m)     $R_m$ is membrane resistance (1/m)

$R_m$ is the resistance of membrane (clean membrane) that find from slope of flux with Trans-membrane pressure is define as [23]

$$J = \frac{TMP}{\mu R_m} \quad : y = mx+c, \text{ slope} = 1/\mu R_m$$

**Figure 3.9** Plot of flux versus trans-membrane pressure of clean water (no fouling)
(Chui et al 2012)

$R_f$ is the resistance of fouling during accumulation of particles on membrane surface
is define as [10]

$$R_f = \alpha M_d$$

Where; $M_d$ is the deposited mass ($kg/m^2$) that calculated from simulation result

$\alpha$ is specific resistance (m/kg) is define as

$$\alpha = \frac{180(1 - \varepsilon)}{\varepsilon^3 \rho_s d_p^2}$$

Porosity of fouling, $\varepsilon$ Based on the Carman-Kozeny equation [10], the porosity can be
evaluated for spherical particles (Kozeny constant = 5)

## 3.5 Parametric study

In this study, we studied the effect of operating variable on column
performance. The parameter and range of variable were shown in Table 3.7. All of
results will be analyzed and discussed in the following topics in the next chapter:

- Effect of parameter to critical flux.

- Effect of parameter to fouling resistance.

- Effect of parameter to particle distribution.

**Table 3.7** Parametric study in star shaped microfiltration membrane.

| Parameter | Value |
|---|---|
| Velocity inlet | 2.5-4.0 m/s |
| Particle size (vary meat extraction size) | small = $3.75 \times 10^{-7}$ m, medium = $1.5 \times 10^{-6}$ m, large = $5 \times 10^{-6}$ m |
| Coefficient of restitution | 0.1-1 |

## 3.6 Baffle design

In this study, we studied the effect of geometry of baffle to column performance. The special geometry of baffle was inserted in to the star-shaped microfiltration at z =165, 240 mm (figure 3.10) All of results will be analyzed and discussed in the following topics in the next chapter:

- Effect of baffle to momentum transfer

- Effect of baffle to critical flux

- Effect of baffle to fouling resistance.

- Effect of baffle to particle distribution
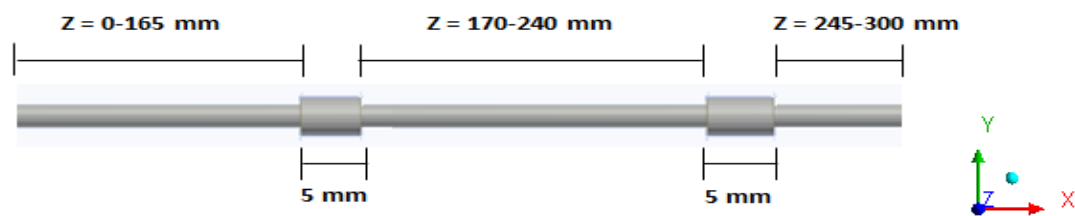


**Figure 3.10** The special rod geometry in star-shaped microfiltration membrane
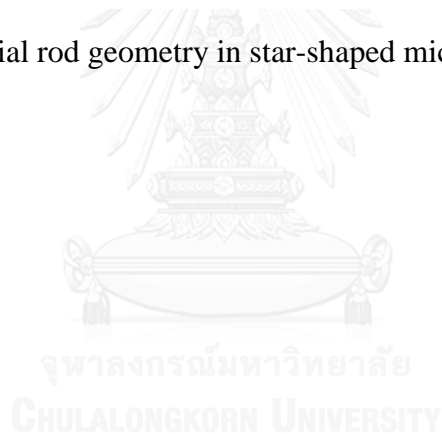
## CHAPTER4

## RESULTS AND DISCUSSTION

### 4.1 Grid sensitivity of tubular microfiltration membrane

Generally, the coarse grids give the large error of simulation results on the other hand the fine grids consume a large of computing time. Thus, every CFD simulation work must be operated the grid sensitive analysis. In this study, the effect of number of grid on simulate result were investigate. The structure grid was varied into four cases which is coarse grid (number of grid = 820000), medium grid (number of grid = 1870000), Fine grid (number of grid = 2890000) and very fine grid (number of grid = 4000000).The effect of grid number to simulation results as show below in Figure 4.1
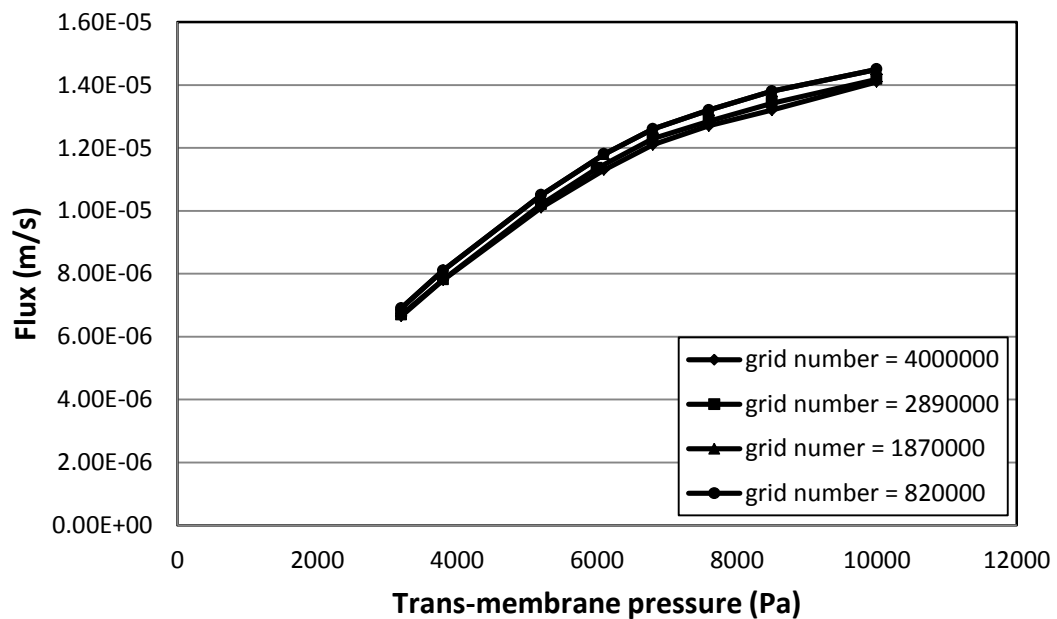


**Figure 4.1** Effect of number of grid to critical flux.

shows the effect of grid number to critical flux versus trans-membrane pressure. As results, the computing time increase significantly follows larger number of grid. The results show deviation of critical flux when grid is coarse (i.e., grid number of 820000); the simulated result using this grid resolution is different from the other grids which are finer. Furthermore, this study found that when using number of grid range of 1870000, 2890000 and 4000000, a little deviation was obtained (i.e., all result be overlapped). Thus, we can infer that in this range of grid the simulated result is seen independent from the size of grid. Moreover, the square shape of grid can offer

an orderliness that effected to use a less time for solving a problem than non-structured of grid.

## 4.2 Model validation of tubular microfiltration membrane

CFD simulation results were compared with the experiment result of the critical flux reported by Gésan-Guiziou et al (2001) to validate the predictability of the CFD model. The RNG k-ε turbulence model (Equation (2.4-2.5)) and the discrete phase model (Equation (2.13-2.14)) have been used to simulate momentum transport and particle distribution which affected the critical flux of the system. Figure 4.2 shows the comparison of the critical flux from the simulation was agreed with experiment result. The percent deviation of the experiment and simulation result was 14.8%. It was found that the simulation result was gradually deviated from experiment because the assumption of fouling in simulation work was the complete pore blocking. While, the mechanism of fouling in experiment may be a cake layer which the particles deposited on themselve. Therefore, the number of particle deposition on membrane surface in experiment was less than simulation work.
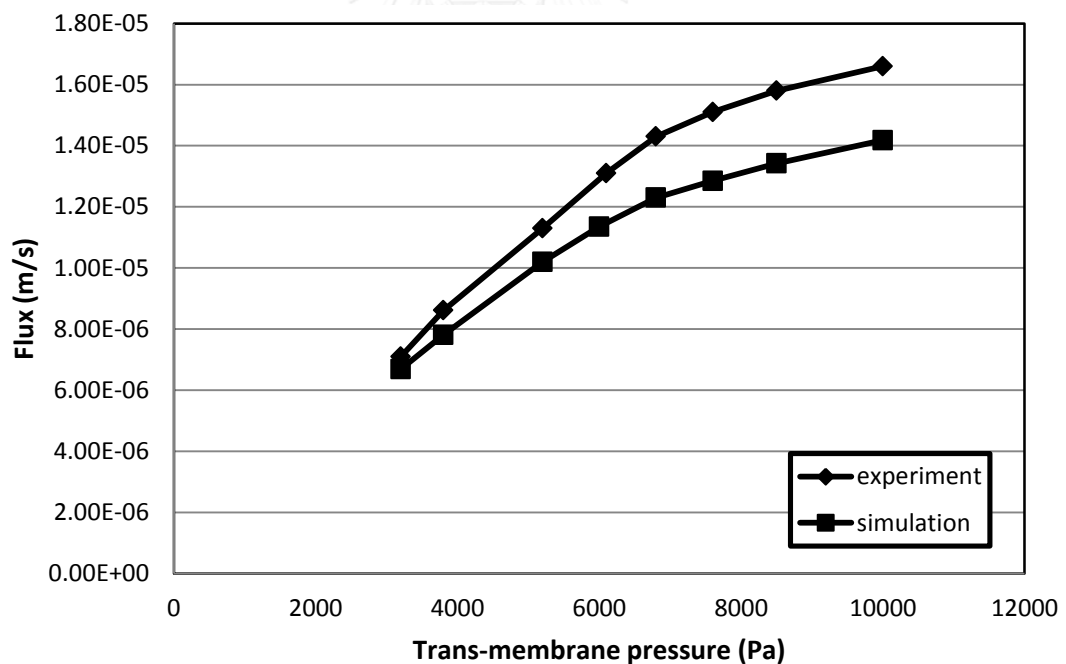


**Figure 4.2** Comparison of the critical flux from the simulation and the experimental measurement in tubular microfiltration membrane (Gésan-Guiziou et al 2001)

## 4.3 The Comparison of critical flux among tubular membrane, star-shaped membrane and star-shaped membrane with rod baffle from the CFD models

The critical flux of tubular membrane was compared with the star-shaped membrane and star-shaped membrane with rod baffle by using the same condition and mathematical models. Figure 4.3 shows the comparison of the critical flux from the star-shaped membrane with rod baffle, star-shaped membrane and the tubular membrane. It was shown that the critical flux of star-shaped membrane with rod baffle was $1.33 \times 10^{-5}$ m/s, which was higher than the critical flux from star-shaped membrane by 4.00 percent and tubular membrane by 8.13 percent. Using star-shaped microfiltration membrane, the fouling resistance was decreased (Figure 4.4). As a result, higher critical flux was founded when used star-shaped microfiltration membrane.
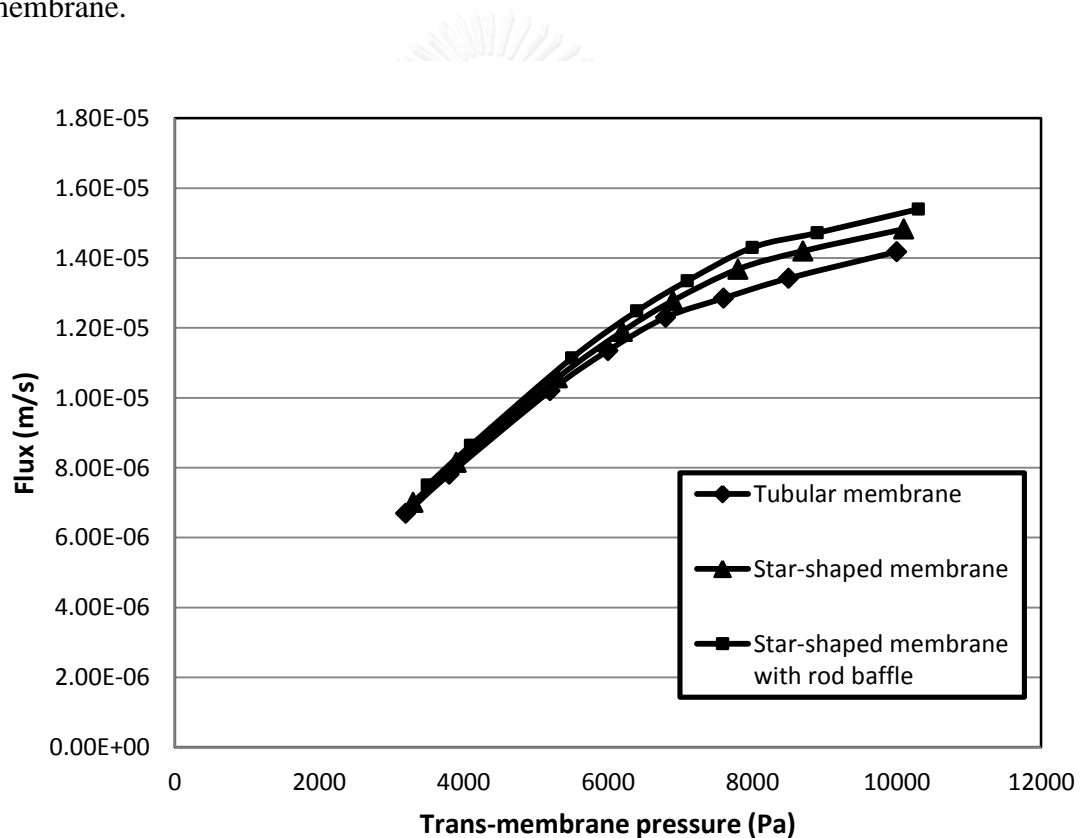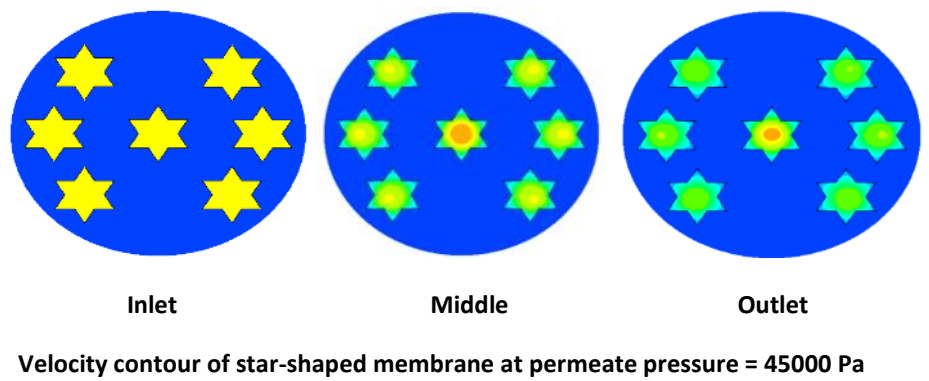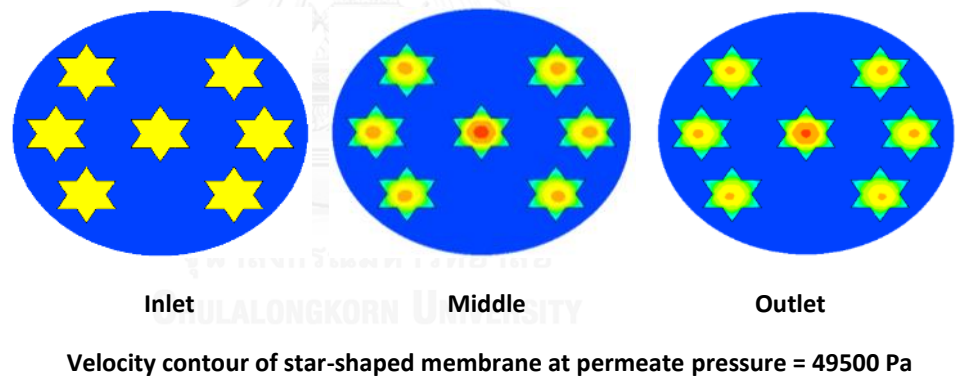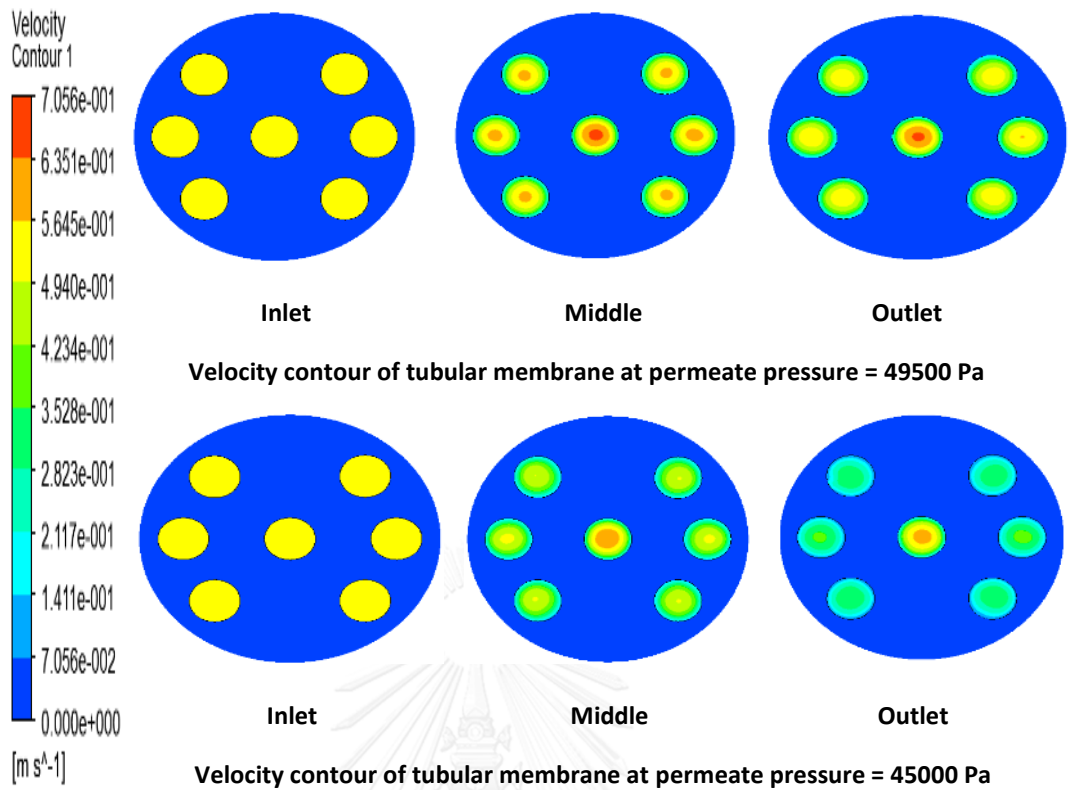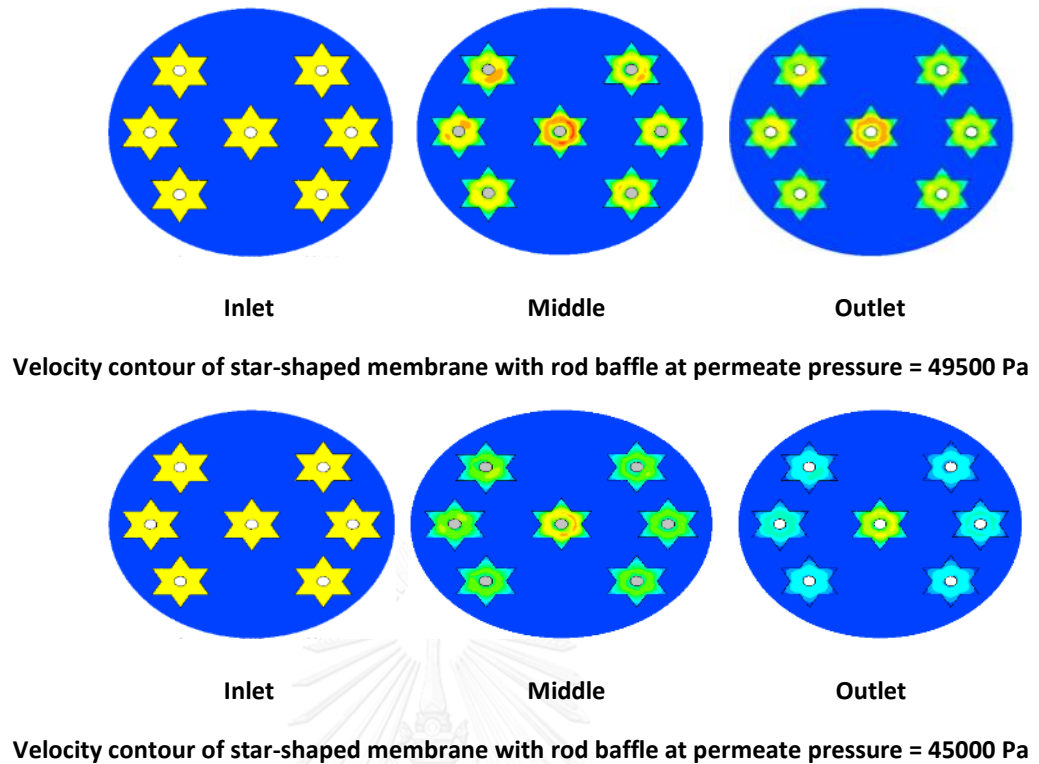


**Figure 4.3** Comparison of the critical flux from the tubular membrane, star-shaped membrane, and star-shaped membrane with rod baffle (at the same inlet velocity of 0.5 m/s, outlet pressure permeate pressure, and particle injection) by using the CFD model.
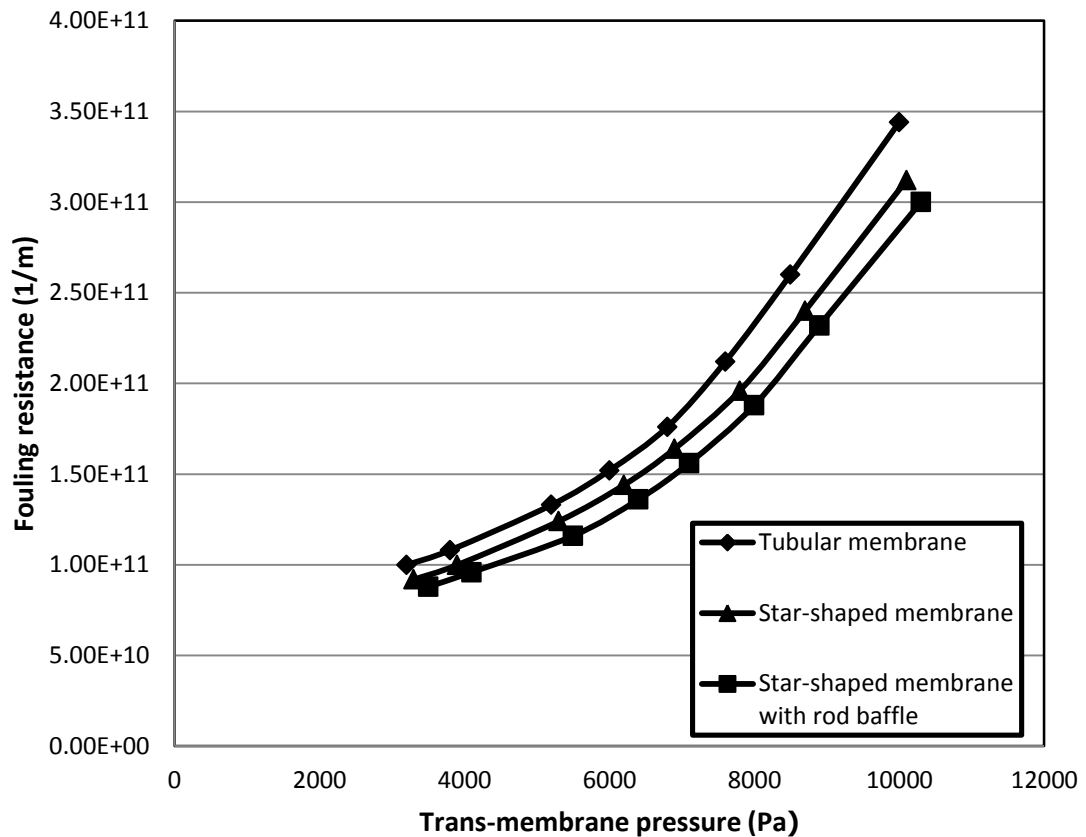
**Figure 4.4** Comparison of the fouling resistance from the tubular membrane, star-shaped membrane, star-shaped membrane with rod baffle (at the same inlet velocity of 0.5 m/s, outlet pressure permeate pressure, and particle injection) by using the CFD model.
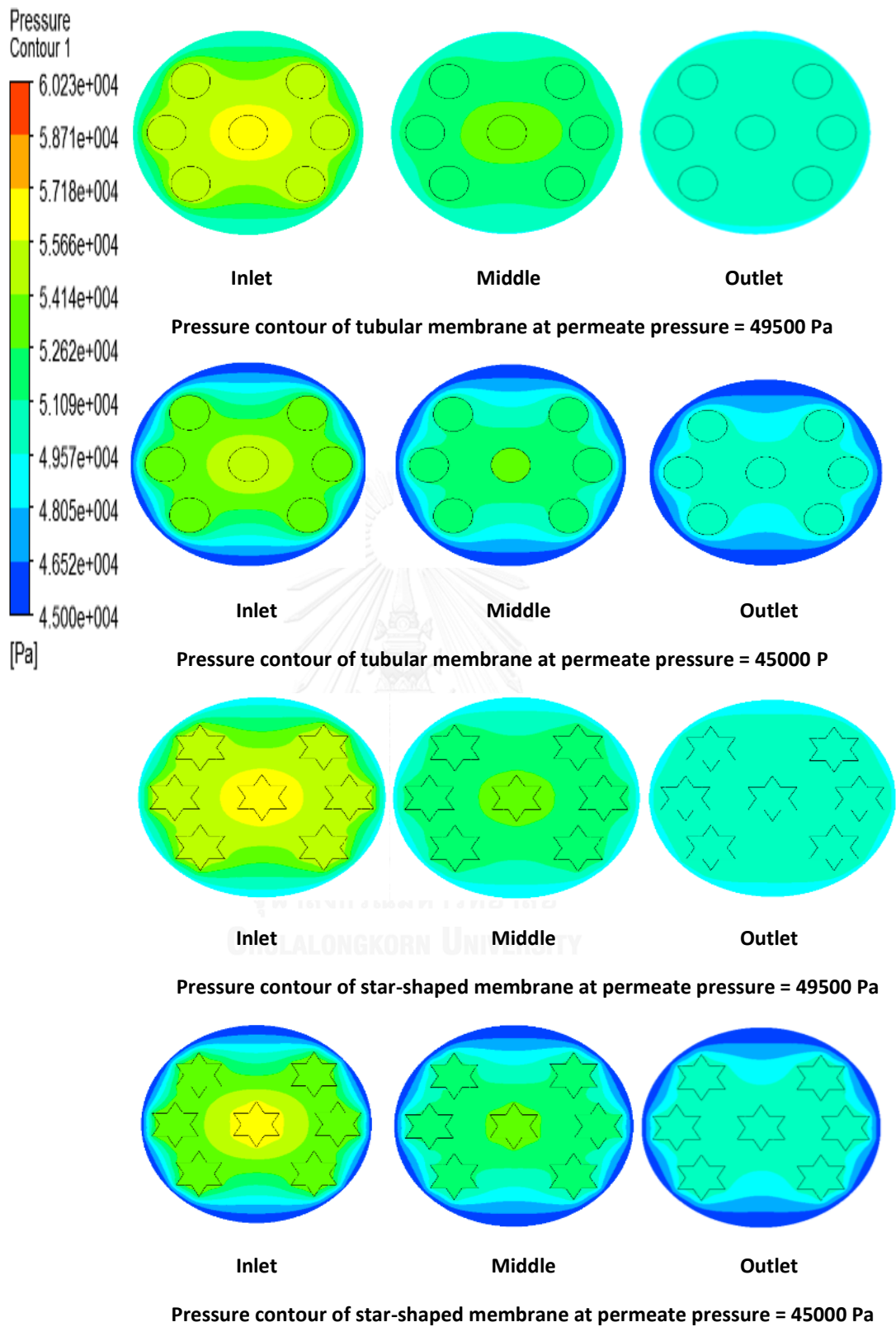
Figure 4.5 shows the velocity contour in tubular and star-shaped microfiltration membrane. From this figure, the velocity was decreased when operated at low permeate pressure (high trans-membrane pressure). Due to, operating at low permeate pressure effected to occur the gradient of pressure between flow channels and permeate side that forced the direction of fluid flowed into the permeate side. Therefore, the velocity in the flow channels was decreased. At permeate pressure of tubular membrane, star-shaped membrane, and star-shaped membrane with rod baffle was 45000 Pa, the maximum velocity occurred at the middle of tubular, star-shaped membrane, star-shaped membrane with rod baffle was 0.705 m/s, 0.695 m/s, and 0.635 m/s. Moreover, the velocity at the membrane surface of tubular, star-shaped membrane, and star-shaped membrane with rod baffle was 0.112 m/s, 0.125 m/s, and 0.141 m/s. Fluid velocity was gradually decreased when the fluid flowed near the membrane surface because the boundary at the membrane surface was non-slip.
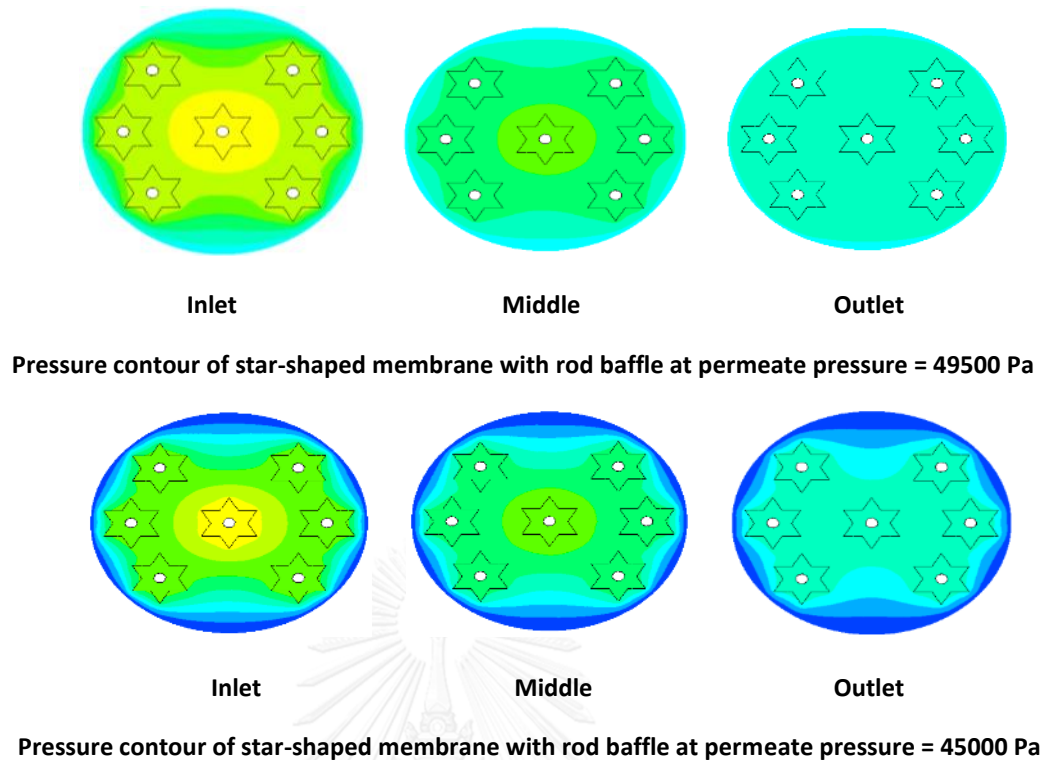
Velocity
Contour 1
7.056e-001
6.351e-001
5.645e-001
4.940e-001
4.234e-001
3.528e-001
2.823e-001
2.117e-001
1.411e-001
7.056e-002
0.000e+000
[m s^-1]

Inlet          Middle          Outlet

**Velocity contour of tubular membrane at permeate pressure = 49500 Pa**

Inlet          Middle          Outlet

**Velocity contour of tubular membrane at permeate pressure = 45000 Pa**

Inlet          Middle          Outlet

**Velocity contour of star-shaped membrane at permeate pressure = 49500 Pa**

Inlet          Middle          Outlet

**Velocity contour of star-shaped membrane at permeate pressure = 45000 Pa**

**Velocity contour of star-shaped membrane with rod baffle at permeate pressure = 49500 Pa**



**Velocity contour of star-shaped membrane with rod baffle at permeate pressure = 45000 Pa**

**Figure 4.5** Velocity contour of the star-shaped and the tubular microfiltration membrane at difference permeate pressure and with the same (inlet velocity = 0.5 m/s, outlet pressure, and particle property)

Figure 4.6 shows the effect of membrane geometry on the simulated contours of pressure along the membrane channel. From this figure, pressure gradient across the transverse plane and pressure drop along the channel were increased when operated at low permeate pressure (high trans-membrane pressure). At permeate pressure = 45000 Pa, star-shaped membrane with rod baffle has higher pressure gradient across the transverse plane near the entrance and higher pressure drop along the channel compared to tubular and star-shaped membrane. The stronger pressure gradient might be due to the minimum cross-sectional area of star-shaped microfiltration affecting the pressure loss due to the major loss in the system. Moreover, the higher pressure drop effected to use higher energy consumption (equation 2.17).
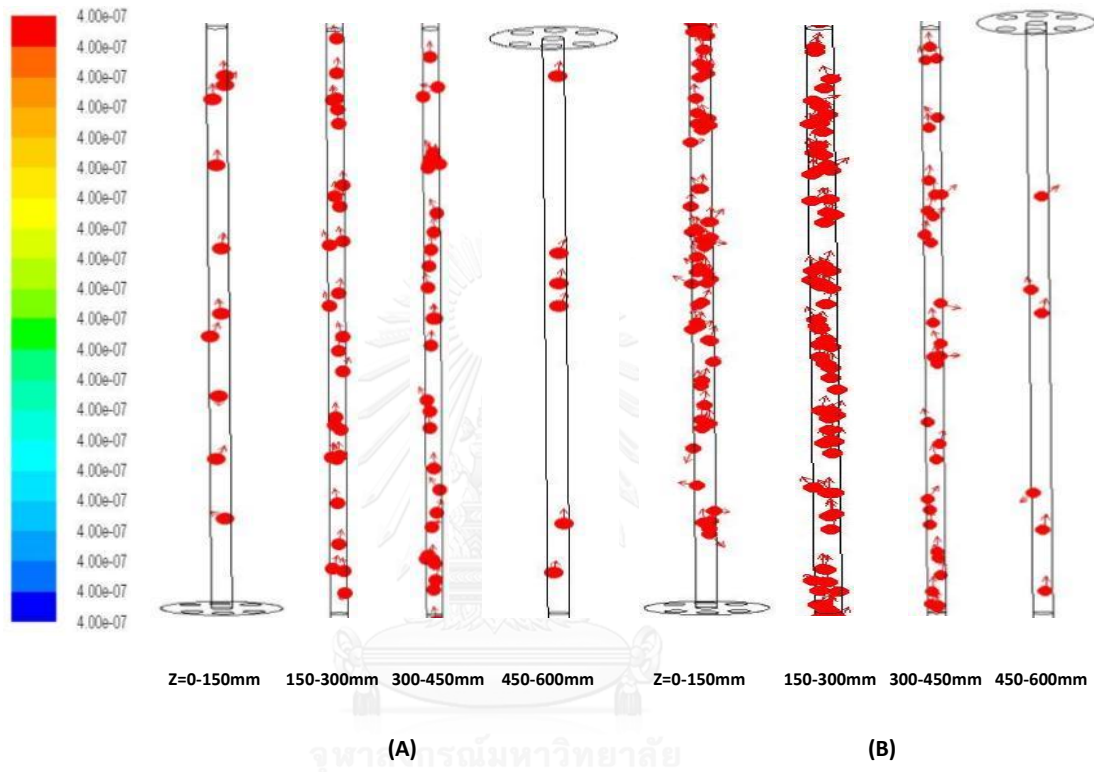
**Pressure contour of tubular membrane at permeate pressure = 49500 Pa**

**Pressure contour of tubular membrane at permeate pressure = 45000 P**

**Pressure contour of star-shaped membrane at permeate pressure = 49500 Pa**

**Pressure contour of star-shaped membrane at permeate pressure = 45000 Pa**

**Pressure contour of star-shaped membrane with rod baffle at permeate pressure = 49500 Pa**



**Pressure contour of star-shaped membrane with rod baffle at permeate pressure = 45000 Pa**

**Figure 4.6** Pressure contour of the star-shaped and the tubular microfiltration membrane at different permeate pressure at the same (inlet velocity = 0.5 m/s, outlet pressure, and particle property)

Figure 4.7 shows the particle distribution (at the same size 4x10-6m) in tubular, star-shaped, and star-shaped membrane with rod baffle (at time = 30 minutes). In addition, the arrows show the direction of particle motion. From this figure, the particle mass accumulation in the system was increased when operated at low permeate pressure (high trans-membrane pressure). Operating at low permeate pressure effected to occur the gradient of pressure between flow channels and permeate side. This pressure gradient forced the direction of fluid flowed toward the permeate side. Due to, the incidence of particle direction was based on flow stream of fluid. Accordingly, the most of particle direction flowed toward the permeate side (membrane surface side) which effected to particle deposition on membrane surface. Tubular membrane had the higher amount of particles accumulated in the system and the direction of particle flowed perpendicular to membrane surface (permeate side). In contrast, star-shaped membrane with rod baffle had the lower amount of particles accumulated in the system. Moreover, the direction of particle in star-shaped membrane with rod baffle flowed toward outlet (retentate side) more than tubular and star-shaped membrane. The particle deposition was explained by velocity profile of waste water. Although, the velocity profile at the middle of tubular channel was higher than the velocity profile at the middle of star-shaped channel but there still lack the high velocity at the membrane surface. While, star-shaped membrane with rod
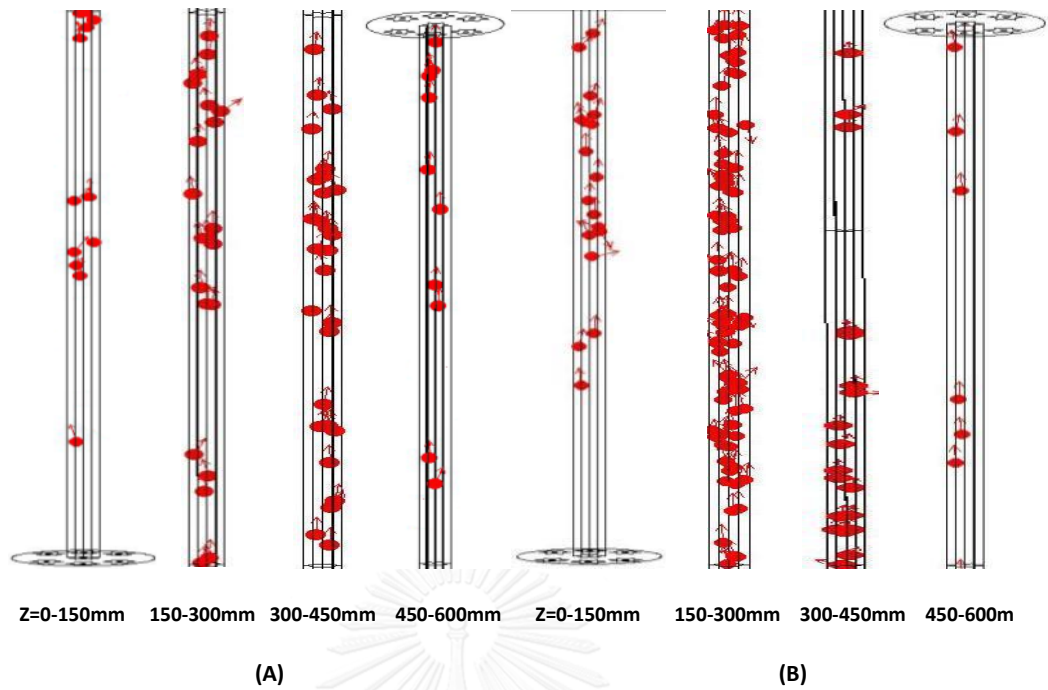
baffle had a higher velocity at the membrane surface than tubular membrane. Under this condition (i.e., lower velocity near surface) explained the particles did not have sufficient shear force (equation 2.12) to induce the lifting for the particle to migrate out of the membrane surface. Therefore, particles were deposited on the membrane surface that effected to decrease the flux for the tubular channel.
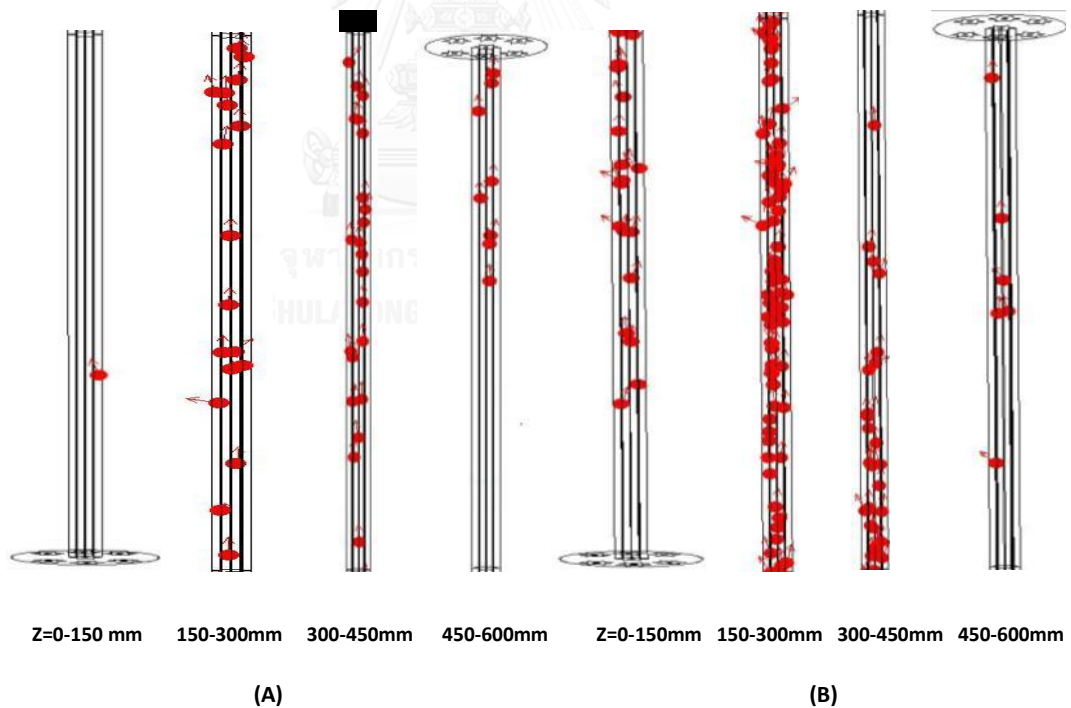


Particle mass profile in tubular microfiltration A) permeate pressure = 49500 Pa, B) permeate pressure =4500Pa

**Particle mass profile in star-shaped microfiltration A) Permeate pressure = 49500 Pa, B) Permeate pressure =45000Pa**



**Particle mass profile in star-shaped microfiltration with rod baffle A) Permeate pressure = 49500 Pa, B) Permeate pressure =45000Pa**

**Figure 4.7** Particle mass distribution profile over different ranges (z) along the star-shaped and the tubular microfiltration membrane at the same (inlet velocity = 0.5 m/s, outlet pressure, and particle size)

## 4.4 The Comparison of particle distribution at different inlet flow channel between middle flow channel with beside flow channel

Figure 4.8-4.9 shows the particle distribution (at the same size $4 \times 10^{-6}$m) in tubular membrane (at time = 30 minutes). In addition, the arrows show the direction of particle motion. From this figure, the particle mass distribution of middle flow channel and beside flow channel had the same particle direction. Because the distance of middle flow channel and beside flow channel to permeate side had a little difference distance form permeate side. Therefore a little difference of distance was not effect to pressure gradient which effected to particle distribution in flow channel. Therefore, only the middle flow was a representative to explain the particle distribution in other flow channel.



Particle Traces Colored by Particle Diameter (m) (Time=1.8000e+03)

Z=0-150 mm    150-300mm    300-450mm    450-600mm        Z=0-150mm    150-300mm    300-450mm    450-600mm

(A)                                                                    (B)
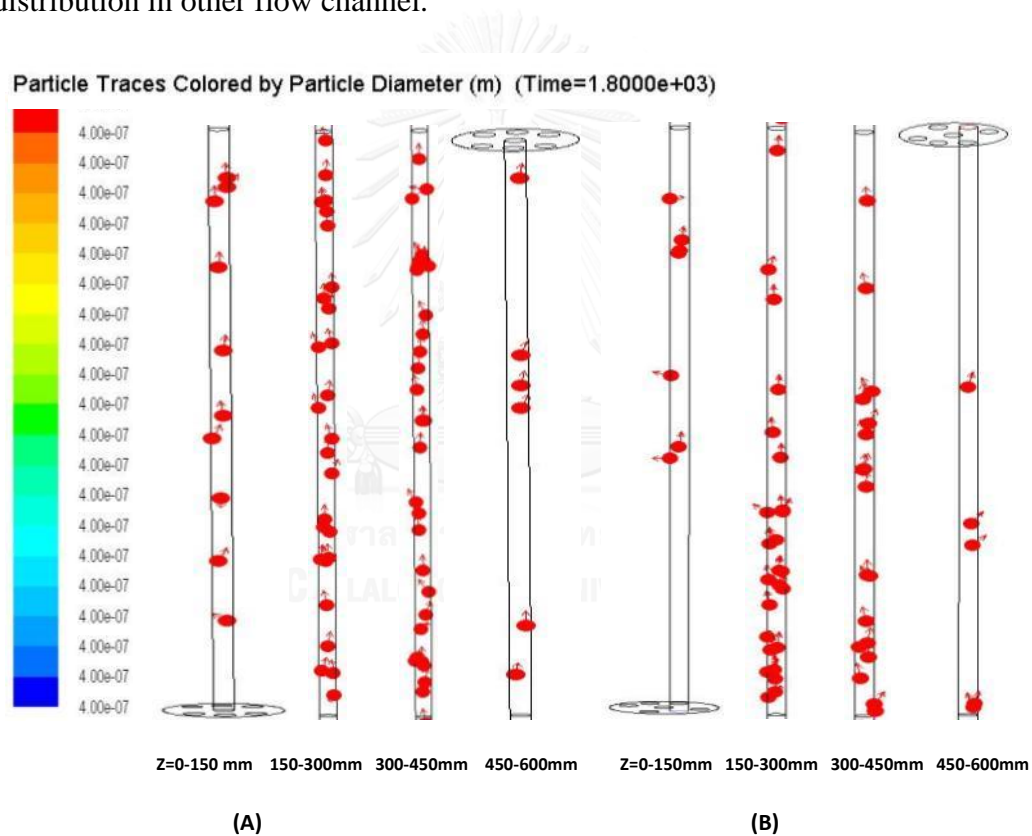
Particle mass profile in tubular microfiltration at permeate pressure = 49500 Pa A) middle flow channel, B) beside flow channel

**Figure 4.8** Particle mass distribution profile over different ranges (z) along the tubular microfiltration membrane at different inlet flow channel with the same (inlet velocity = 0.5 m/s, outlet pressure, and particle size)

Z=0-150 mm    150-300mm    300-450mm    450-600mm          Z=0-150mm    150-300mm    300-450mm    450-600mm

(A)                                                          (B)
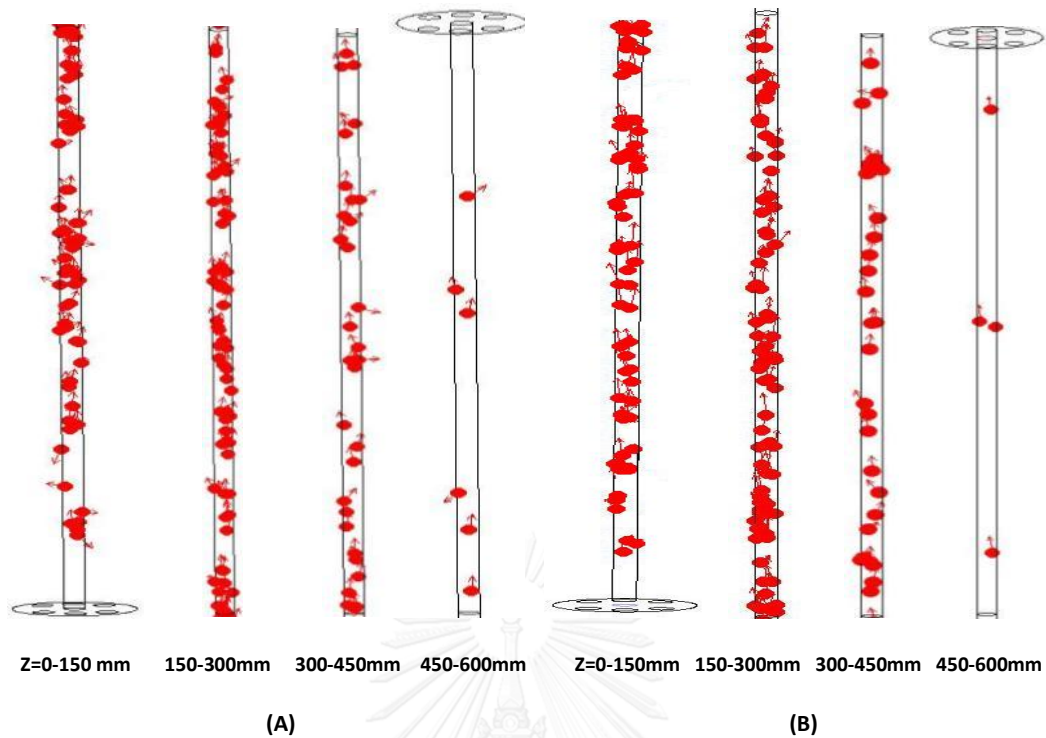
**Particle mass profile in tubular microfiltration at permeate pressure = 45000 Pa A) middle flow channel, B) beside flow channel**

**Figure 4.9** Particle mass distribution profile over different ranges (z) along tubular microfiltration membrane at different inlet flow channel with the same (inlet velocity = 0.5 m/s, outlet pressure, and particle property)

## 4.5 Model validation of star-shaped microfiltration membrane with rod baffle

The comparison of the critical flux from the simulation and the experimental data reported by Gésan-Guiziou et al (2001) has shown that the CFD model can effectively predict the flow and particle deposition behaviors in the tubular membrane microfiltration system. However, from the comparison of the performance of star-shaped membrane with rod baffle, star-shaped membrane, and tubular membrane at the same condition, it was shown that star-shaped membrane with rod baffle offered a higher critical flux than the others [3]. Therefore, further study will focus on star-shaped membrane with rod baffle. In addition, the CFD model, validated based on the tubular membrane module, was taken to predict the flow and particle deposition behaviors in star-shaped membrane with rod baffle in the work of Chui et al (2005). The validation result of the CFD model with the experimental data by Chui et al (2005) is shown in Figure 4.8. Note that the boundary condition, operating condition, and the type of geometry of membrane of star-shaped membrane by Chui et al (2005) resembled to tubular membrane by Gésan-Guiziou et al (2001).

CFD simulation results were compared with the experiment results of the critical flux. The RNG k-ε turbulence model (Equation (2.4, 2.5)) and the discrete phase model (Equation (2.13, 2.14)) have been used to simulate momentum transport and particle distribution which affected the critical flux of the system. Figure 4.10 shows the comparison of the critical flux from the experiments and the simulations results. The percent deviation of the experiment and simulation result was 13 percent because this system had the seven type of particle and the assumption of inter-particle interaction in simulation work was negligible. While, inter-particle interaction in experiment may be occur in the system. Thus, the inter-particle interaction effected to particle collision which effected to the particle deposition. Therefore, the critical flux from simulation was deviated from experiment.
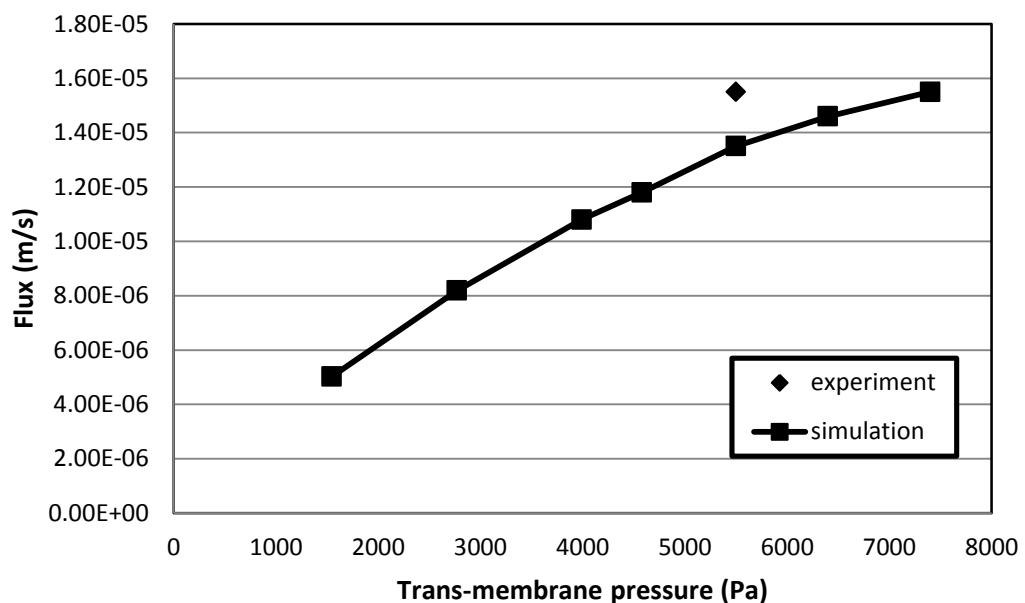


**Figure 4.10** Comparison of the critical flux from the simulation and the experimental measurement (Chui et al 2005) in star-shaped microfiltration membrane with rod baffle at (inlet velocity = 3.27 m/s)

## 4.6 Parametric study

The parametric study was carried out to determine the effected operating parameter to critical flux. The operating conditions, for example: the effect of velocity inlet, particle size and coefficient restitution, were changed. The results based on the critical flux were obtained.

### 4.6.1 Effect of inlet velocity

Figure 4.11 shows the effect of inlet velocity of waste water in the star-shaped microfiltration membrane on the critical flux. The different inlet velocity, i.e., (2.50 m/s, 3.27 m/s, and 4.00 m/s) was compared. The result shows that when velocity inlet was increased, the fouling resistance was decreased (Figure 4.12). As a result, higher critical flux was founded when operated at high inlet velocity. At high inlet velocity had high viscous drag force. The force exerts on the particle and does not allow it to settle on membrane surface. Moreover, at high velocity the resident time of particle is low. Then, the particle has a less time to settle down on membrane surface. Therefore, the critical flux will increase.
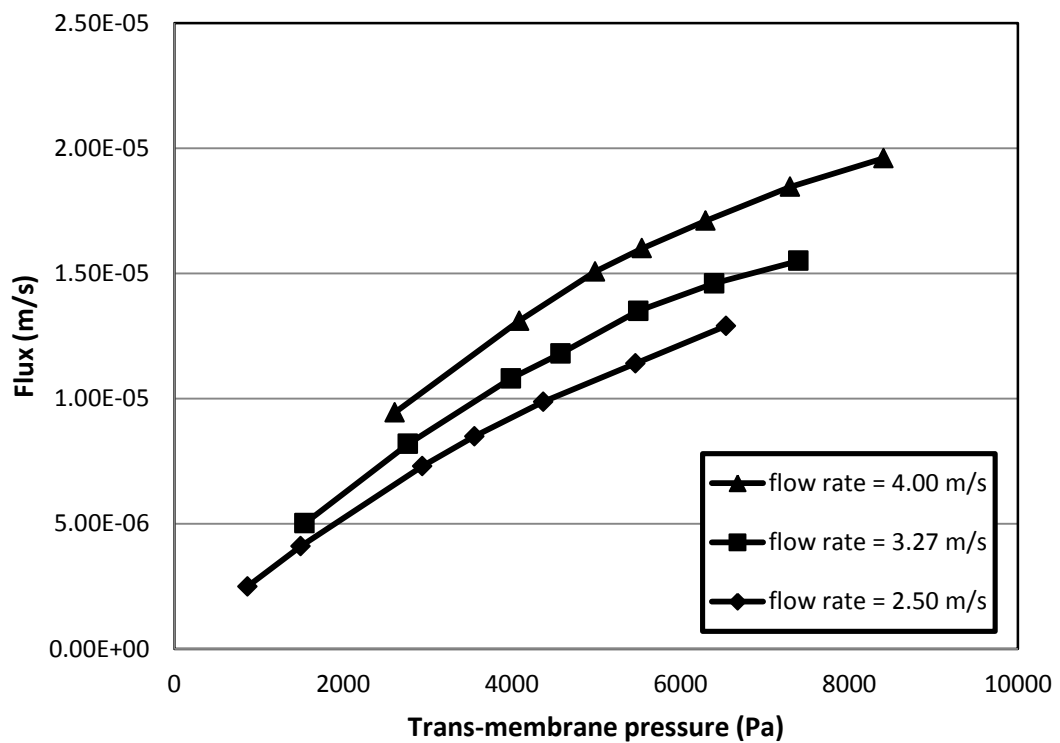


**Figure 4.11** Comparison of the effect of inlet velocity to critical flux in star-shaped microfiltration membrane with rod baffle at different inlet velocity with the same (outlet pressure, permeate pressure, and particle property)
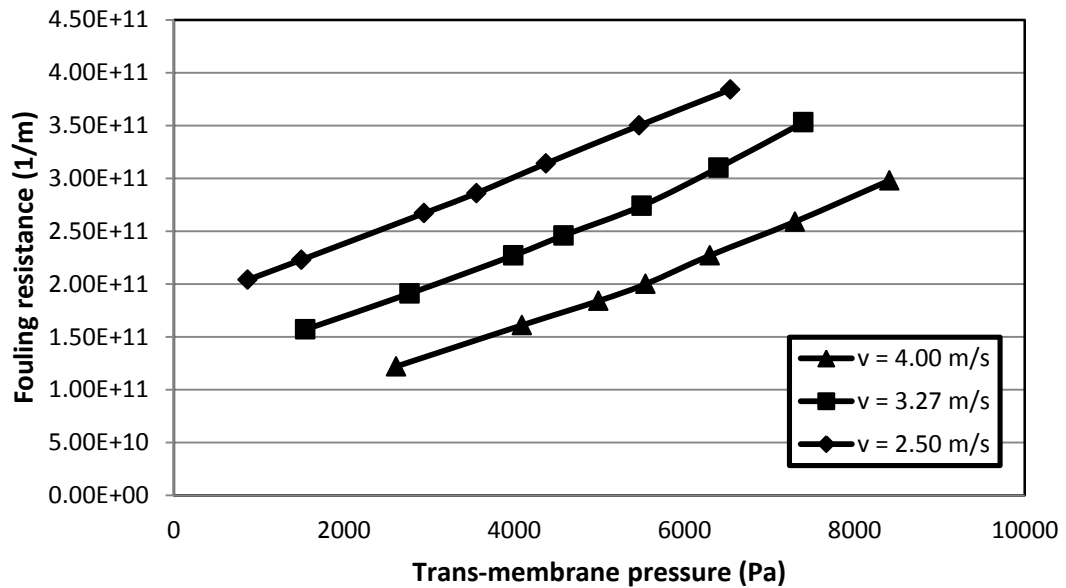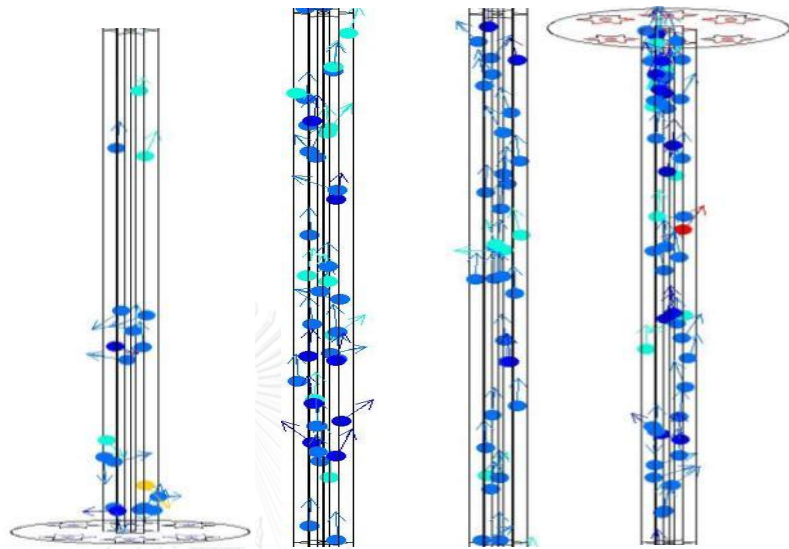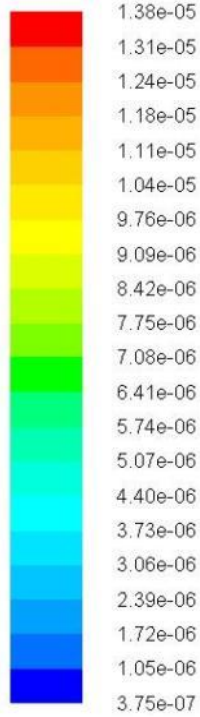
**Figure 4.12** Comparison of the effect of inlet velocity to fouling resistance in star-shaped microfiltration membrane with rod baffle at different velocity with the same (outlet pressure, permeate pressure, and particle property)

Figure 4.13 shows the particle velocity profile at different inlet velocity, i.e., (2.50 m/s, 3.27 m/s, and 4.00 m/s). The lowest particle velocity happened at 2.50 m/s and the highest at 4.0 m/s. At the lowest velocity inlet had the lowest particle velocity and particle direction flowed perpendicular to membrane surface. However, at the highest inlet velocity had the highest particle velocity and particles direction flowed more parallel to membrane surface. The particle distribution was be explained by drag force. Hwang et al (2001) [24] studied the effect of flow rate to particle distribution. The result showed that at higher volumetric flow rate, the particle had a higher viscous drag force for preventing particle to accumulate on membrane surface (equation 2.6). Therefore, this can explain that the high inlet velocity (4.00 m/s) had a highest viscous drag force to migrate the particles which did not allow particles to settle down on the membrane surface. Therefore, operating at inlet velocity (4.00 m/s) had the highest flux. Moreover, Jirathanon et al (1995) [18] studied the effect of volumetric flow rate of fruit juice to the concentration polarization on membrane surface. They explained that high velocity had a high sheer force that wash the concentration of fouling on membrane surface and helped to increase flux.

Particle Traces Colored by Particle Velocity Magnitude (m/s)  (Time=1.8000e+03)



| | | | |
|---|---|---|---|
| Z= 0-75 mm | Z= 75-150 mm | Z= 150-225 mm | Z= 225-300 mm |

**Inlet velocity = 2.50m/s**



| | | | |
|---|---|---|---|
| Z= 0-75 mm | Z= 75-150 mm | Z= 150-225 mm | Z= 225-300 mm |

**Inlet velocity = 3.27 m/s**

**Z= 0-75 mm**    **Z= 75-150 mm**    **Z= 150-225 mm**    **Z= 225-300 mm**

**Inlet velocity = 4.00 m/s**
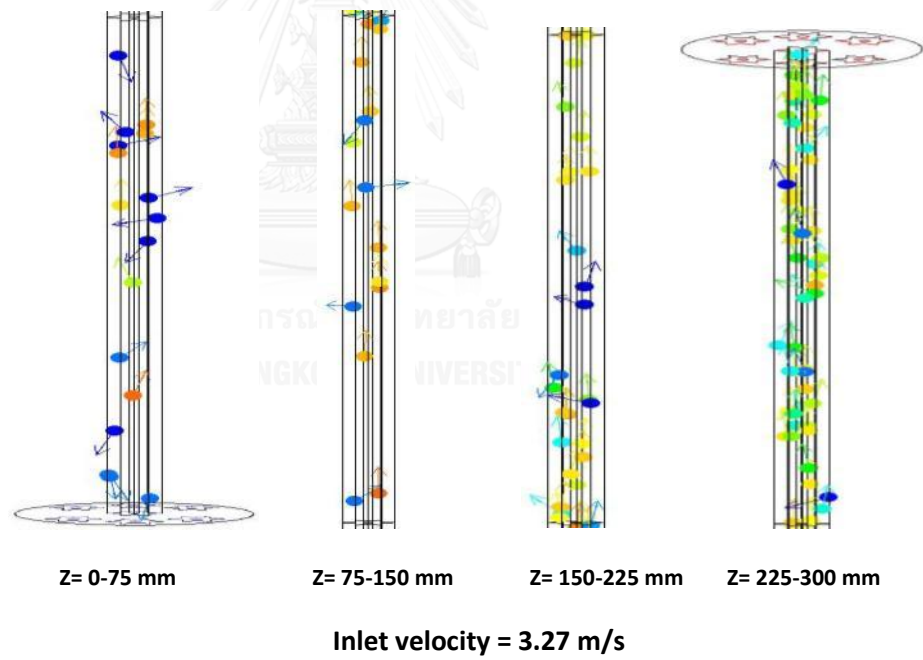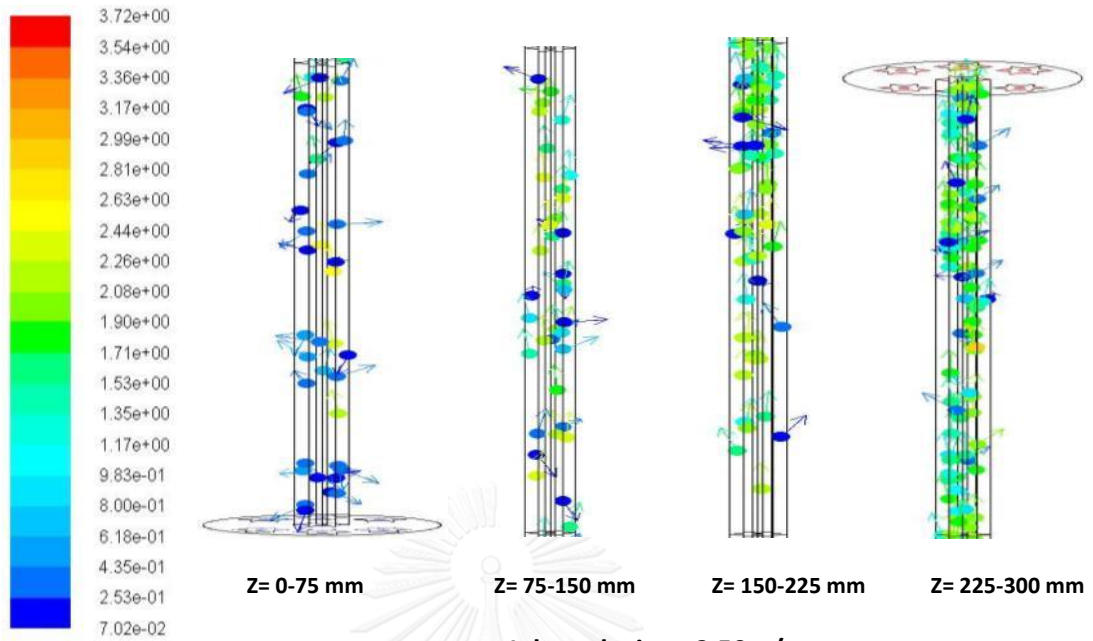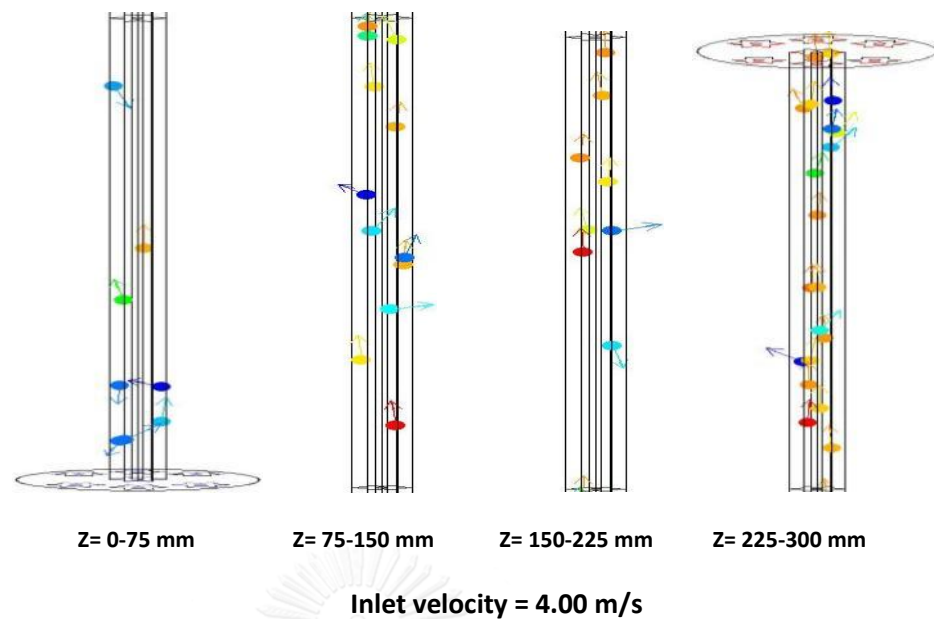
**Figure 4.13** Particle velocity profile for the star-shaped microfiltration membrane at different inlet velocity with the same (outlet pressure, permeate pressure, and particle property)

### 4.6.2 Effect of particle size

Figure 4.14 shows the effect of particle size to critical flux in the star-shaped microfiltration membrane. The different particle size of meat extraction, i.e., (small = $3.75 \times 10^{-7}$ m, medium = $1.5 \times 10^{-6}$ m, and large = $5 \times 10^{-6}$ m) was compared. The result shows that when particle size was increased, the fouling resistance was decreased (Figure 4.15). As a result, higher critical flux was founded when operated at large particle size. Because the fluid phase hardly influenced to large size of particle while, a small size of particle was easily to interact with fluid phase. Therefore, it was easily to force small size of particle to deposit on membrane surface than large size of particle.
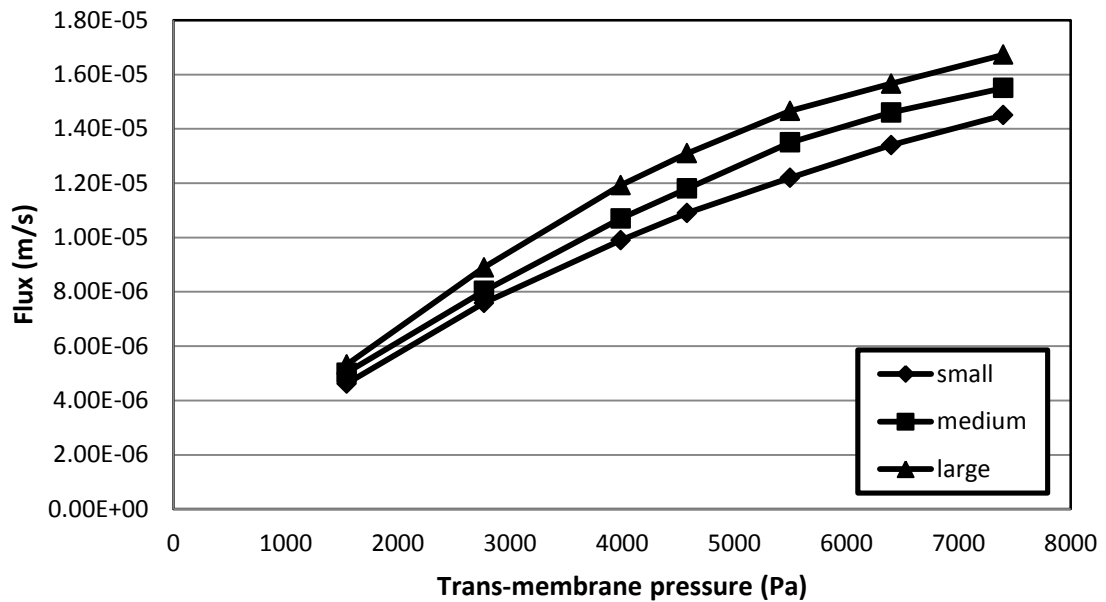
**Figure 4.14** Comparison of the effect of particle size to critical flux in star-shaped microfiltration membrane with rod baffle at the same (outlet and permeate pressure, and inlet velocity)
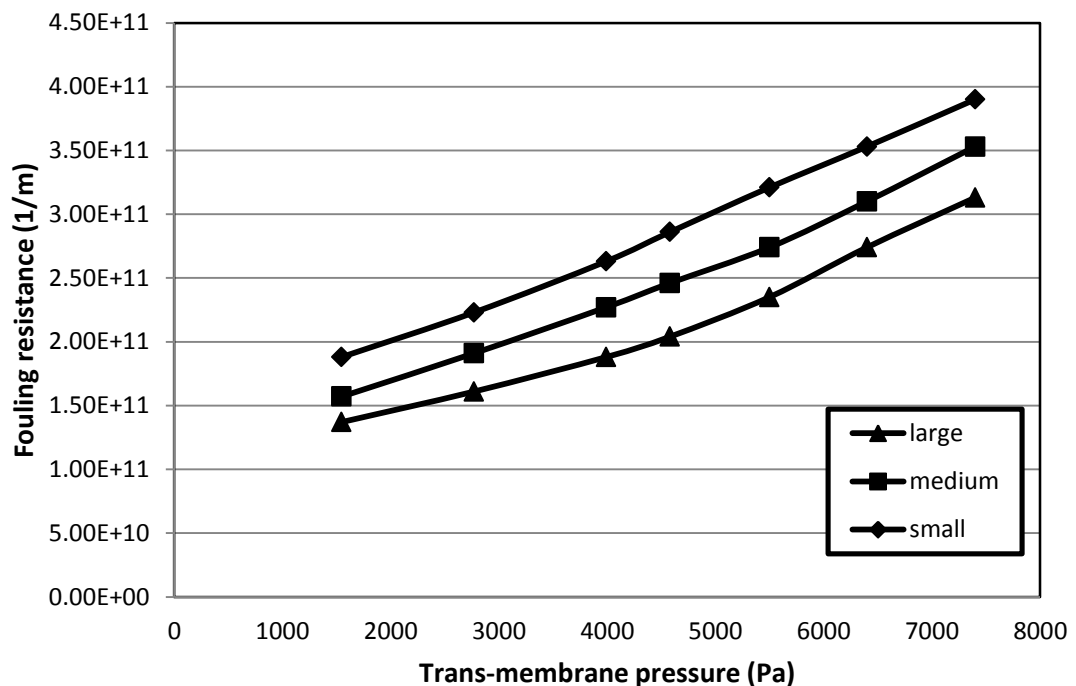


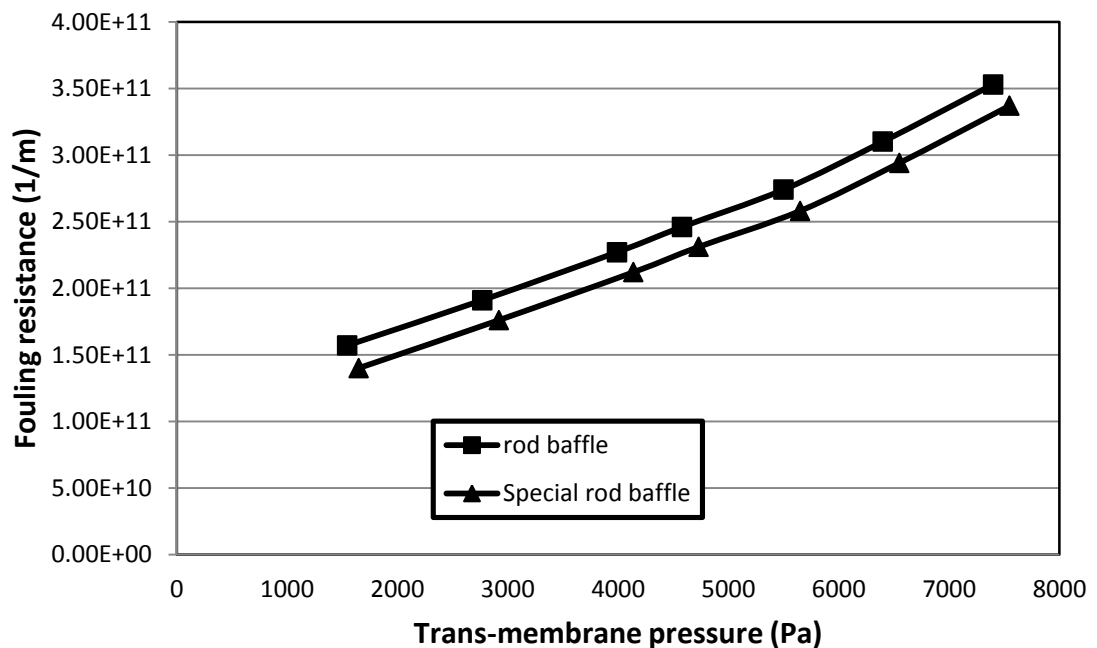**Figure 4.15** Comparison of the effect of particle size on fouling resistance in star-shaped microfiltration membrane with rod baffle at different particle size with the same (outlet pressure, permeate pressure and inlet velocity)

Figure 4.16 shows the particle size distribution profile of seven type of substances at different particle size injection of meat extraction, i.e., (small = $3.75 \times 10^{-7}$ m, medium = $1.5 \times 10^{-6}$ m, and large = $5 \times 10^{-6}$ m) by fixing to equal mass flow rate of all size of meat extraction injection. The highest amount of particles remained in the system happened at small size and the lowest at large size. The small particle size had the highest amount of particle remained in the system and the particles direction flowed perpendicular to membrane surface. However, the large particle size had the lowest amount of particle remained in the system and particles direction flowed more parallel to membrane surface. For each system the small particles were found more at the entrance region, while the large particles were found more at the exit region (retentate). Therefore, this can explain that small particle had a chance to settle down at the entrance, while the large particle had a chance to settle down at the exit.

The particle size distribution was explained by the balancing of drag force and lift force. Hwang et al (2010) [24] studied the effected of binary particles size to particle deposition. The result shows that small particles were compacted at the membrane surface more than large particle although large particle had higher a drag force than small size but it had a higher lift force than small size too  simulation. The lift force, which did not allow particles to settle down to the membrane, overcame drag force caused there were many small particles near the membrane surface. Altmann et al (1996) [25] studied the particle deposition and layer formation at cross flow microfiltration membrane. The result showed that the large size of particle had a higher lift force, so it did not settle down to the membrane surface. However, only small particle size could be deposited on the membrane surface. Moreover, Van dinther [26] studied the effect of flow to particle migration in micro channel. The result showed that large particle migrated to the middle of channel while small particle had a higher amount near the membrane surface. They elucidated the particle migration was caused by shear induce diffusion that particle diameter and shear rate were the function of it. The conclusion of particle deposition of Dinther et al (2013)and Altmann et al (1996) had the same tenor. Therefore, this can explain the large size of particles had a highest lift force and sheer induce diffusion (shear-induced diffusion) to help particles migrate away and not settle down on the membrane surface. Therefore, operating at large size had the higher flux.

Particle Traces Colored by Particle Diameter (m)  (Time=1.8000e+03)



**Z= 0-75 mm      Z= 75-150 mm   Z= 150-225 mm   Z= 225-300 mm**

**Small size of particle**
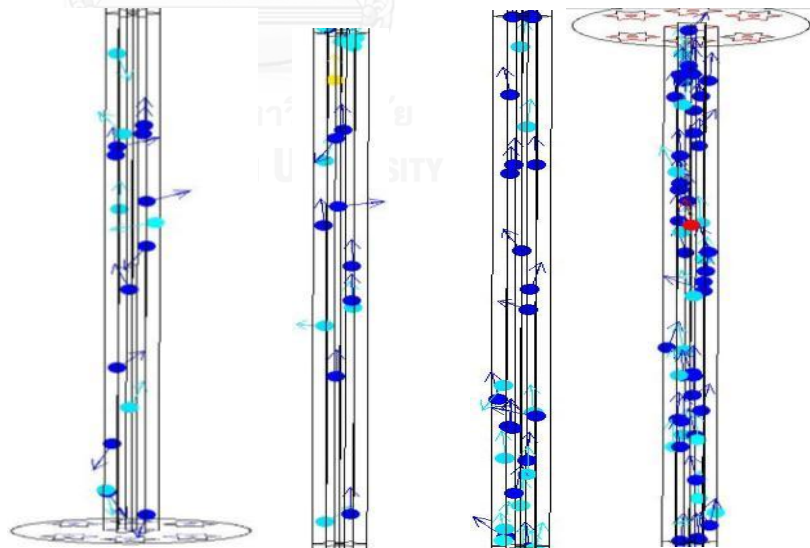
**Z= 0-75 mm      Z= 75-150 mm   Z= 150-225 mm   Z= 225-300 mm**

**Medium size of particle**

**Z= 0-75 mm    Z= 75-150 mm    Z= 150-225 mm  Z= 225-300 mm**

**Large size of particle**
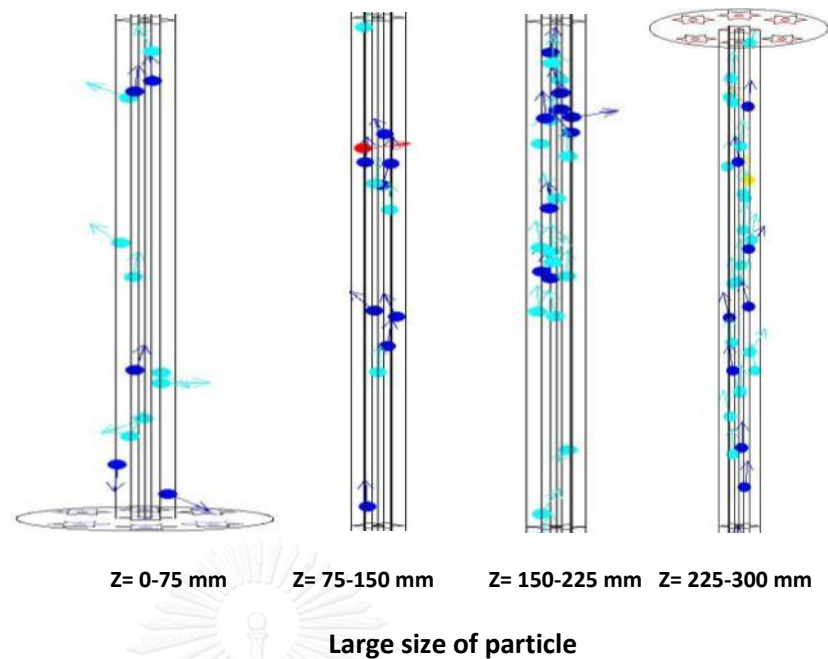
**Figure 4.16** Particle size distribution profile of the star-shaped microfiltration membrane with rod baffle at different particle size with the same (outlet pressure, permeate pressure, and inlet velocity)

### 4.6.3 Effect of coefficient restitution

Coefficient of restitution was the particle collision on rod baffle. The rebound of particle on rod baffle was investigated to the effected to critical flux. Figure 4.17 shows of the effect of coefficient restitution of particle on rod baffle in the star-shaped microfiltration membrane on the critical flux. The different coefficient restitution of baffle, i.e., (1, 0.5, and 0.1) was compared. The result shows that when coefficient restitution of baffle was decreased, the fouling resistance was only slightly increased (Figure 4.18). As a result, critical flux was not changed when operated at different coefficient restitution. This might be due to the direction of rod baffle which was installed parallel to the fluid flow direction at the middle of star-shaped microfiltration channel. However, the operation step of microfiltration membrane was decreased permeate pressure (increased trans-membrane pressure) for increasing the critical flux. Thus, the direction of fluid would be flowed into the membrane surface which was the same side of permeate pressure. Due to, the incidence of particle direction was based on flow stream of fluid. Accordingly, the most of particle direction flowed into the permeate side which did not impacted to rod baffle. This was a reason that the coefficient of restitution in this work did not effect to the critical flux. Moreover, the boundary of membrane was set up to interface zone boundary which could not adjust the coefficient of restitution. Therefore, it was a reason that made the simulation results deviated to experiment result.
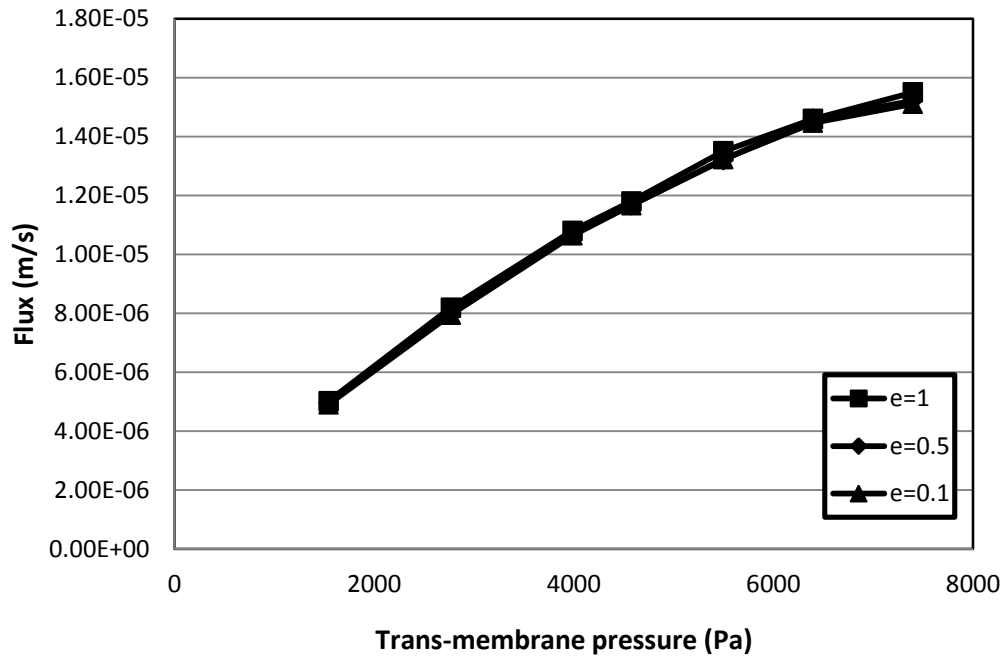
**Figure 4.17** Comparison of the effect of coefficient of restitution to critical flux in star-shaped microfiltration membrane with rod baffle at the same (outlet pressure, permeate pressure, inlet velocity = 3.27 m/s, and at particle property)
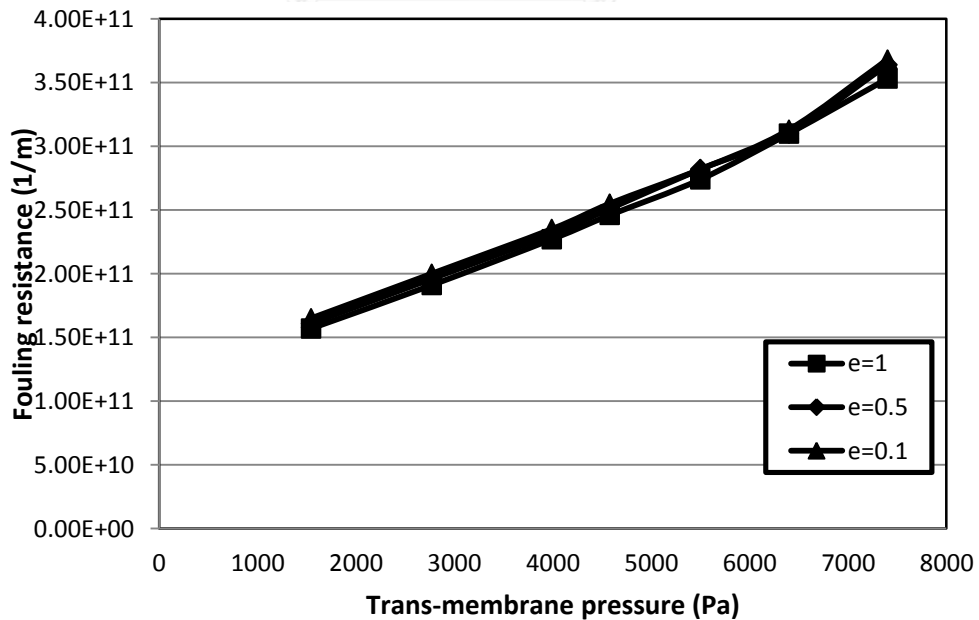


**Figure 4.18** Comparison of the effect of coefficient of restitution to fouling resistance in star-shaped microfiltration membrane with rod baffle at the same (outlet pressure, permeate pressure, inlet velocity = 3.27 m/s, and at particle property)

## 4.7 Baffle guideline

Figure 4.19 shows the effect of baffle type in the star-shaped microfiltration membrane on the critical flux. The different of baffle type, i.e., (rod, and special rod) was compared. The result shows that when special rod was inserted into the star-shaped microfiltration, the fouling resistance was decreased (Figure 4.20). As a result, higher critical flux was founded when inserted special baffle into the star-shaped microfiltration. Because near the membrane surface which velocity of special rod baffle had higher than rod baffle that velocity could prevent the accumulation of particle on membrane surface which influence to increase filtration flux.
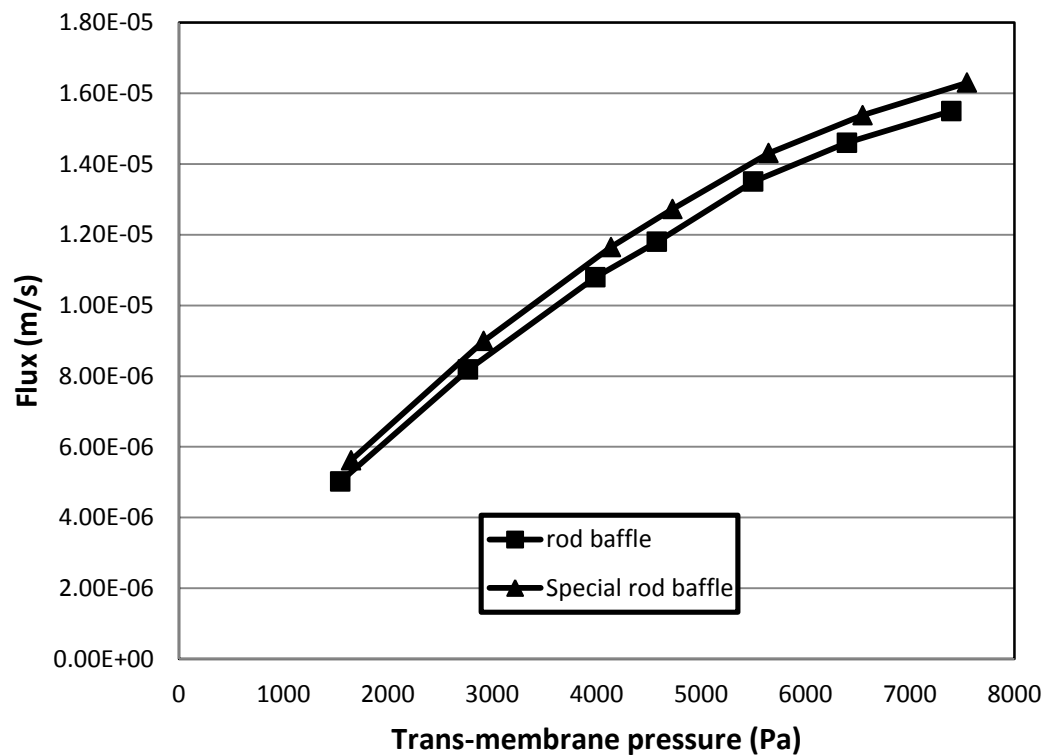


**Figure 4.19** Comparison of the effect of baffle type to critical flux in star-shaped microfiltration membrane with baffle at the same (velocity = 3.27 m/s, permeate pressure, outlet pressure, and at particle property)

**Figure 4.20** Comparison of the effect of baffle type to fouling resistance in star-shaped microfiltration membrane with baffle at the same (outlet pressure, permeate pressure, inlet velocity = 3.27 m/s, and at particle property)

Figure 4.21 shows the velocity profile at different baffle type, i.e., (rod baffle, and special rod baffle). At distance of z =150-225mm and z = 225-300 of the region of special rod was inserted into star-shaped microfiltration membrane. This region offered a high velocity near membrane surface. Thus, at high velocity could prevent the accumulation of particle on membrane surface which influence to increase filtration flux. Figure 4.22 shows the particle velocity profile at different baffle type. The particle in the area of z =150-225 mm and z = 225-300mm which did not insert special rod baffle had a lower particle velocity than special rod baffle. Moreover, the vector of particle in rod baffle flowed into the membrane surface more than special rod baffle. Ahmed et al (2011) [23] studied the effect of baffle in tubular membrane channel. The rod baffle influenced the wall shear stress which reduced particles accumulation on the membrane surface. Therefore, special rod offered a higher flux.
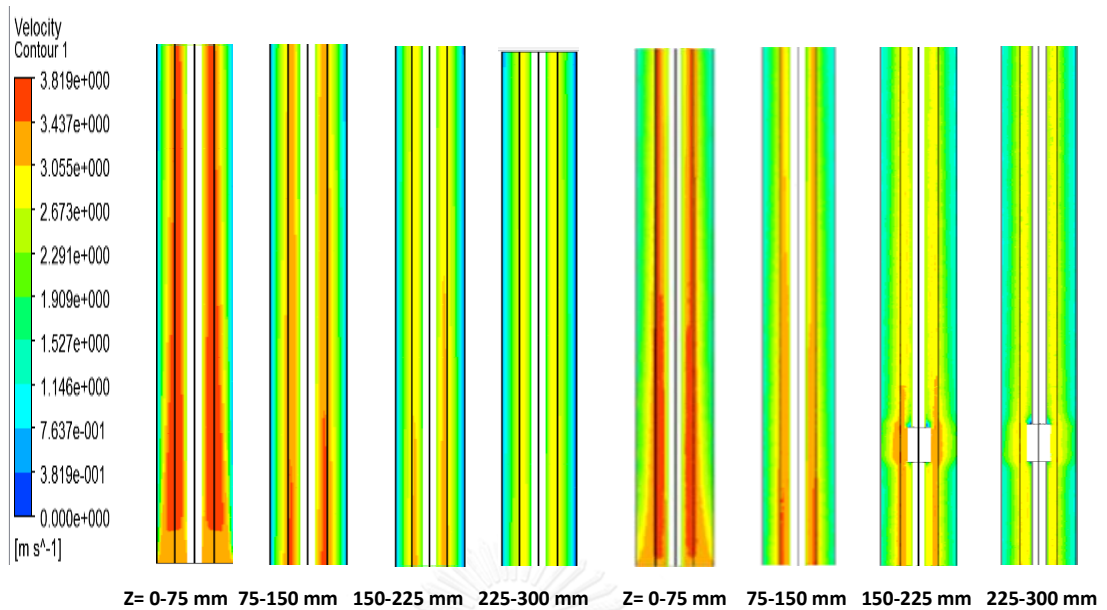
**Figure 4.21** Velocity profile in star-shaped microfiltration membrane. A) insert rod baffle B) insert special rod baffle at the same (inlet velocity, permeate pressure, outlet pressure, and particle property)
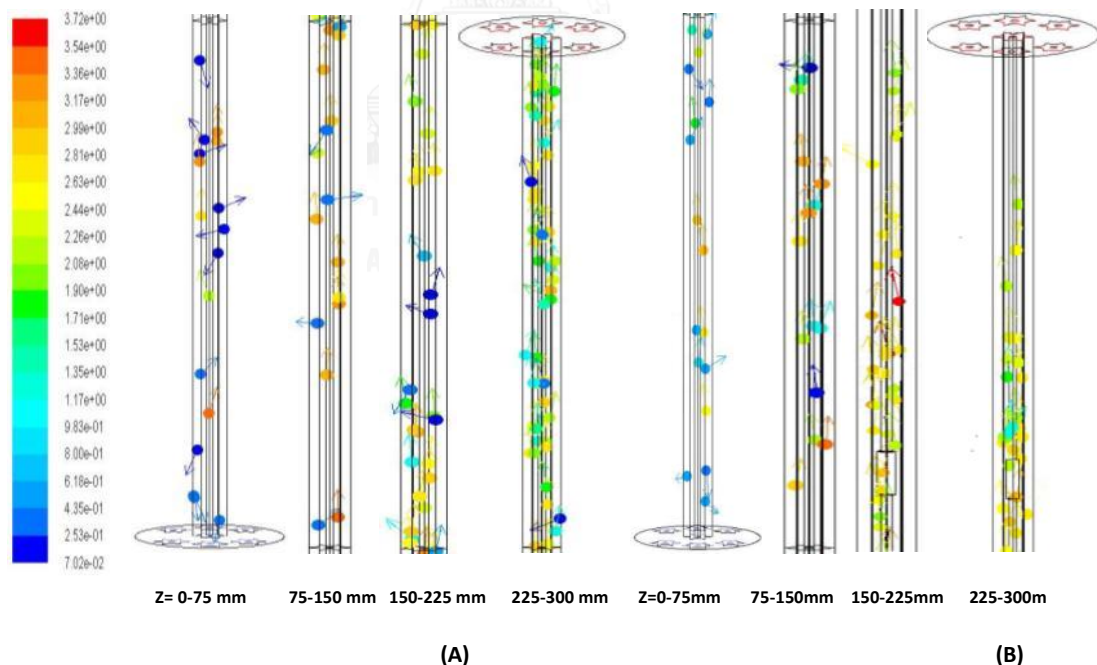


**Figure 4.22** Particle velocity profile in star-shaped microfiltration membrane. A) insert rod baffle B) insert special rod baffle at the same (inlet velocity, permeate pressure, outlet pressure, and particle property)

**4.8 Energy consumption**

The energy consumption or the energy required for the pump in order to achieve a specific flux value. Table 4.1 shows the energy consumption in the star-shaped microfiltration membrane at different inlet velocity, i.e., (v=2.5m/s, v=3.27m/s, and v=4.0m/s). Increase inlet velocity lead to increase pressure drop that effected to increase energy consumption (equation 2.17). Although, at inlet velocity was 4.0 m/s which purposed the highest critical flux but it used the highest energy of pump. Thus, at 4.0 m/s was not worthwhile for operation. Therefore, at 2.5m/s of inlet velocity was suitable for operating.

**Table 4.1** Energy consumption of star-shaped membrane with rod baffle (at different inlet velocity)

| Inlet velocity | Critical flux (m/s) | Energy consumption ($J/m^3$) |
|---|---|---|
| V = 2.5 m/s | $9.87 \times 10^{-6}$ | $1.84 \times 10^{-5}$ |
| V = 3.27 m/s | $1.35 \times 10^{-5}$ | $2.22 \times 10^{-5}$ |
| V=4.00m/s | $1.96 \times 10^{-5}$ | $2.45 \times 10^{-5}$ |

Table 4.2 shows the energy consumption in the star-shaped microfiltration membrane at different particle size, i.e., (small, medium, and large). Increase particle size lead to increase critical flux and decrease energy consumption (equation 2.17). Because increasing particle size, not only the pressure drop was not increased but also the critical flux was increased. Therefore, at large size of particle offered high performance.

**Table 4.2** Energy consumption of star-shaped membrane with rod baffle (at different particle size)

| Particle size | Critical flux | Energy consumption ($J/m^3$) |
|---|---|---|
| Small size | $1.22 \times 10^{-5}$ | $2.46 \times 10^{-5}$ |
| Medium size | $1.35 \times 10^{-5}$ | $2.22 \times 10^{-5}$ |
| Large size | $1.47 \times 10^{-5}$ | $2.04 \times 10^{-5}$ |

Table 4.3 shows the energy consumption in the star-shaped microfiltration membrane at different coefficient of restitution, i.e., (e=0.1, e=0.5, and e=1.0). Increase coefficient of restitution lead to decrease energy consumption (equation 2.17). Because increasing coefficient of restitution, not only the pressure drop was not

increased but also the critical flux was increased. Therefore, e=1 of coefficient of restitution offer high performance.

**Table 4.3** Energy consumption of star-shaped membrane with rod baffle (at different coefficient of restitution)

| Coefficient of restitution | Critical flux | Energy consumption $(J/m^3)$ |
|---|---|---|
| e=0.1 | $1.32 \times 10^{-5}$ | $2.27 \times 10^{-5}$ |
| e=0.5 | $1.32 \times 10^{-5}$ | $2.27 \times 10^{-5}$ |
| e=1.0 | $1.35 \times 10^{-5}$ | $2.22 \times 10^{-5}$ |

Table 4.4 shows the energy consumption in the star-shaped microfiltration membrane at different baffle type, i.e., (rod baffle, and special rod baffle). Increase coefficient of restitution lead to decrease energy consumption (equation 2.17). Although, inserting special rod baffle into star-shaped membrane was increased the pressure drop but they purposed the higher critical flux and used less energy consumption than rod baffle. Therefore, special rod of baffle was suitable for choosing.

**Table 4.4** Energy consumption of star-shaped membrane with baffle (at different baffle type)

| Baffle type | Critical flux | Energy consumption $(J/m^3)$ |
|---|---|---|
| Rod baffle | $1.35 \times 10^{-5}$ | $2.22 \times 10^{-5}$ |
| Special Baffle | $1.43 \times 10^{-5}$ | $2.15 \times 10^{-5}$ |

# CHAPTER5

# CONCLUSIONS AND RECOMMENDATION

**Conclusions**

This study was aimed to explain the transport phenomena of fluid and particles fouling inside the tubular and star-shaped microfiltration membrane. In addition, the effects of inlet velocity, particle size, coefficient of restitute, and baffle geometry on the critical flux were also investigated in order to develop a guideline for optimal operation of the microfiltration membrane. The conclusions of this study are:

- The fluid flow inside tubular and star-shaped microfiltration membrane can be simulated using a Computational Fluid Dynamics (CFD) modeling. It was found that RNG k-ε turbulent model and discrete phase model could effectively predict the fluid flow and the particle motion, respectively.

- The inlet velocity has significant to the critical flux. It was found that increasing the inlet velocity of water tends to decrease fouling of the system because the particle has higher viscous drag force in parallel direction with membrane surface. The force exerts on the particle and does not allow it to settle on membrane surface. Moreover, at high velocity the resident time of particle is low. Then, the particle has a less time to settle down on membrane surface. Therefore, the critical flux will increase.

- The particle size has a significant to the critical flux. When increasing the particle size, fouling tends to decrease. This is because large particle has higher shear force which relates to lift force for lifting the particle and not allowing it to settle down on the membrane surface. Then, the critical flux will increase.

- The coefficient of restitute has not significant to the critical flux because the which flows into the permeate side and retentate side that the chance of particle

- The special geometry has a significant to the critical flux. Inserting the special geometry tends to decrease fouling because the geometry

increases the fluid velocity of flow adjacent to membrane surface. High velocity results in high sheer- induced lift force which helps to lift the substances and does not allow them to settle down on the membrane surface. Then, the critical will increase.

- At 2.5 m/s of inlet velocity, large size of particle, coefficient of restitution was 1, and special rod baffle purposed the lowest energy consumption for each parametric comparison. Thus, this parameter offered a high performance of star-shaped microfiltration

**Recommendations**

This research simulation was worked under referable paper of Gesan et al 2001 and Chiu et al 2005. Therefore, the limitation of this research was lacked some information. Moreover, the assumption of this research was neglected the inter-particle interaction. Thus, the simulation result was deviate from the experiment result. Accordingly, it should be setup a real laboratory of membrane separation for conducting the input parameter and it should be setup a camera for taking a photo of particle fouling in microfiltration membrane for realistic of the result.
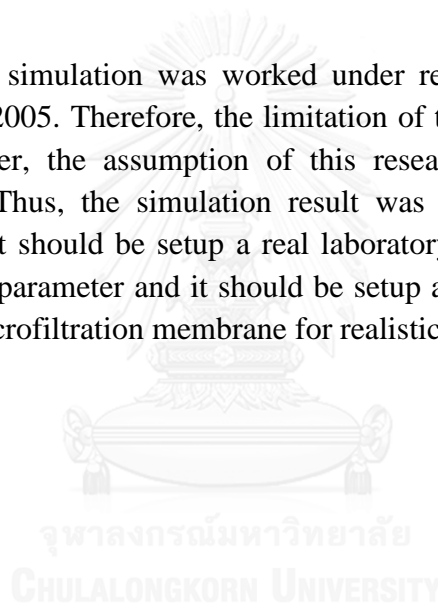
# REFERENCES

1. OECD guideline for testing number 302A. 1981.
2. OECD guideline for testing number 303A. 2001.
3. Chiu, T.Y. and A.E. James, Effects of axial baffles in non-circular multi-channel ceramic membranes using organic feed. Separation and Purification Technology, 2006. 51(3): p. 233-239.
4. Case Study Star-Sep™ Ceramic Membranes in the Pharmaceuticals Industry. 2013.
5. Chiu, T.Y. and A.E. James, Critical flux determination of non-circular multi-channel ceramic membranes using TiO2 suspensions. Journal of Membrane Science, 2005. 254(1-2): p. 295-301.
6. Xu, N., et al., Application of turbulence promoters in ceramic membrane bioreactor used for municipal wastewater reclamation. Journal of Membrane Science, 2002. 210(2): p. 307-313.
7. Gupta, B.B., et al., A helical baffle for cross-flow microfiltration. Journal of Membrane Science, 1995. 102(C): p. 31-42.
8. Broussous, L., et al., An experimental study of helically stamped ceramic microfiltration membranes using bentonite suspensions. Separation and Purification Technology, 2001. 24(1-2): p. 205-221.
9. Liu, Y., et al., CFD simulations of turbulent flow in baffle-filled membrane tubes. Separation and Purification Technology, 2009. 67(1): p. 14-20.
10. Gésan-Guiziou, G., R.J. Wakeman, and G. Daufin, Stability of latex crossflow filtration: Cake properties and critical conditions of deposition. Chemical Engineering Journal, 2002. 85(1): p. 27-34.
11. OECD 303A: Biodegradation of Chemicals- Activated Sludge Simulation Test.
12. Amin Reza, R., Membrane fouling during hollow fiber ultrafiltration of protein solution, in Chemical Engineering. 2010, University of Waterloo.
13. Cheryan, M., Ultrafiltration and microfiltration handbook. 1998.
14. SPECTRUM® LABORATORIES. 1995; Available from: http://www.spectrumlabs.com/filtration/Edge.html.
15. Garcia, F.J.G. and T.Y. Chiu, Economic aspects of critical flux operability in star shaped microfiltration membranes: Influence of some operating conditions. Journal of Membrane Science, 2008. 325(2): p. 641-646.
16. Cheryan, M. and N. Rajagopalan, Membrane processing of oily streams. Wastewater treatment and waste reduction. Journal of Membrane Science, 1998. 151(1): p. 13-28.
17. Brandsma, R.L. and S.S.H. Rizvi, Depletion of whey proteins and calcium by microfiltration of acidified skim milk prior to cheese making. Journal of Dairy Science, 1999. 82(10): p. 2063-2069.
18. Jiraratananon, R. and A. Chanachai, A study of fouling in the ultrafiltration of passion fruit juice. Journal of Membrane Science, 1996. 111(1): p. 39-48.
19. Bowen, W.R., J.I. Calvo, and A. Hernández, Steps of membrane blocking in flux decline during protein microfiltration. Journal of Membrane Science, 1995. 101(1-2): p. 153-165.

20. Yuan, w.M., B.; Shane, C.; Shane, C.;, CFD simulation of membrane filtration zone in submerge hollow fibre membrane bioreactor using a porous media approach. Journal of Membrane Science 2010(363): p. 57-66.
21. Inc, A., ANSYS FLUENT 14.5. 2013.
22. Liu, Y.G., H.E.; Ding , L.; Dou, H.; Ju, J.; Li, B.;, Experiment and CFD studies on performance of microfiltration enhanced by turbulence promoter. Chinese journal of chemical engineering 2012. 20(4): p. 617-624.
23. Ahmed, S.T.S., M.; Jahedi, J.; Hashib, M.; , CFD simulation of turbulence promoters in tubular membrane chanel. Desalination, 2011. 276: p. 191-198.
24. Hwang, K.Y.-S., Y., Numerical simulation of particle depositon in cross flow microfiltration of binary particle. Tamkang journal of science and engineering 2001. 4: p. 119-125.
25. Altmann, J.R., S. , Particle deposition and layer formation at the cross flow microfiltration. Journal of Membrane Science 1996. 124: p. 119-128.
26. Van Dinther, A.M.C., et al., Flow-induced particle migration in microchannels for improved microfiltration processes. Microfluidics and Nanofluidics, 2013. 15(4): p. 451-465.
27. Rahimi, M., et al., CFD and experimental studies of fouling of a microfiltration membrane. Chemical Engineering and Processing: Process Intensification, 2009. 48(9): p. 1405-1413.
28. Allen, T.O., F.; David, j.; David, C., Finite element model of cricket ball impacting a bat. Procedia engineering  2014. 72: p. 521-526.
29. Li, X., et al. Comparison of turbulence promoter geometry on flow pattern from view point of field synergy principle. in Procedia Environmental Sciences. 2011.
30. Chiu, T.Y. and A.E. James, Critical flux enhancement in gas assisted microfiltration. Journal of Membrane Science, 2006. 281(1-2): p. 274-280.

**APPENDIX**

# APPENDIX A

# CREATE DOMAIN

In this study, WORK BENCH 14.5 (Ansys Fluent 14.5, Lebanon) was used to create domain of tubular and star-shaped microfiltration membrane.

Procedure

1. **Start > Programs > Lab Apps > Workbench 14.5 > Geometry**
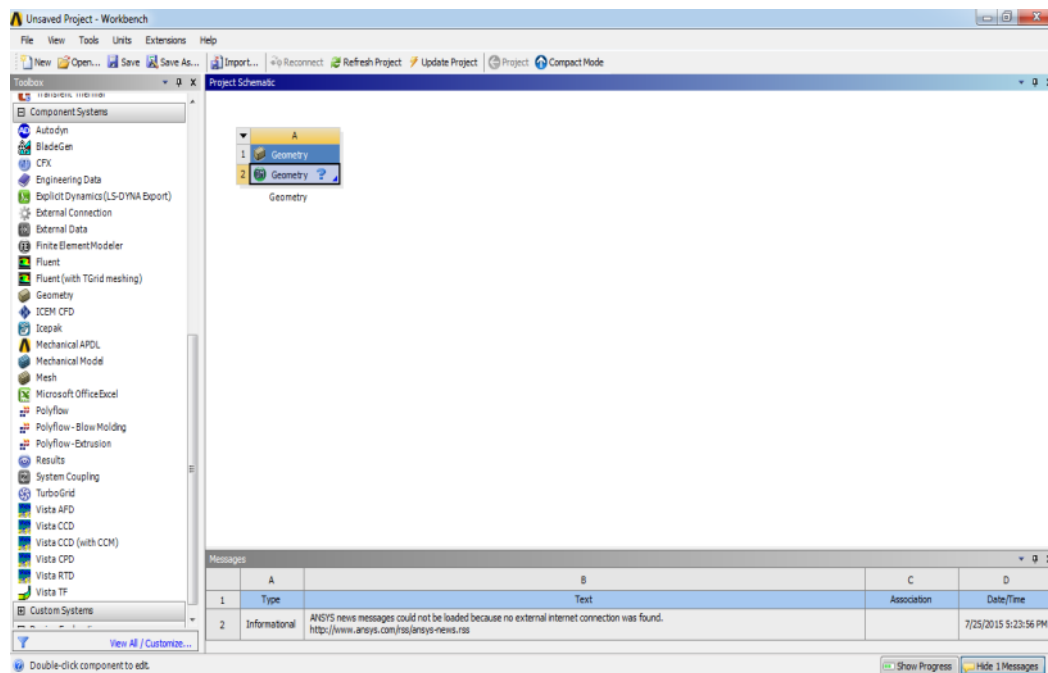


**Figure A.1** The project schematic workbench window.

2. **XY plane** ![XYPlane] **> New sketch** ![sketch icon] **> Membrane > Circle** ![Circle] **> Generate** ![Generate]

Workbench graphic was created on xy-plane and drawn the circle with 20 mm of diameter.
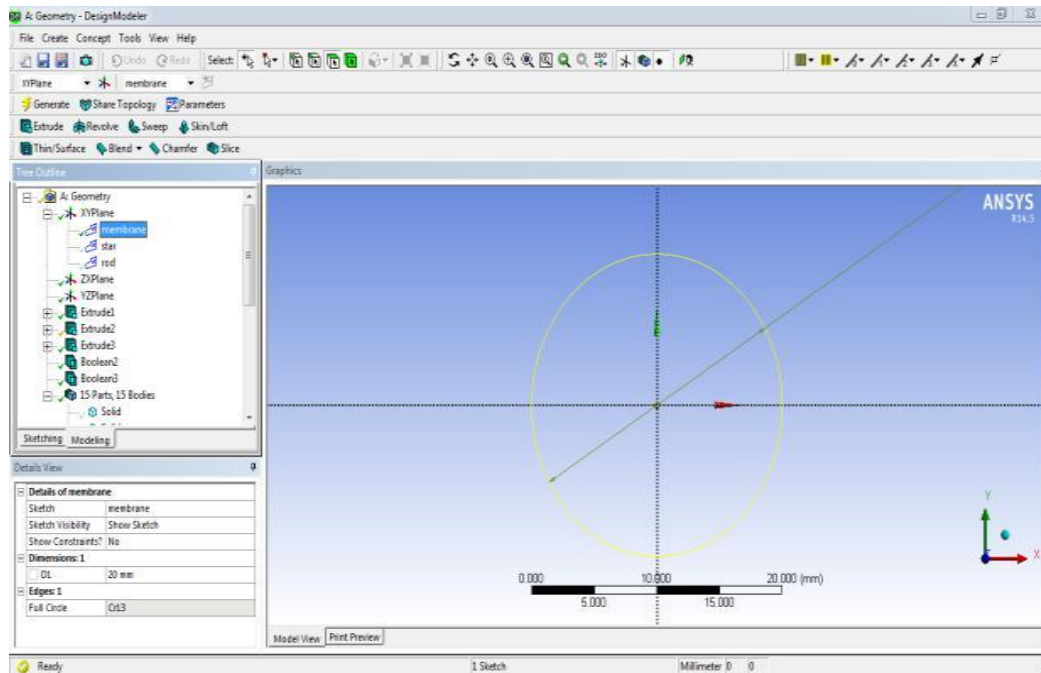
**Figure A.2** Create membrane structure.

3. **XY plane** ![XYPlane icon] **XYPlane** > **New sketch** ![sketch icon] > **Sketch** > **Line** ![Line icon] **Line** > **Generate** ![Generate icon] **Generate**

Workbench graphic was created on xy-plane and drawn the asterisk geometry. After that, the circle with 2.8mm inner diameter and 4.6 mm outer diameter were created on the point of intersection.
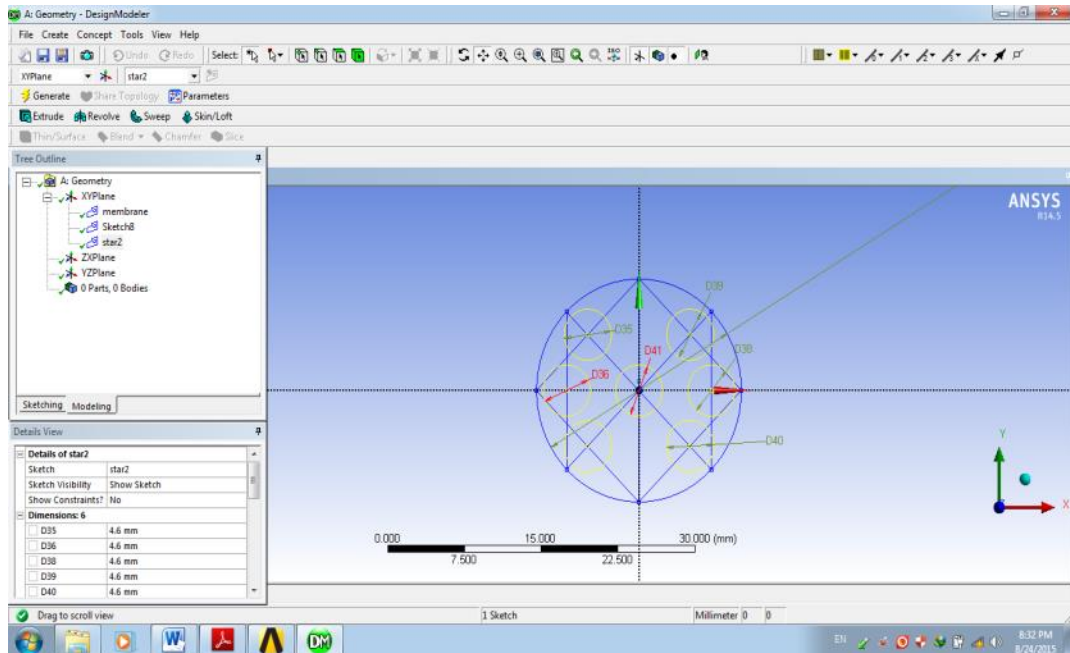
**Figure A.3** Create sketch structure.

4. **XY plane**  **> New sketch**  **> Star > Line**  **> Generate**


The asterisk geometry in sketch was deleted. Then, workbench graphic was created on xy-plane and combined the two tri angle with 60º of each angle into the circle sketch.
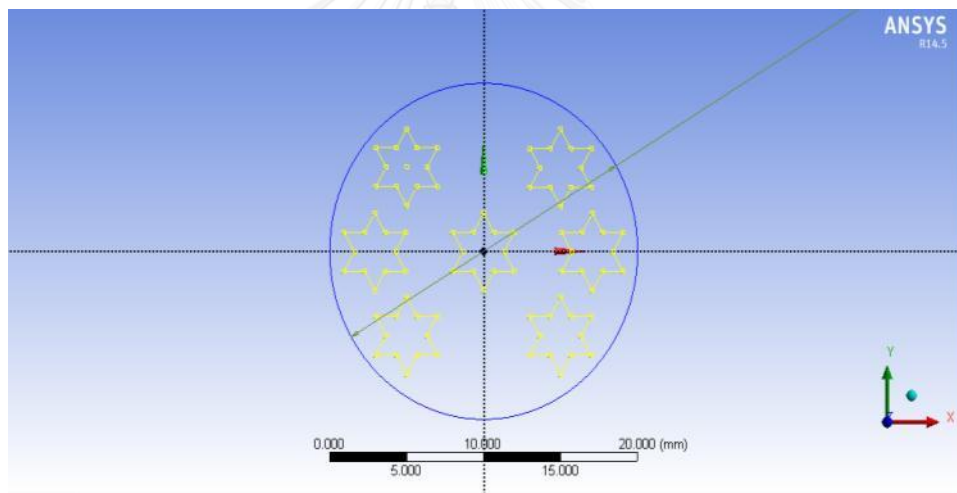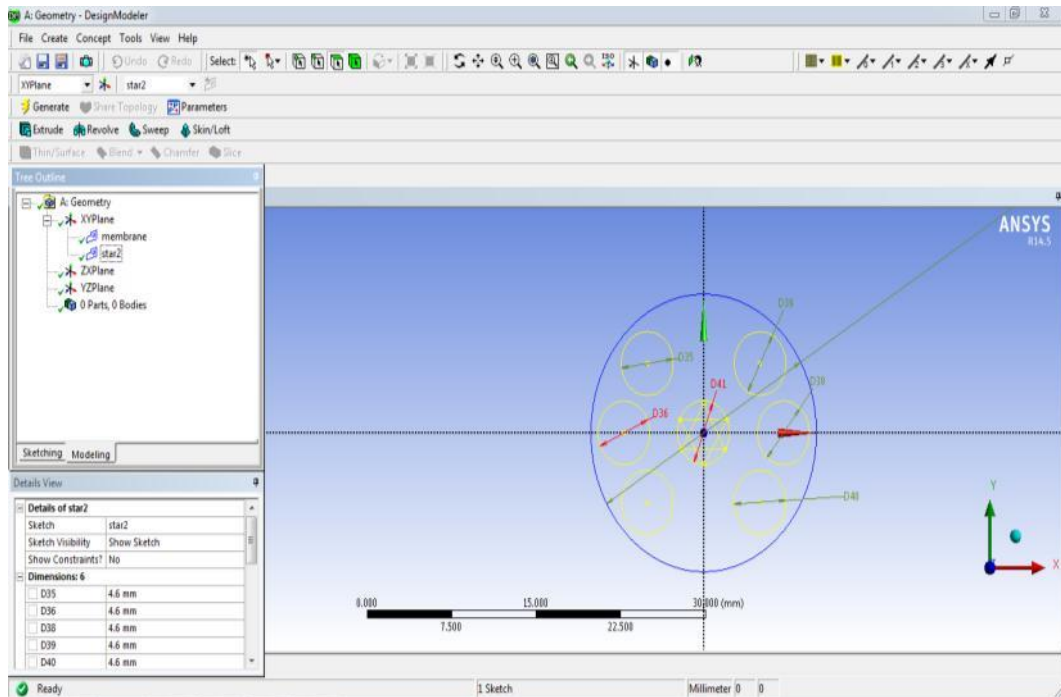
**Figure A.4** Create star structure.

5. **XY plane** ⋏ XYPlane **> New sketch** 🖼 **> Membrane > Circle** ⊙ Circle **>**

   **Generate** ⚡ Generate

The rod geometry was created in to the middle of star geometry by using create circle

button with 0.9 mm of diameter.
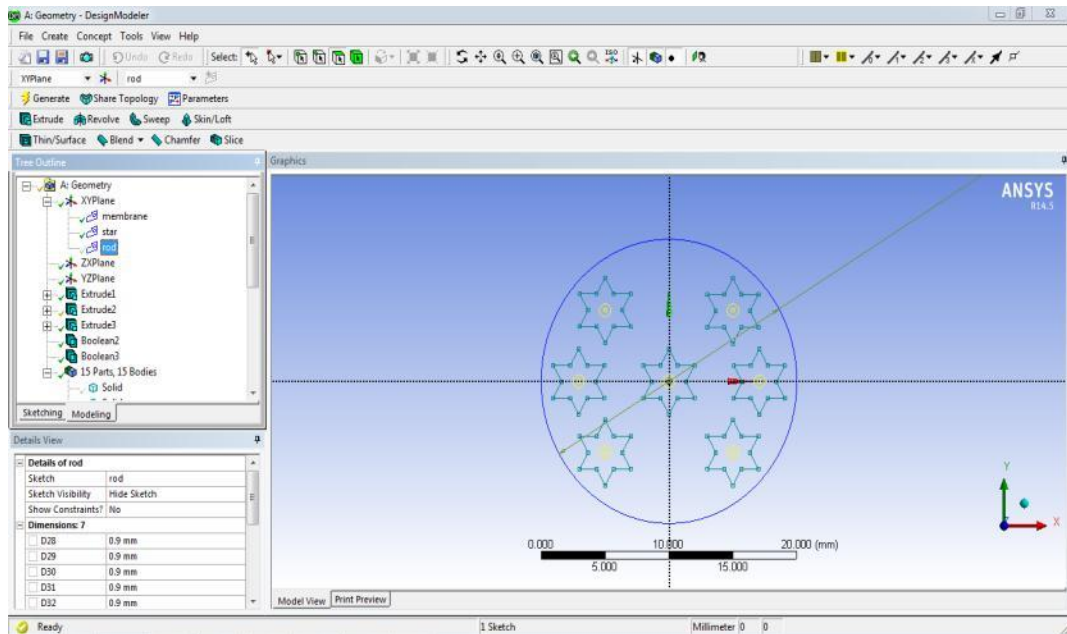
**Figure A.5** Create rod structure.

**6. Extrude**  **> Face of rod**  **> Generate** 

The extrude method is tool which expands the drawing structure. Rod structure was extruded in the normal direction with 600 mm of length by using add frozen operation (Shift + left click on the face of rod) then click generate.
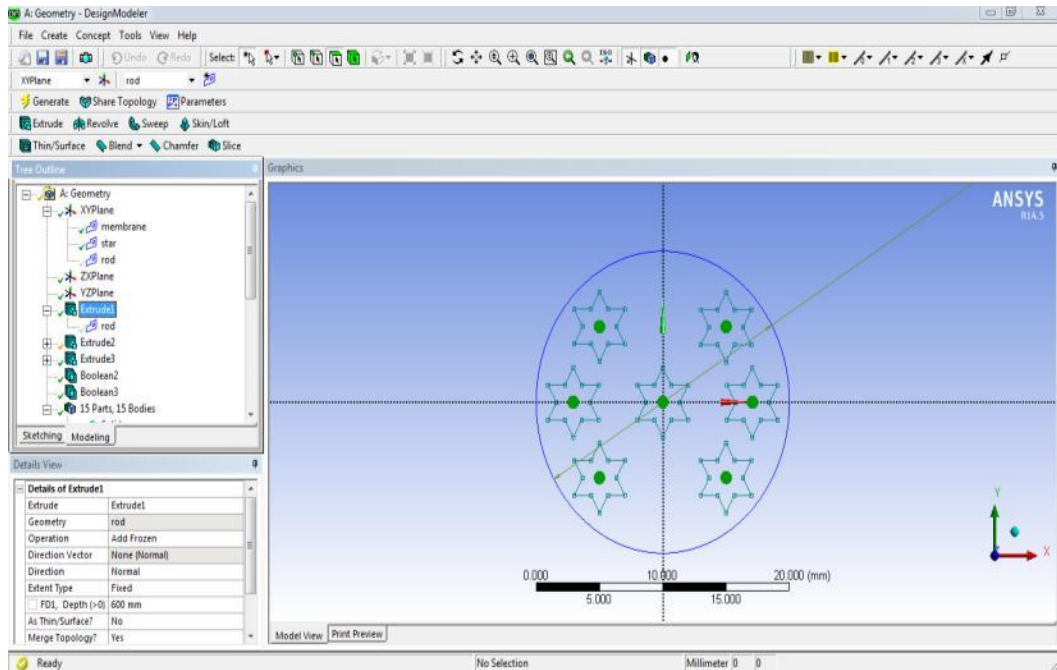
**Figure A.6** Extrude method of rod

**7. Extrude** ![Extrude] **> Face of membrane** ![icon] **> Generate** ![Generate]

Membrane structure was extruded in the normal direction with 600 mm of length by using add frozen operation (Shift + left click on the face of membrane) then click generate.
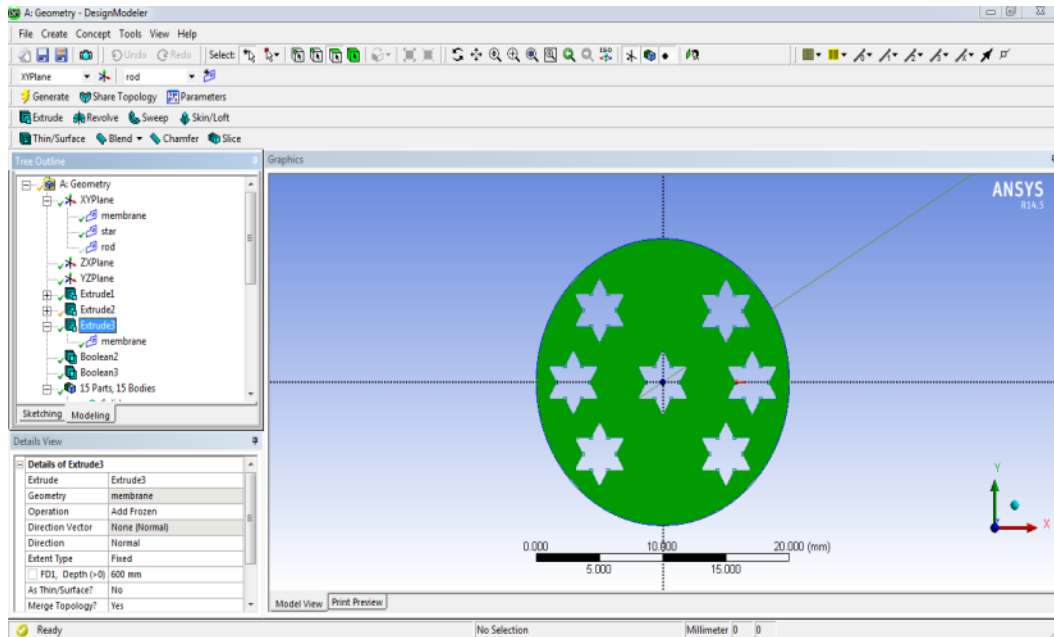
**Figure A.7** Extrude method of membrane.

8. **Extrude** ![Extrude icon] **> Face of star** ![icon] **> Generate** ![Generate icon]

Star structure was extruded in the normal direction with 600 mm of length by using add frozen operation (Shift + left click on the face of star) then click generate.
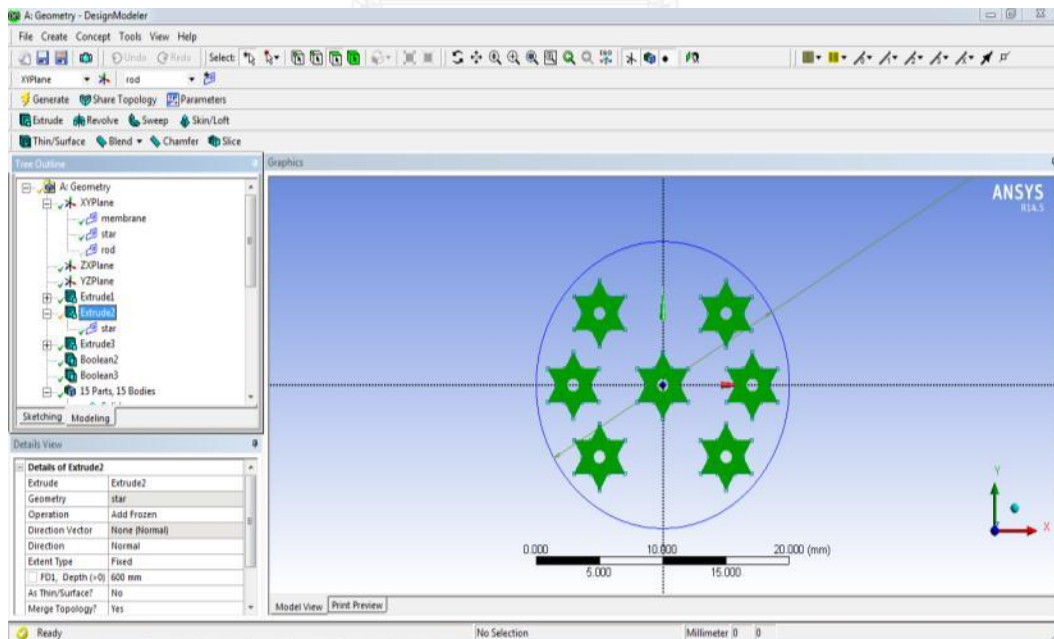


**Figure A.8** Extrude method of star.

**9. Boolean** 🔲 Boolean **> Body of star and membrane** 🔲 **> Generate** ⚡Generate

Boolean method is the tool which separates from each other. Boolean star and membrane body was created by boolean method command (Shift + left click on the body of star and membrane) then click generate.
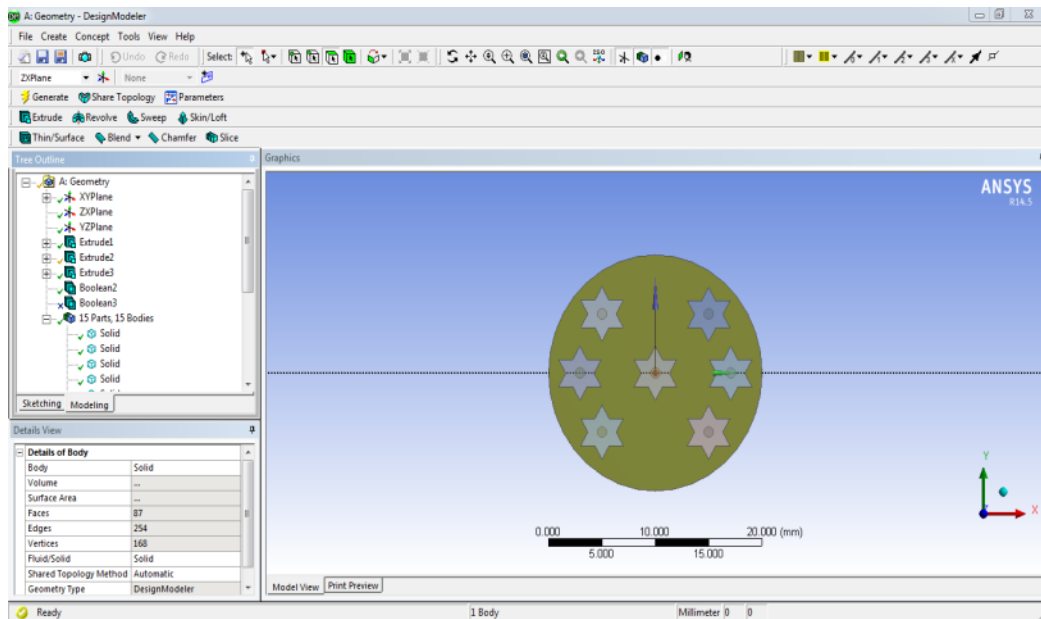


**Figure A.9** Boolean method of star and membrane.

**10. Boolean** 🔲 Boolean **> Body of star and rod** 🔲 **> Generate** ⚡Generate

Boolean star and rod body was created by boolean method command (Shift + left click on the body of star and rod) then click generate.
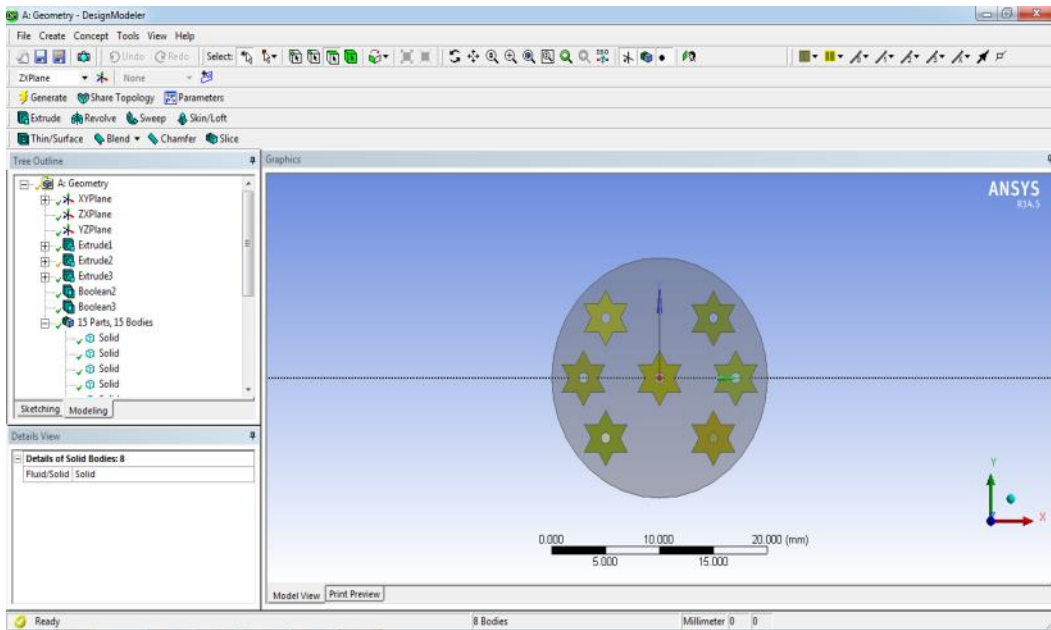
**Figure A.10** Boolean method of star and rod.

## APPENDIX B

## Meshing

Procedure

**1.)** After creating domain, the meshing icon (B) was dragged in to geometry icon (A).
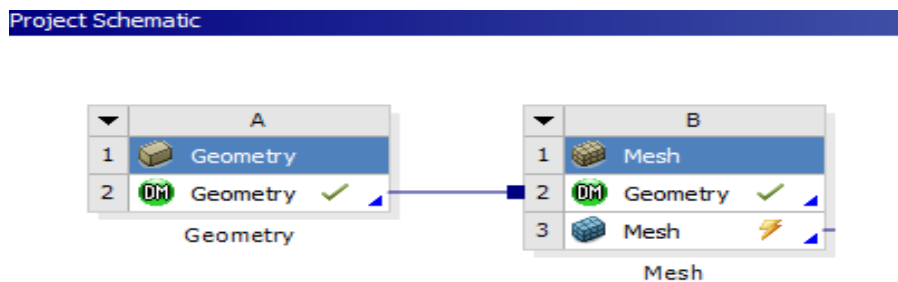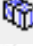


**Figure B.1** FLUENT schematic window

**2.)** Mesh Mesh > Method Method > Sweep > Face of rod > Update Update

Sweep rod geometry was created by sweep method command (Shift + left click on the face of rod) then click Update.
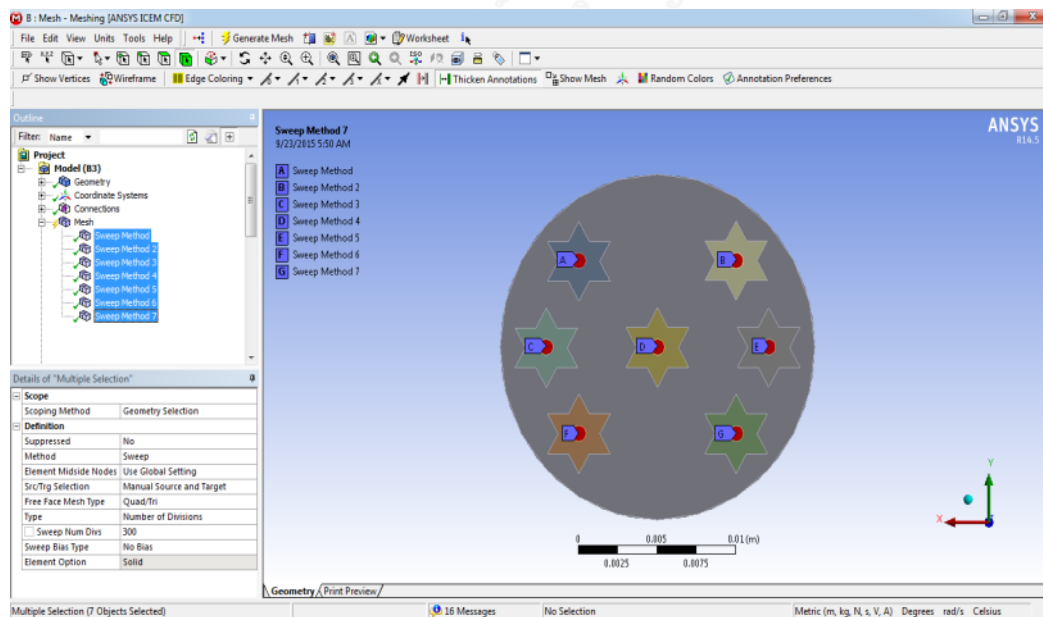


**Figure B.2** Sweep method of rod

**3.) Mesh** 🔳 Mesh **> Sizing** 🔳 Sizing **> Face of rod** 🖼️ **> Update** ⚡ Update

Face sizing of rod was created after sweep method command by (Shift + left click on the face of rod) then click Update.
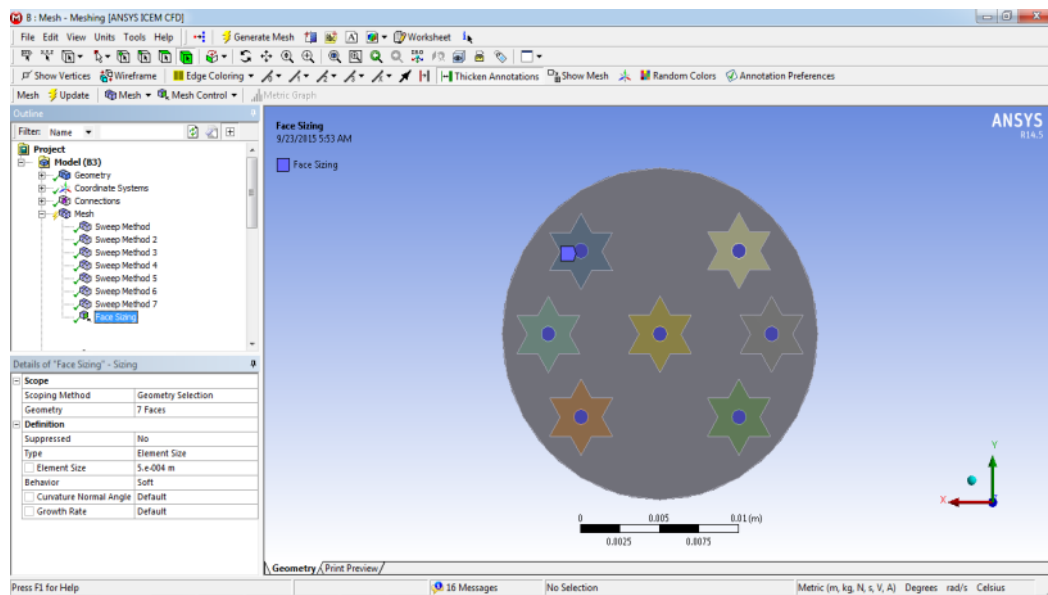


**Figure B.3** Sizing method of rod.

**4.) Mesh** 🔳 Mesh **> Method** 🔳 Method **> Sweep > Face of star** 🖼️ **> Update**

⚡ Update

Sweep star geometry was created by sweep method command (Shift + left click on the face of star) then click Update.
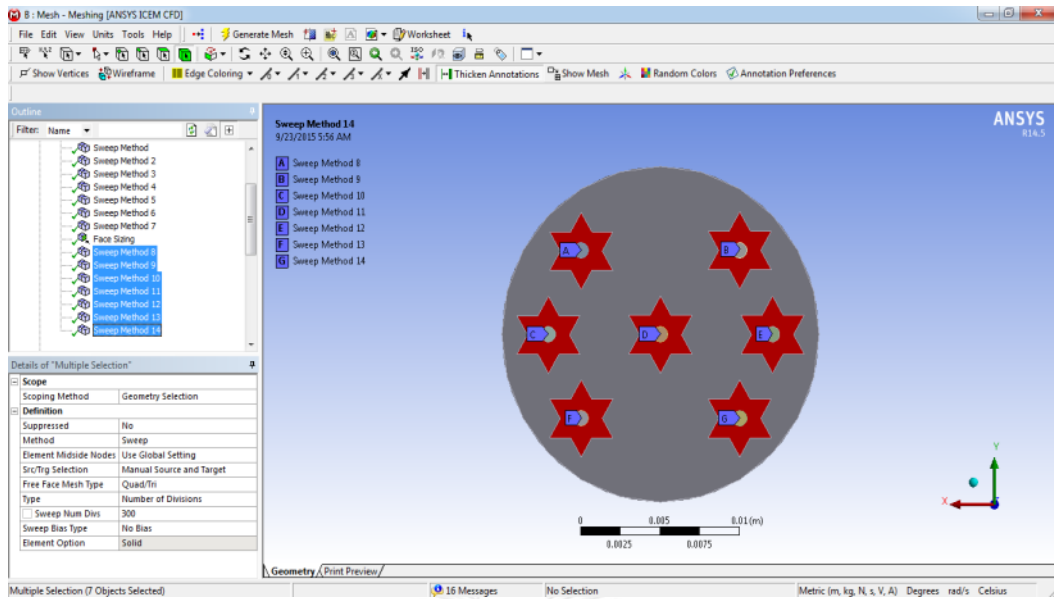
**Figure B.4** Sweep method of star.

5.) **Mesh** 🔲 Mesh > **Sizing** 🔲 Sizing > Face of star 🔲 > Update ⚡ Update

Face sizing of star was created after sweep method command by (Shift + left click on the face of star) then click Update.
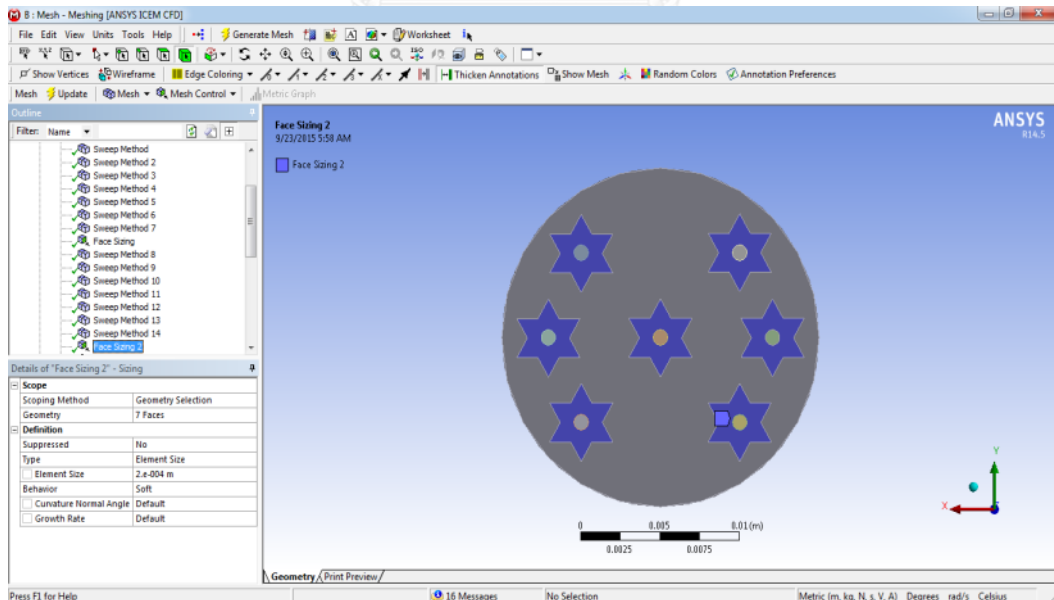


**Figure B.5** Sizing method of star.

**6.) Define > Method** [Method] **> Sweep > Face of membrane** [ ] **>**

**Update** [Update]

Sweep membrane geometry was created by sweep method command (Shift + left click on the face of membrane) then click Update.
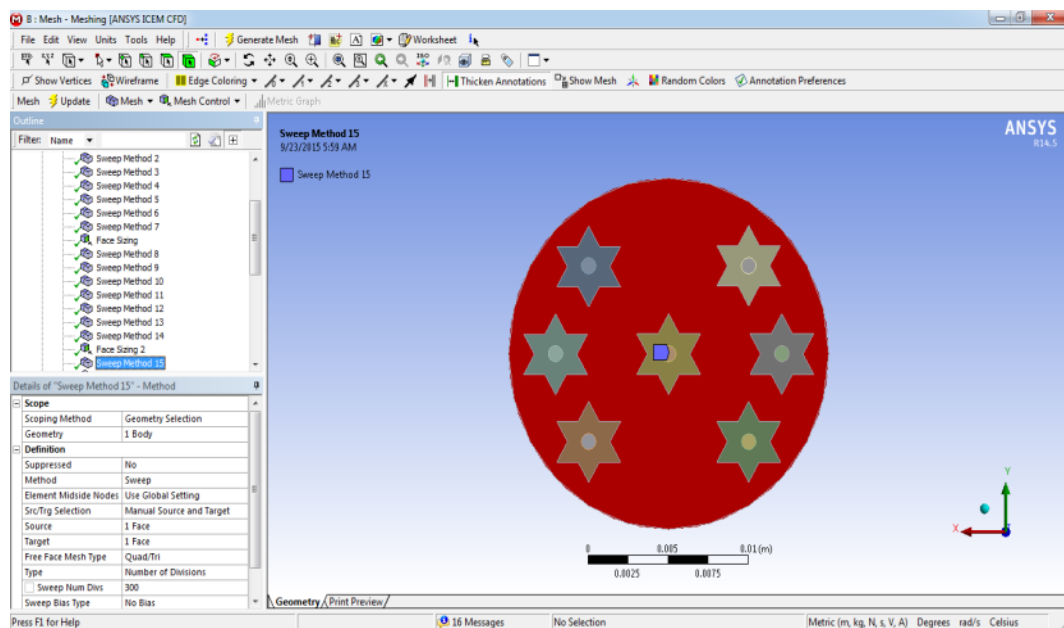


**Figure B.6** Sweep method of membrane.

**7.) Mesh** [Mesh] **> Sizing** [Sizing] **> Face of membrane** [ ] **> Update** [Update]

Face sizing of membrane was created after sweep method command by (Shift + left click on the face of membrane) then click Update.
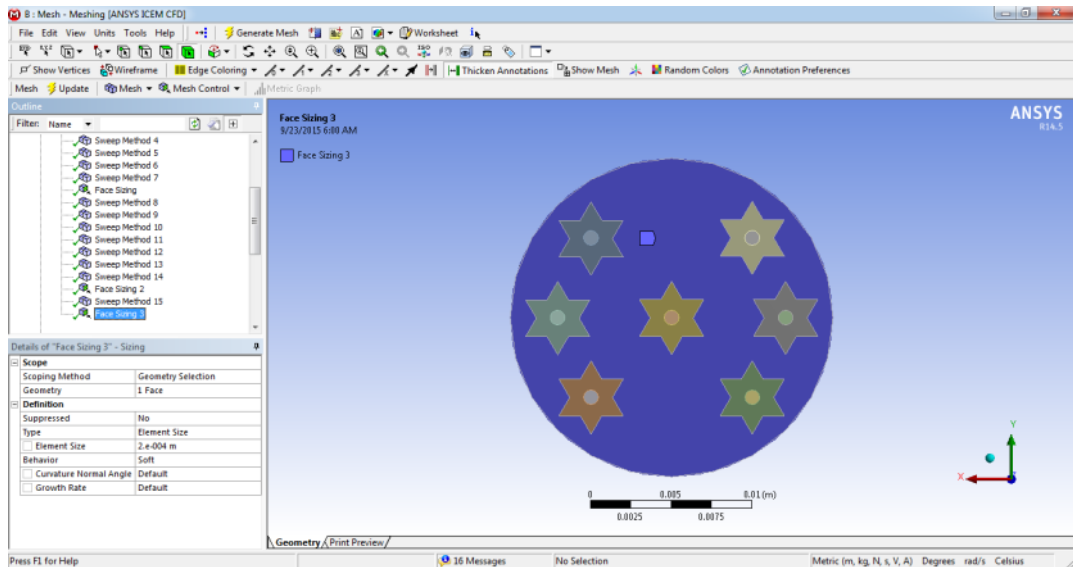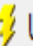
**Figure B.7** Sizing method of membrane.

**8.) Mesh** 🔲 Mesh **> Method** 🔲 Method **>Inflation** 🔺 Inflation **> Edge of star**
🔲 **> Update** ⚡ Update

Inflation method of star was created after sizing method of star by (Shift + left click on the edge of star) then click Update.
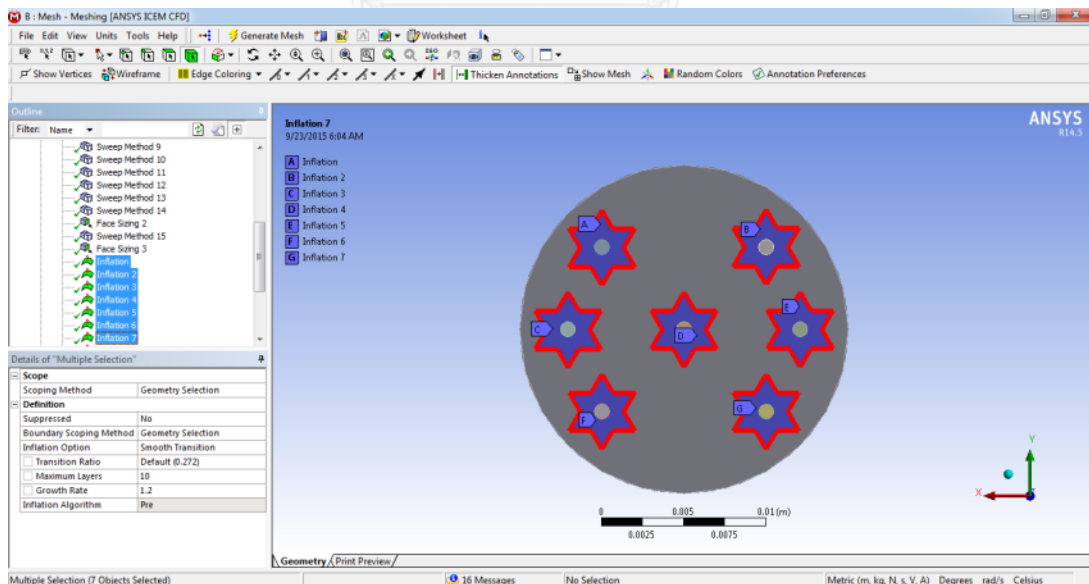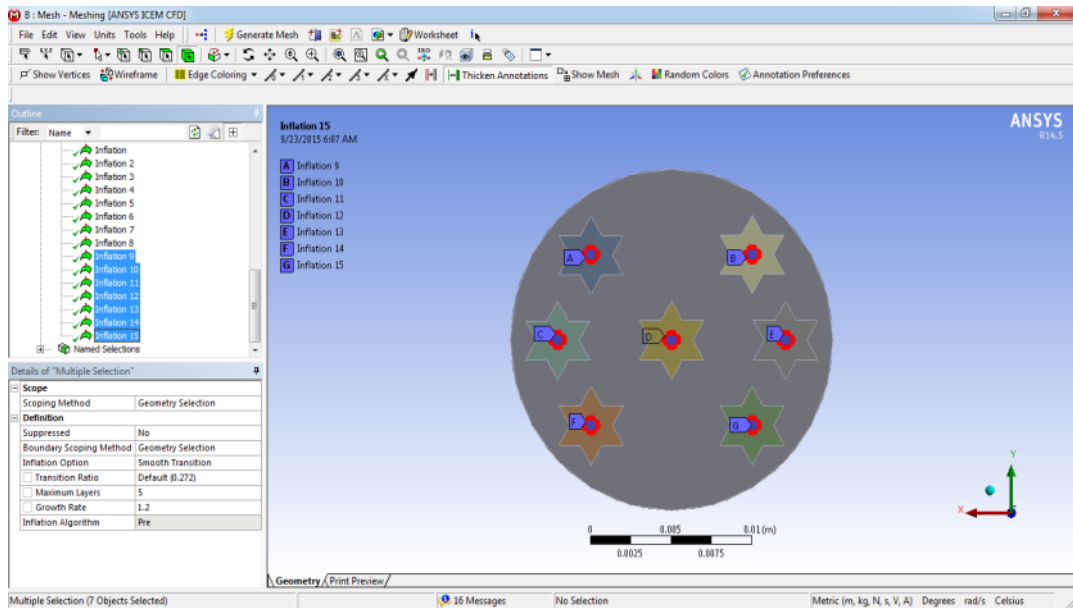


**Figure B.8** Inflation method of star.

**9.) Mesh** 🔲 Mesh **> Method** 🔲 Method **>Inflation** ⛰ Inflation **> Edge of**

**membrane** 🗒 **> Update** ⚡ Update

Inflation method of membrane was created after sizing method of membrane by (Shift + left click on the edge of membrane) then click Update.
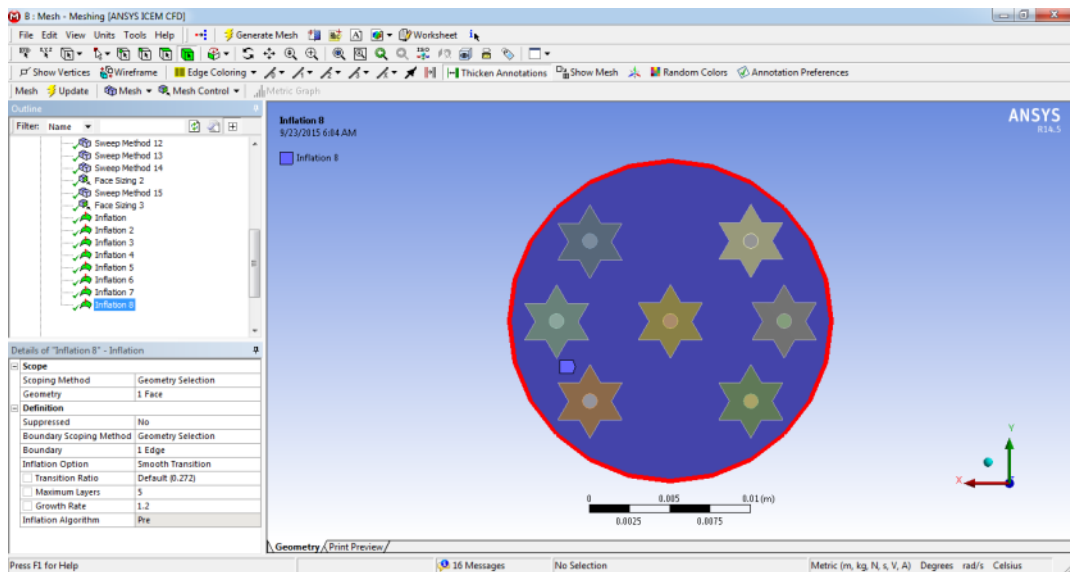


**Figure B.9** Inflation method of membrane.

**10.) Mesh** 🔲 Mesh **> Method** 🔲 Method **>Inflation** ⛰ Inflation **> Edge of rod** 🗒

**> Update** ⚡ Update

Inflation method of rod was created after sizing method of rod by (Shift + left click on the edge of rod) then click Update.

**Figure B.10** Inflation method of rod.

11.) **Generate mesh** ⚡ Generate Mesh

Inflation method of rod was created after sizing method of rod by (Shift + left click all of body) then click Generate mesh.
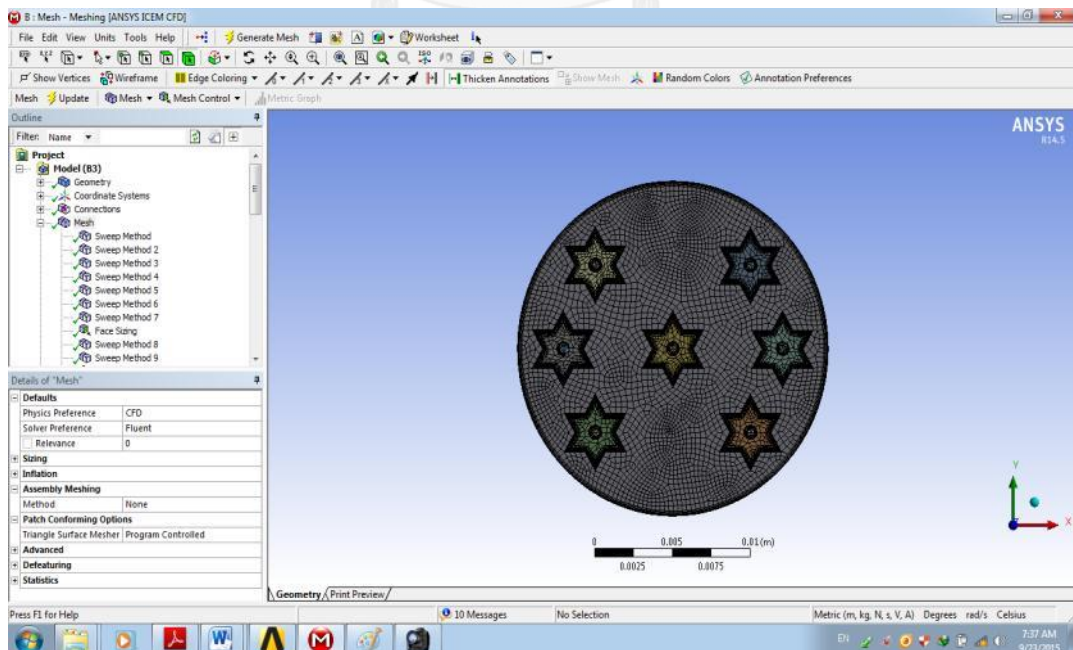


**Figure B.11** Mesh generation.

12.) Model **Model** > **Insert name selection** **Named Selection** > **Body of rod**

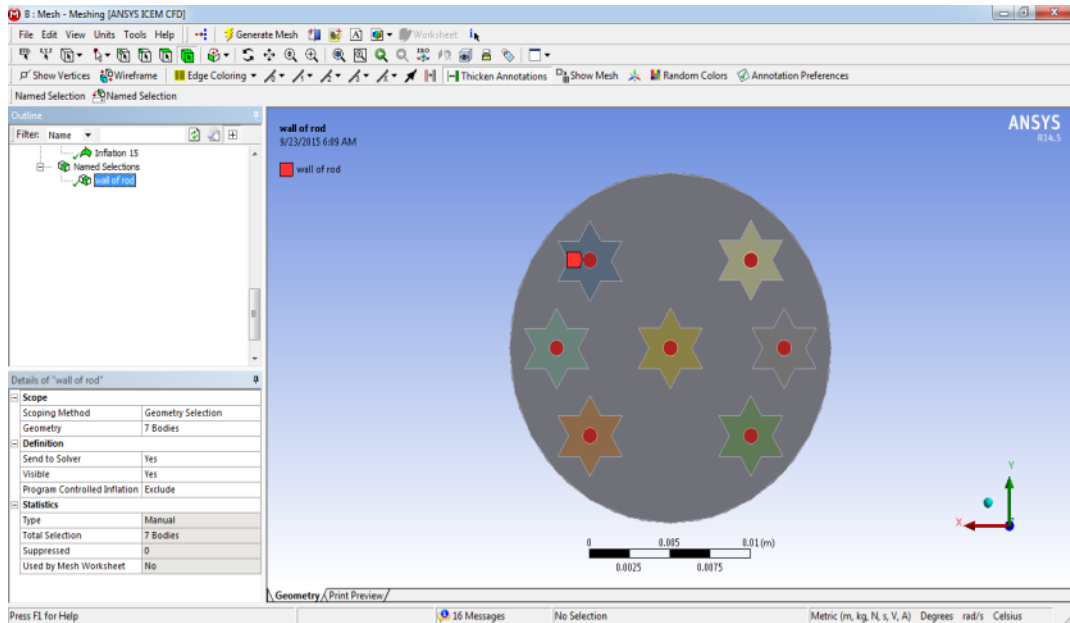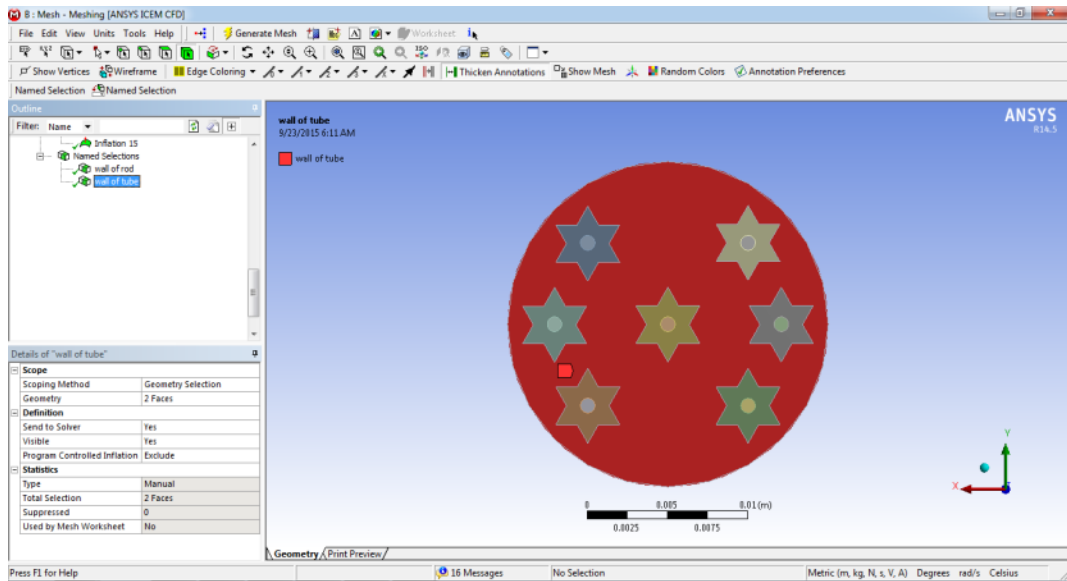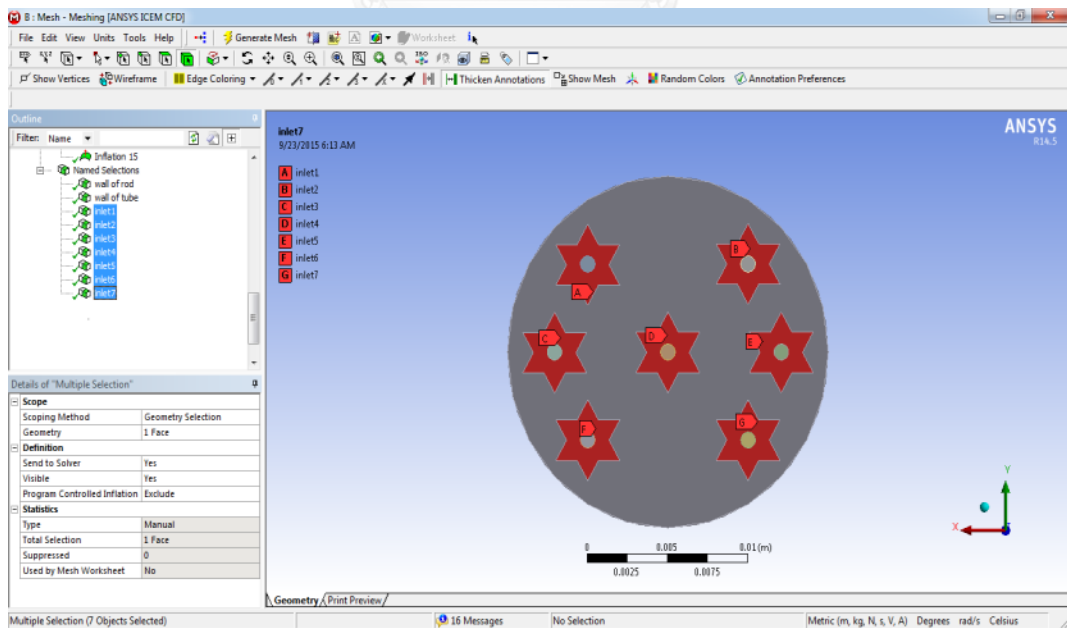The rod geometry was defined to wall boundary (Right click + insert name "wall of rod").



**Figure B.12** The specify boundary condition of rod.

13.) Model **Model** > **Insert name selection** **Named Selection** > **face of membrane**

The membrane geometry was defined to wall boundary (Right click + insert name "wall of membrane").

**Figure B.13** The specify boundary condition of wall of membrane.

**14.)** Model 📦 **Model** > Insert name selection 📑 **Named Selection** > face of star 📋

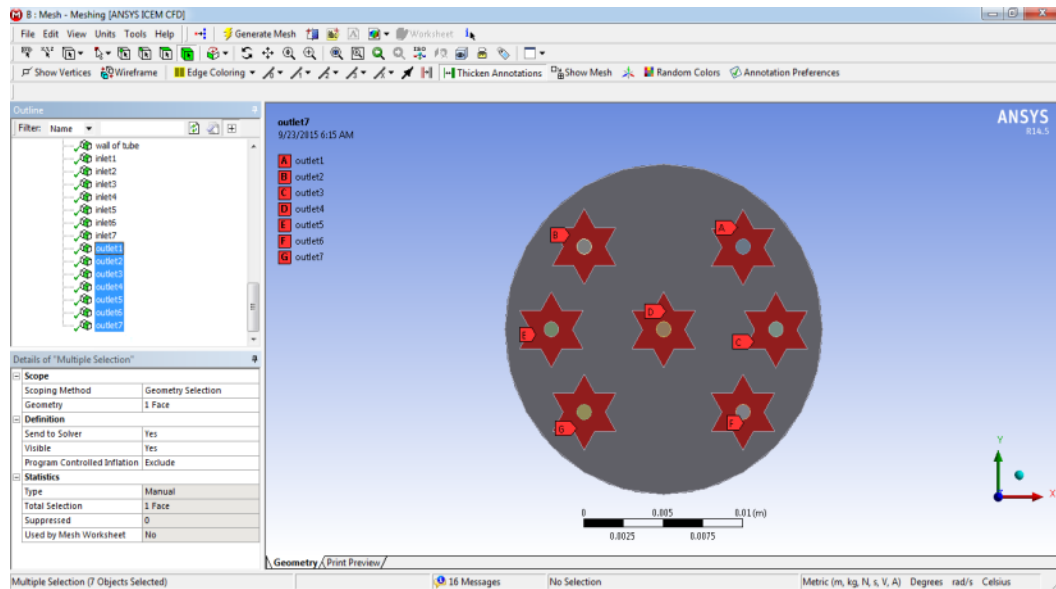The star geometry was defined to velocity inlet boundary (Right click + insert name "inlet").



**Figure B.14** The specify boundary condition of inlet.

**15.) Model** 🔲 Model **> Insert name selection** 📇 Named Selection **> face of star** ▣

The star geometry was defined to pressure outlet boundary (Right click + insert name "outlet").



**Figure B.15** The specify boundary condition of outlet.

**16.) Model** 🔲 Model **> Insert name selection** 📇 Named Selection **> face of membrane** ▣

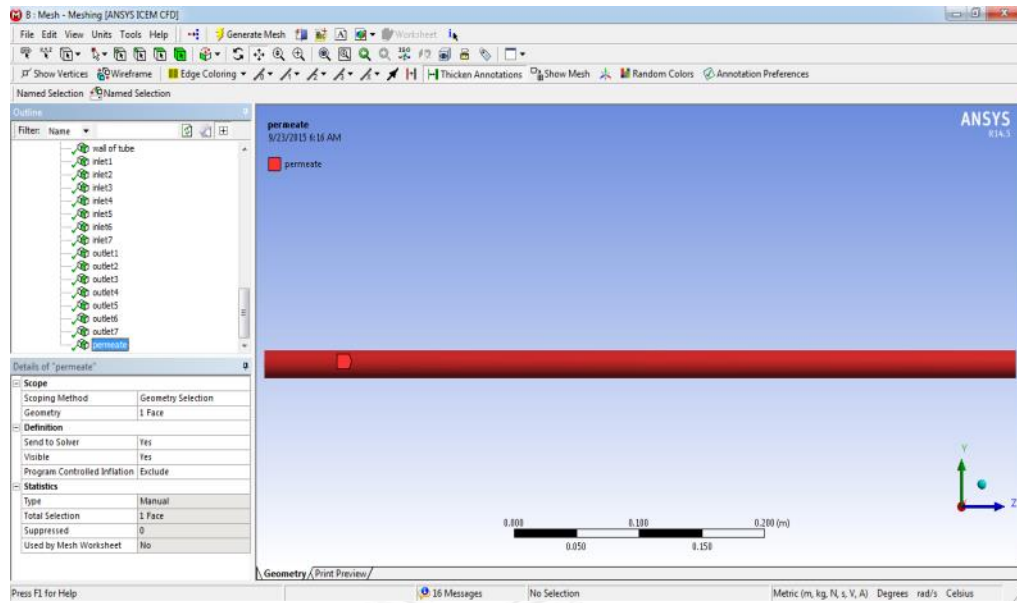The outside of membrane geometry was defined to pressure outlet boundary (Right click + insert name "permeate").

**Figure B.16** The specify boundary condition of permeate.

# APPENDIX C

# SIMULATION IN FLUENT

In this study, FLUENT 14.5 (Ansys Fluent 14.5, Southpointe Canonsburg, PA15317 USA) is the tool for simulating flow of waste water inside tubular and star-shaped microfiltration membrane and incorporating with Work bench 14.5 for domain generation.

**Procedure**

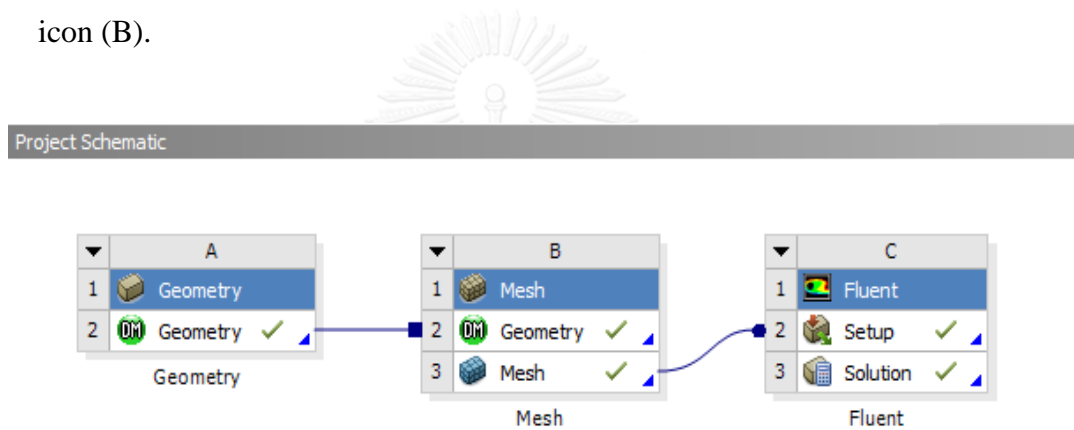1.) After creating domain and meshing, the fluent icon (C) was dragged in to mesh icon (B).



**Figure C.1** FLUENT schematic window.

2.) Clicked on setup and selected the parallel processing in the processing option panel.
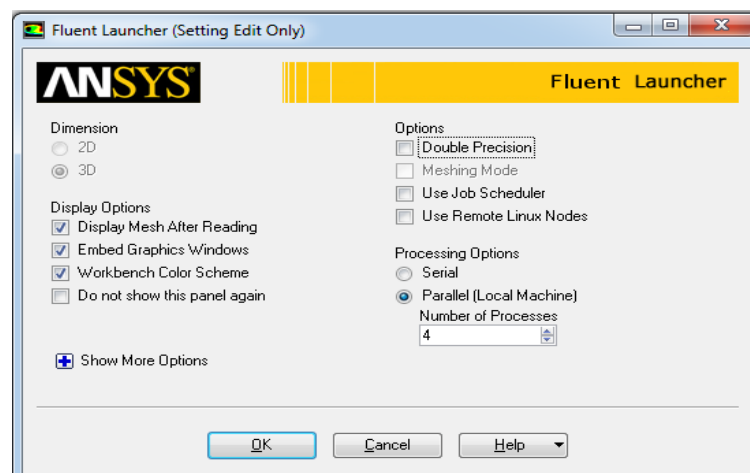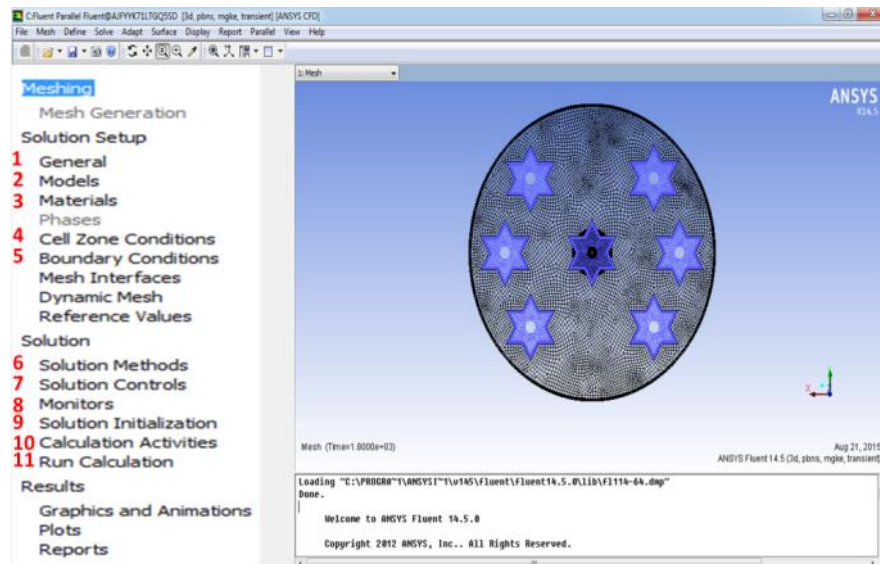


**Figure C.2** FLUENT launcher window.

3.) When lunch to FLUENT software, there are eleventh options for commanding in fluent window.



**Figure C.3** FLUENT command window.

4.) Define > general or operating condition (step 1)

Define general was selected to pressure base, transient because this solver suit for incompressible fluid. Moreover, the continuity equation from pressure based solver was achieved by solving a pressure correction. Absolute velocity formulation, gravity acceleration was 9.81 m/s$^2$ in z direction. Moreover, This simulation work use explicit formation for solving the problem. Because this formation suitable for the variable which unknown value in each cell. Therefore each unknown will appear in only one equation in the system and the equation for the unknown value in each cell can be solved one at a time to give the unknown quantities
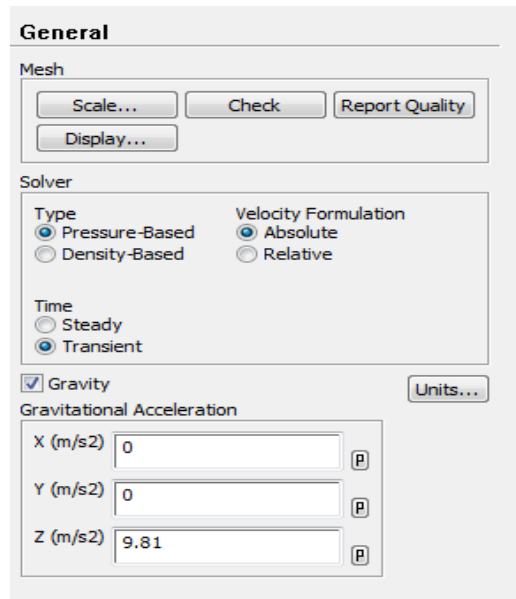
**Figure C.4** Setting of general

5.) Define > Model (step 2)

There are two model used in

5.1 The viscous model was selected. In this study, the turbulence flow was chosen.

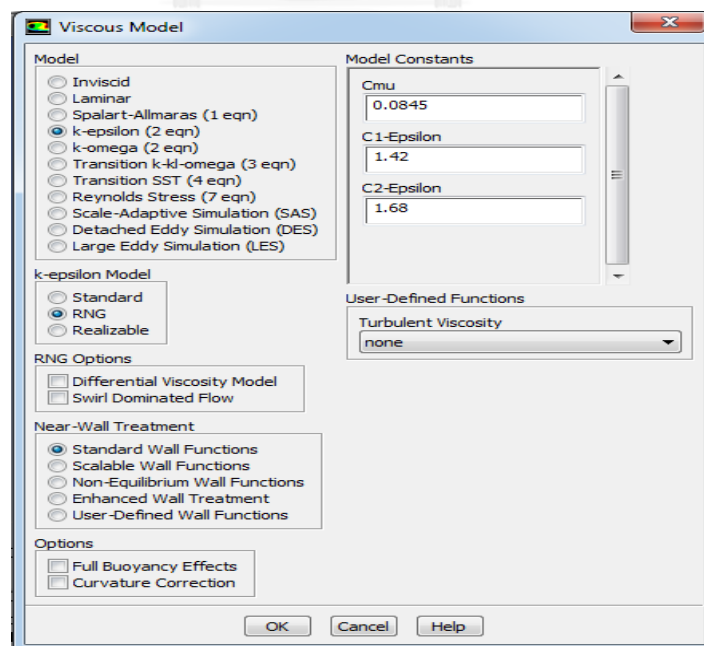**Define > Model > Viscous > K-epsilon > RNG > Standard wall function > OK**



**Figure C.5** Setting of viscous model.

5.2 The discrete phase model was selected. In this study, stochastic was chosen.

**Define > Model > Discrete phase > Stochastic > Saffman lift force > Injection >Ok**

Particle trajectories were modeled on a particle-by-particle basis using the stochastic random-walk model and adding the saffman lift force into discrete phase model. The Guasian method was used to integrate the particle equations. Figure C.7 was performed with particle injection type in FLUENT. Inert particles with seven type were released at the surface of inlet velocity and trapped on the membrane surface. The properties of the ash particle are given below:
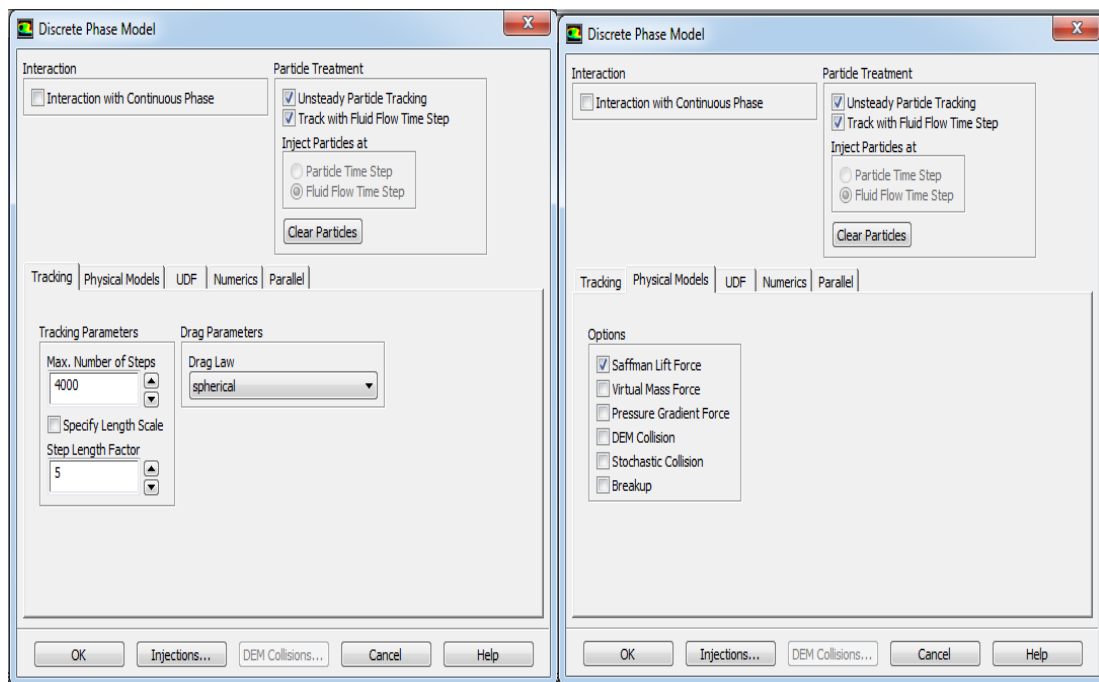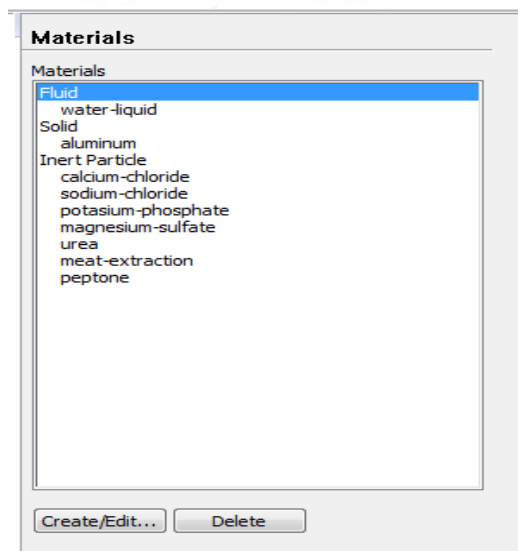


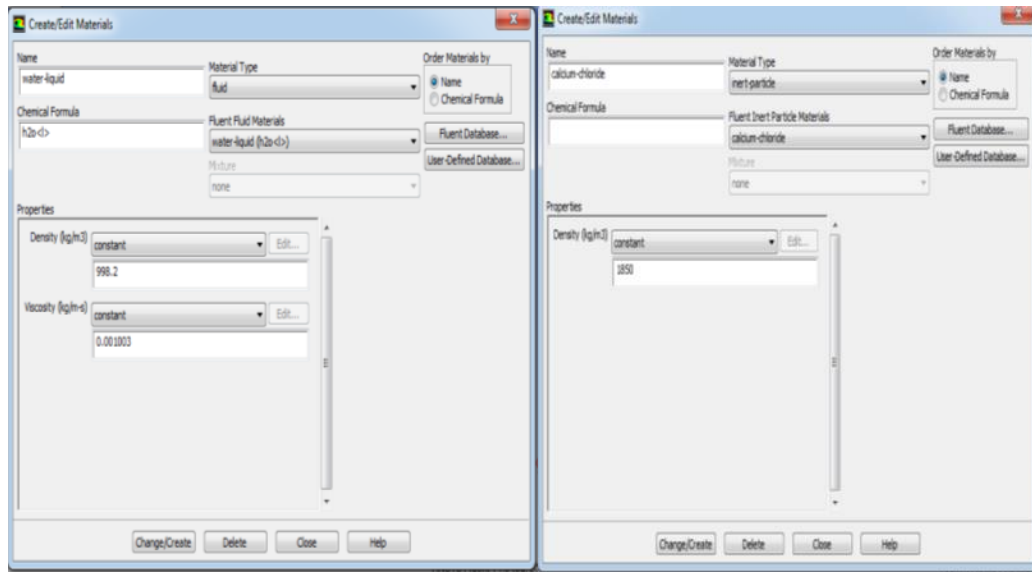**Figure C.6** Setting of discrete phase model
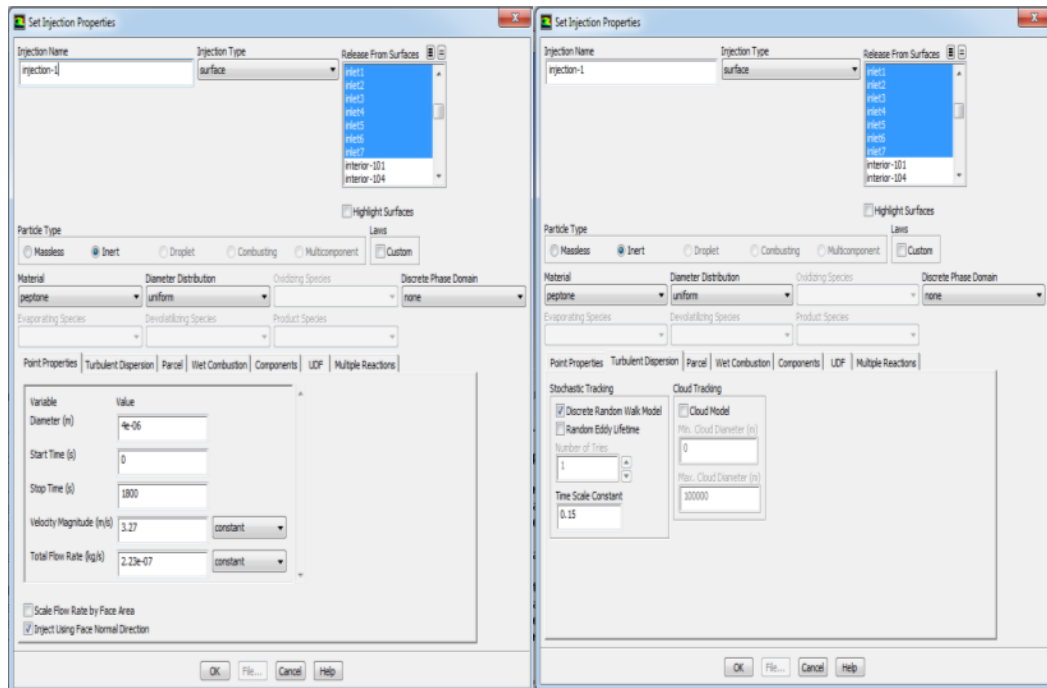
**Figure C.7** Setting of injection in discrete phase model.

6.) Define > Material (step 3)

Material setting was edited to specify the physical property of material such as density and viscosity.



**Figure C.8** Define material.

**Figure C.9** Define and setting the property of fluid and particles.

7.) Define > Cell zone condition (step 4)

Cell zone setting was edited to specify type of domain. Membrane zone was selected to the fluid type with porous media which edited the value of viscous resistance and fluid porosity. Star zones were selected to fluid type without porous zone. Rod baffle was selected to the solid type.
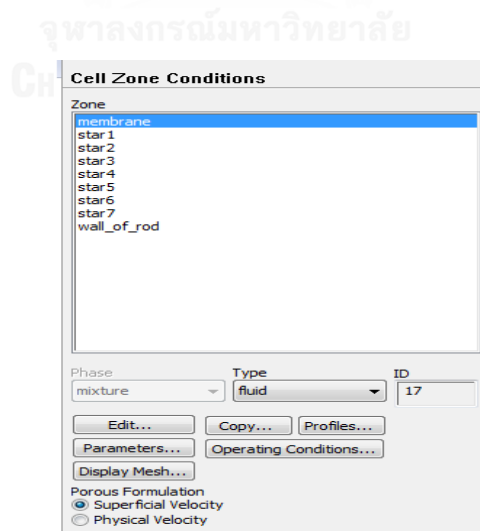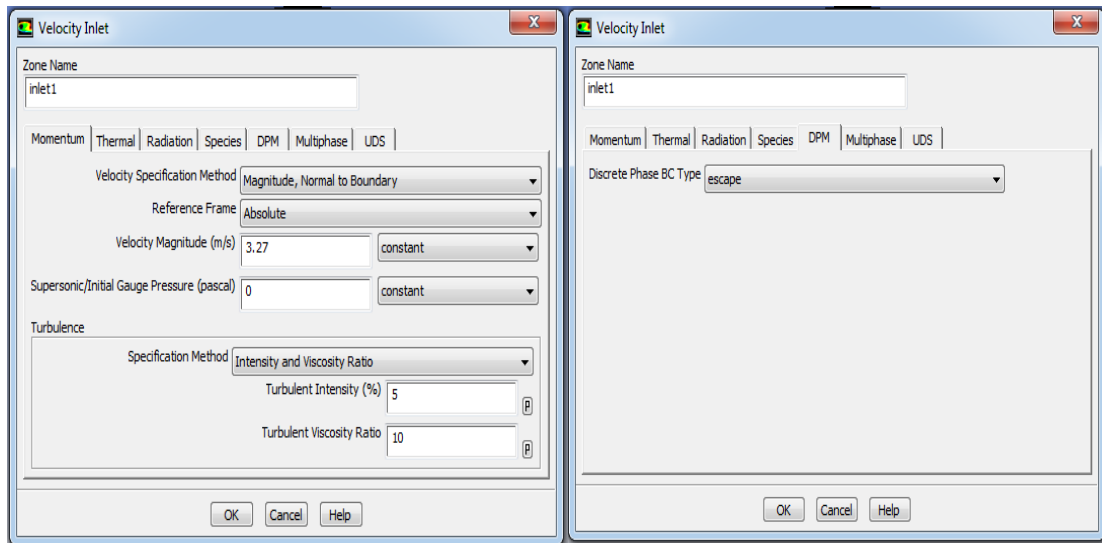


**Figure C.10** Define cell zone condition
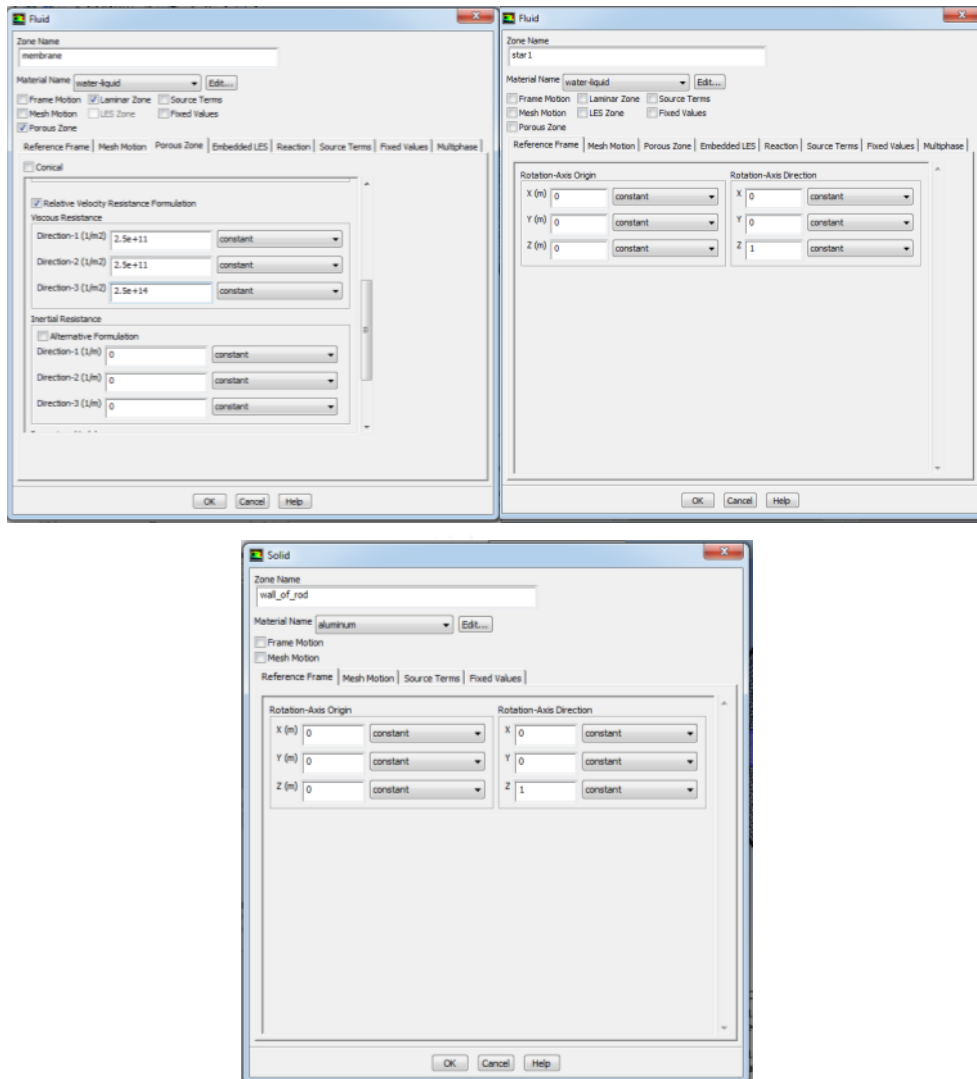
**Figure C.11** Define and setting the property of cell zone condition.

8.) Define > Boundary condition (step 5)

- For inlet boundary condition, the velocity magnitude and discrete phase model (escape) was selected in drop down list.
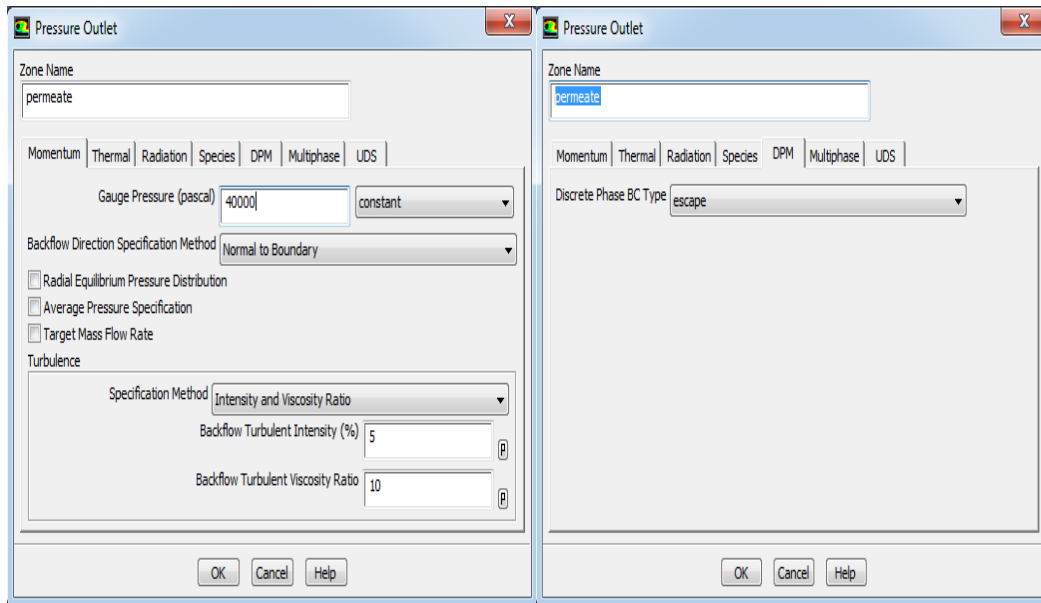
**Figure C.12** Setting of inlet boundary condition.

- For outlet boundary condition, the pressure outlet and discrete phase model (escape) was selected in drop down list.
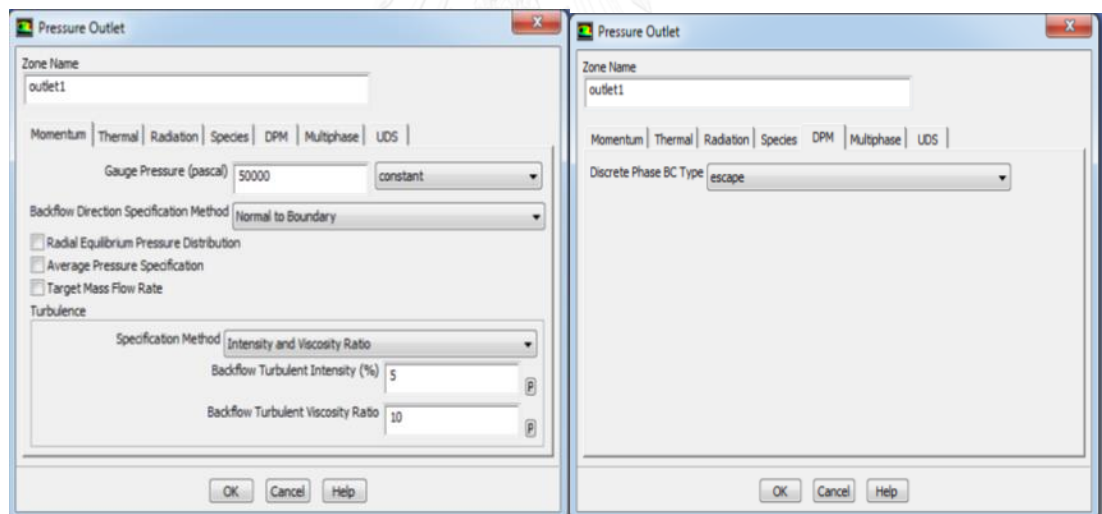


**Figure C.13** Setting of outlet or retentate boundary condition.

- For permeate boundary condition, the pressure outlet and discrete phase model (DPM) was selected in drop down list.

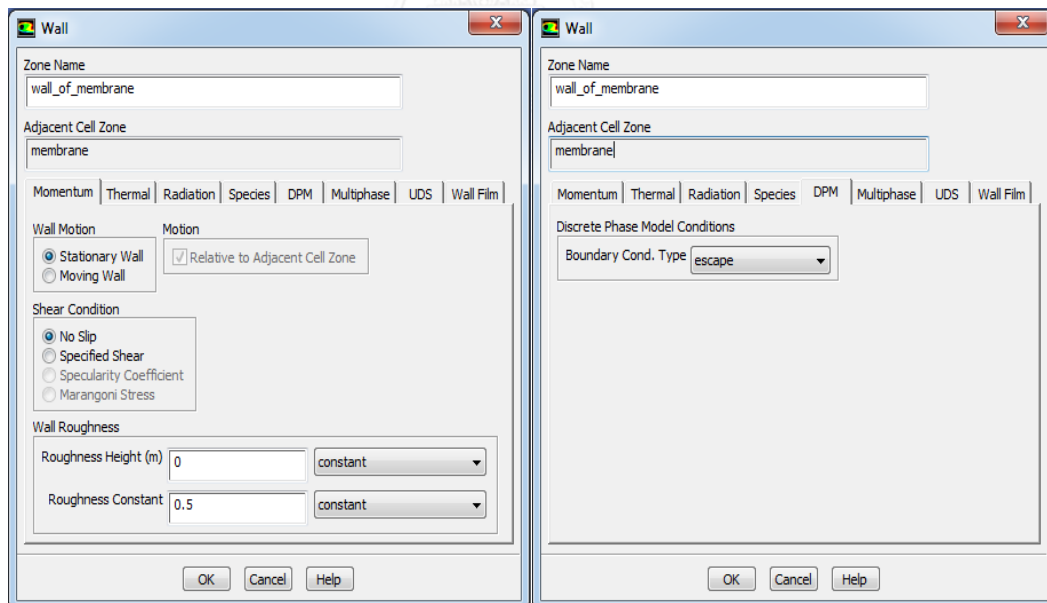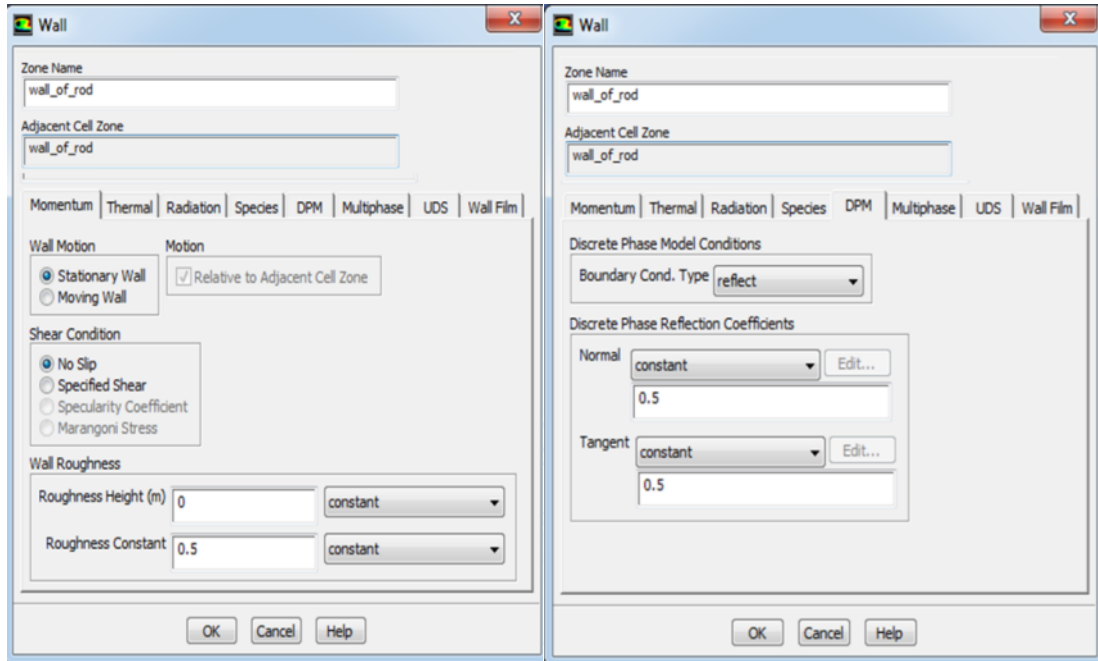**Figure C.14** Setting of outlet or permeate boundary condition.

- For wall of membrane boundary condition, the wall and discrete phase model (escape) was selected in drop down list.



**Figure C.15** Setting of wall of membrane boundary condition.

- For wall of baffle boundary condition, the wall and discrete phase model (reflect) was selected in drop down list.



**Figure C.16** Setting of wall of baffle boundary condition.

- For interior membrane boundary condition porous jump. Face permeability was the inverse value of viscous resistance and discrete phase model (trap) was selected in drop down list.
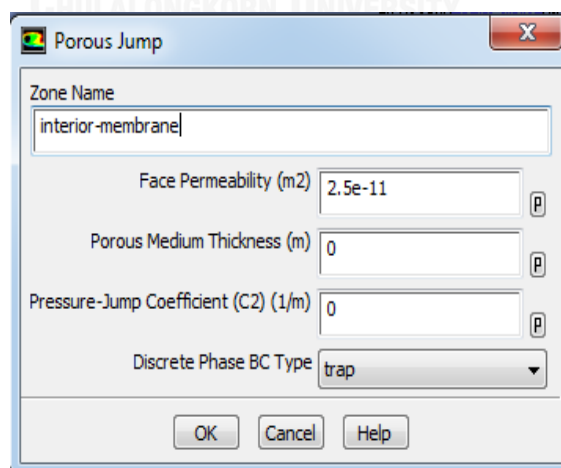


**Figure C.17** The boundary condition setting of porous zone.

9.)  Define > Solution method (step 6)

In solution panel, the energy solution was unselected (isothermal operation). The discretization was defined following the various flow parameter.

**Solve > Controls > Solution**

Pressure-velocity coupling: simple

Pressure: second order

Momentum: second order upwind

When ;  When the flow is not aligned with the grid (i.e., when it crosses the grid lines obliquely). The first-order c increases the large error of numerical discretization. The second-order get a higher accurate results than first order, especially in complex flows.

Turbulent kinetic energy: third-order muscl

Turbulent dissipation rate: third-order muscl

When ; third order muscl has a high efficient to improve spatial accuracy for all mesh geometry. It is suitable for complex three-dimensional flows.
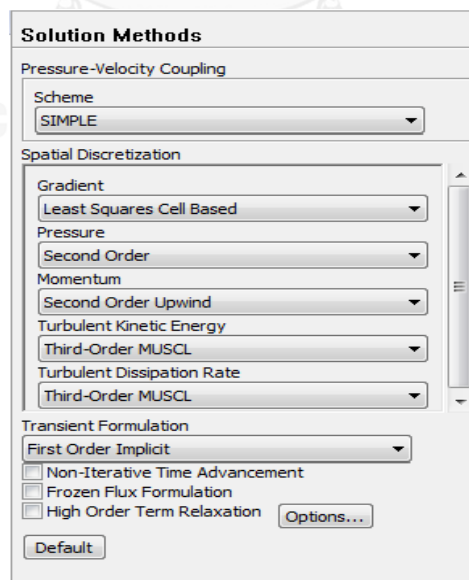


**Figure C.18** Setting of solution method.

10.)    Define > Solution controls (step 7)

For solution control, the under relaxation was selected in drop down list (set default).
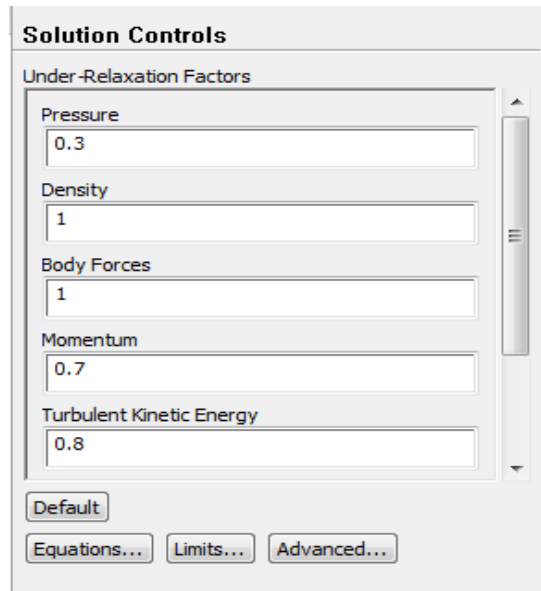
**Figure C.19** Setting of solution control.

11.)    Define > Monitor (step 8)

Set the limit of residual. For complete solution, the residual should be smaller than convergence value. In this study was set to $10^{-3}$.
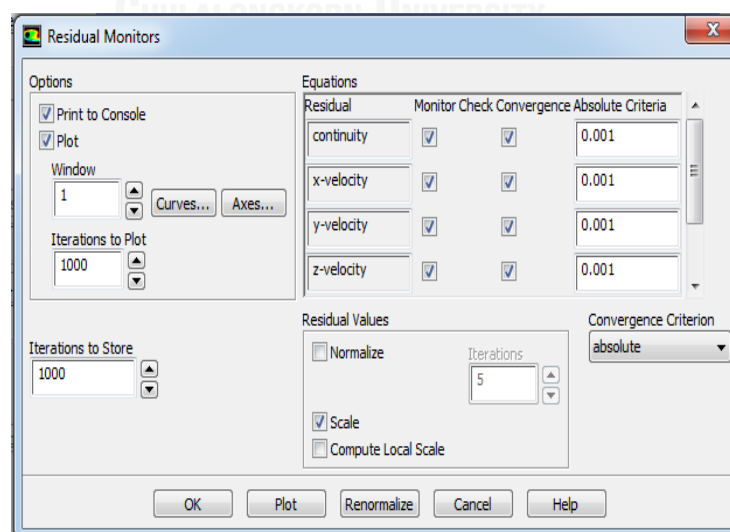
**Figure C.20** Setting of residual monitors.

12.) Define > Solution initialization (step 9)

Define > Solution initialization > Compute form > Inlet 4 > Initialize
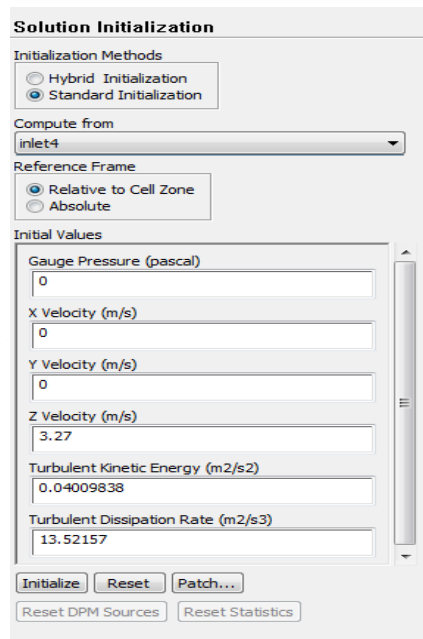


**Figure C.21** Setting of solution initialization.

13.) Define > Calculation activity (step 10)

Define > Auto save every > Edit > 1 time step > Ok



**Figure C.22** Setting of save data

14.)   Finally, Run calculation (step 11)

Define > Run calculation > Calculate



**Figure C.23** Setting of iteration in star-shaped microfiltration membrane.

# APPENDIX D

## Fouling resistance estimation

**Example @ critical flux of tubular membrane of Gesan : TMP =6800 ,** %trapped =44

$$J_C = \frac{TMP}{\mu(R_m+R_f)}$$

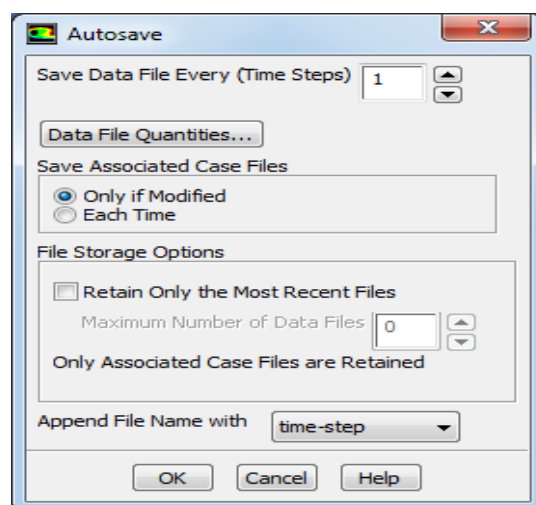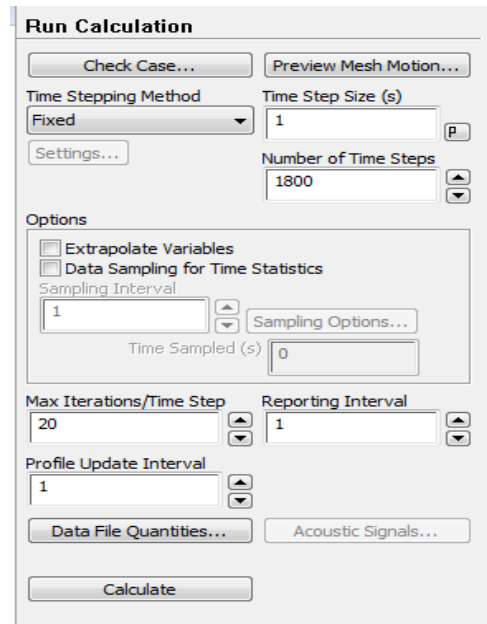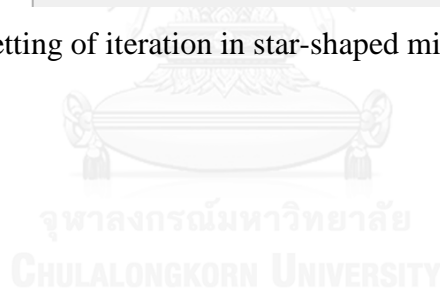$$J_C = \frac{6800\,Pa}{9.57x10^{-4}\,Pa.s \times ((4x10^{11}m^{-1})+(1.76x10^{11}m^{-1}))}$$

$$J_C = 1.23x10^{-5}\ m/s$$

| number | particle type | α (m/kg) | %trapped | (%trapped x particle flow rate x time)/membrane area = MD (kg/m$^2$) | (α x MD) = RF (m$^{-1}$) |
|--------|---------------|----------|----------|------------------------------------------------------------|--------------------------|
| 1 | latex | 2.00E+14 | 0.44 | 0.00087912 | 1.76E+11 |

**Example @ critical flux of tubular membrane of Chui et al : TMP =5500 Pa**

%trapped =70

$$J_C = \frac{TMP}{\mu(R_m+R_f)}$$

$$J_C = \frac{5500\,Pa}{8.62x10^{-4}\,Pa.s \times ((2x10^{11}m^{-1})+(2.74x10^{11}m^{-1}))}$$

$$J_C = 1.35x10^{-5}\ m/s$$

| number | particle type | α (m/kg) | fraction | (%trapped x particle flow rate x time)/membrane area = K | fraction x K = MD (kg/m$^2$) | (α x MD) = RF (m$^{-1}$) |
|--------|---------------|----------|----------|----------------------------------------------------------|------------------------------|--------------------------|
| 1 | peptone | 4.20E+10 | 0.47 | 1.99752 | 0.938834 | 3.94E+10 |
| 2 | CACL2 | 4.32E+08 | 0.01176 | 1.99752 | 0.023491 | 1.01E+07 |
| 3 | MEAT | 3.23E+11 | 0.32 | 1.99752 | 0.639206 | 2.06E+11 |
| 4 | urea | 2.15E+10 | 0.08823 | 1.99752 | 0.176241 | 3.79E+09 |
| 5 | magnesium | 2.54E+09 | 0.02588 | 1.99752 | 0.051696 | 1.31E+08 |
| 6 | potasium | 1.49E+11 | 0.08235 | 1.99752 | 0.164496 | 2.45E+10 |
| 7 | NACL | 1.75E+09 | 0.0205 | 1.99752 | 0.040949 | 7.15E+07 |
| | TOTAL | | | | | 2.74E+11 |

# APPENDIX E

## The quantity of fouling along z-direction of membrane

Type of microfiltration membrane

Tubular membrane

| Distance (mm) | % Trapped |
|---|---|
| 0-200 | 47 |
| 201-400 | 42 |
| 401-600 | 11 |

Star-shaped membrane

| Distance (mm) | % Trapped |
|---|---|
| 0-200 | 40 |
| 201-400 | 43 |
| 401-600 | 17 |

Star-shaped inserted rod

| Distance (mm) | % Trapped |
|---|---|
| 0-200 | 36 |
| 201-400 | 45 |
| 401-600 | 19 |

Inlet velocity

Inlet velocity = 2.5 m/s

| Distance (mm) | % Trapped |
|---|---|
| 0-100 | 32 |
| 101-200 | 33 |
| 201-300 | 35 |

Inlet velocity = 3.27 m/s

| Distance (mm) | % Trapped |
|---|---|
| 0-100 | 25 |
| 101-200 | 35 |
| 201-300 | 40 |

Inlet velocity = 4.0 m/s

| Distance (mm) | % Trapped |
|---|---|
| 0-100 | 19 |
| 101-200 | 34 |
| 201-300 | 47 |

Particle size

Small size of particle

| Distance (mm) | % Trapped |
|---|---|
| 0-100 | 31 |
| 101-200 | 32 |
| 201-300 | 37 |

Medium size of particle

| Distance (mm) | % Trapped |
|---|---|
| 0-100 | 29 |
| 101-200 | 33 |
| 201-300 | 38 |

Large size of particle

| Distance (mm) | % Trapped |
|---|---|
| 0-100 | 28 |
| 101-200 | 31 |
| 201-300 | 41 |

Baffle type

Rod baffle

| Distance (mm) | % Trapped |
|---|---|
| 0-100 | 25 |
| 101-200 | 35 |
| 201-300 | 40 |

Special rod baffle

| Distance (mm) | % Trapped |
|---|---|
| 0-100 | 28 |
| 101-200 | 33 |
| 201-300 | 39 |
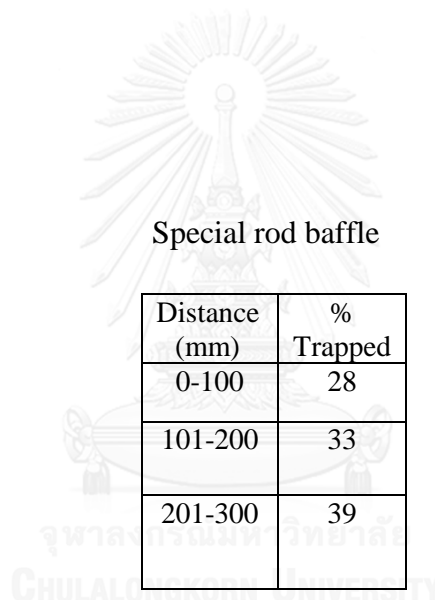
**VITA**

Mr. Sophon Leechasan was born on February 8 th, 1990 in Bangkok, Thailand. He studied at King Mongkut's University of Technology North Bangkok, Nonthaburi, Thailand for 4 years and received a Bachelor's Degree of Science from the Department of Chemical Engineering in April 2012. Then, he pursued his study in Master's Degree of Science at the Department of Chemical Engineering, Chulalongkorn University in 2012.

In June 2014, he participated in PSU-USM-NSTRU International Conference, Songkhla, Thailand and published his work under the topic ''Computational fluid dynamics modeling of effect of baffles in star shaped micro filtration membranes for water treatment''.